

Online Derivatization Aerosol Mass Spectrometry for the analysis of organic peroxides, alcohols and carboxylic acids in aerosol particles

Dissertation

For Attaining the Academic Degree of
“Doctor rerum naturalium” Dr. rer. nat.
at the Chemistry Department;
Faculty of Chemistry, Pharmaceutical Sciences,
Geography and Geoscience
of the Johannes Gutenberg-University, Mainz

by

Marcel Weloe

born in Mainz, Germany

JOHANNES GUTENBERG
UNIVERSITÄT MAINZ



Mainz, May 2020

Faculty director: [REDACTED]

1st supervisor: [REDACTED]

2nd supervisor: [REDACTED]

Date of Examination:

D77 – Dissertation of the Johannes Gutenberg University, Mainz

“Now this is not the end. It is not even the beginning of the end. But it is, perhaps, the end of the beginning.” Winston Churchill

Zusammenfassung

Atmosphärische Aerosole sind als in Luft suspendierte flüssige oder feste Partikel definiert. Sie streuen und absorbieren die elektromagnetische Strahlung, was zu einer Abkühlung bzw. Erwärmung der Atmosphäre führt. Sie nehmen Wasser auf und bilden Wolken. Je kleiner die Partikel sind, desto tiefer gelangen sie in die Atemwege. Sie haben daher einen wichtigen Einfluss auf das Klima und die menschliche Gesundheit. Die optischen und toxikologischen Eigenschaften variieren zeitlich und räumlich stark und sind abhängig von der Herkunft der Luftmassen, von gasförmigen Vorstufen, Primärquellen, reaktiven Spezies wie Ozon-, OH- oder NO₃-Radikalen, Temperatur, relativer Luftfeuchtigkeit und Strahlung. Zur Messung dieser kurzfristigen Variation und zur Charakterisierung von Aerosolquellen werden sogenannte Online-Instrumente, bei denen Probenahme und Analyse gleichzeitig erfolgen, eingesetzt, wobei bevorzugt Massenspektrometer für die chemische Charakterisierung verwendet werden. Das hochauflösende Flugzeit-Aerosolmassenspektrometer (*High Resolution Time of Flight Aerosol Mass Spectrometer*, HR-ToF-AMS oder kurz AMS), das hauptsächlich in dieser Doktorarbeit verwendet wurde, enthält eine Elektronenstoßionisationsquelle (EI), die mit einem Flugzeit-Massenspektrometer verbunden ist. Die EI-Quelle begünstigt die Quantifizierung eines Aerosols mit unbekannter Zusammensetzung, da die Empfindlichkeit der Ionisierung für ähnliche Verbindungen nahezu gleich ist. Für die Quantifizierung üblicher atmosphärischer Aerosolpezies ist eine Kalibrierung für wenige Standardverbindungen erforderlich. Die Partikelkomponenten werden jedoch nicht vor der Ionisierung abgetrennt, und eine starke gleichzeitige Fragmentierung aller Verbindungen macht es unmöglich, detaillierte chemische Informationen über einzelne Verbindungen oder funktionelle Gruppen zu erhalten, solange kein charakteristisches Fragment oder Marker-Ion bekannt ist. Infolgedessen werden die organischen Verbindungen normalerweise als „Organik“ zusammengefasst.

Das Ziel dieser Doktorarbeit war die Quantifizierung einzelner funktioneller Gruppen in Aerosolpartikeln mittels chemischer Nachweis- oder Derivatisierungsmethoden. Im Fokus standen dabei Peroxide, die wichtige Intermediate bei der Oxidation von organischen und schwefelhaltigen Verbindungen in der Atmosphäre sind. Ihre Analyse ist jedoch aufgrund ihrer chemischen Reaktivität und Artefaktbildung immer noch eine analytische Herausforderung. In einer *Proof-of-Principle*-Studie sollte eine Echtzeitmethode für Alkohole und Carbonsäuren mithilfe der Silylierung entwickelt werden.

Zum Erzielen der jeweiligen Nachweisreaktion wurden das im Trägergas angereicherte Nachweisreagenz und die Aerosolpartikel in eine Mischkammer gegeben, in der das Reagenz auf den Partikeln kondensierte und mit den Partikelbestandteilen sich vermischte. Das Produkt wurde unter Verwendung von Marker-Ionen, die an der EI-Quelle des AMS gebildet wurden, identifiziert und quantifiziert. Ein entscheidender Faktor bei beiden Methoden war der Aufbau der Gasquelle des Reagenzes und der Übergang zur Mischkammer.

Für die Peroxidbestimmung wurde Triphenylphosphin (TPP), das mit Peroxiden Triphenylphosphinoxid (TPPO) bildet, als Reagenz verwendet. Es wurde zur

Schmelze erhitzt, dabei im Stickstoffstrom angereichert und dieser mit dem kühleren Aerosolstrom vermischt, was zur Kondensation von TPP auf den Partikeln führte. Das Molekülion $[M]^+$ und das Molekülion mit Wasserstoffabstraktion $[M-H]^+$ wurden als Markerionen für TPP bzw. TPPO gefunden und für die Kalibrierung mittels Tandem-DMA-AMS verwendet (DMA: *differential mobility analyzer*). Die neue Methode wurde *online redox derivatization (ORD)-AMS* genannt. In sogenannten Kammerexperimenten wurden mittels Ozonolyse von Monoterpenen sekundäre organische Aerosolverbindungen (SOA) gebildet, welche entweder neue Partikel bildeten oder auf bereits vorhandenen Ammoniumsulfatpartikeln kondensierten. Dabei zeigte sich, dass der Peroxidanteil in SOA zunächst zunahm und dann abnahm. Am Ende der Ozonolyse lagen die Anteile im Bereich von 20 bis 70% und entsprachen denen, die in der Literatur gefunden wurden.

Eine große Herausforderung der Methodenentwicklung war die Hintergrundkorrektur, da das Markerion von TPPO bereits auf reinen TPP-Partikeln und auf nicht-reaktiven Ammoniumsulfat-Partikeln nachgewiesen wurde. Bei den Kammerexperimenten wurde beobachtet, dass die Zeitverläufe von TPP und TPPO umso ähnlicher wurden, je mehr TPP dem Partikel zugesetzt wurde. Aus diesem Grund wurde das Hintergrund-TPPO durch ein Referenzverhältnis von TPPO zu TPP vom Gesamt-TPPO abgezogen. Das Referenzverhältnis wurde bei der Kondensation von TPP zu den Ammoniumsulfat-Partikeln ermittelt. Dieses Referenzverhältnis wurde auch als Minimalwert bei der Außenmessung erhalten, was diese Korrekturmethode unterstützt.

Schließlich wurde eine Online-Methode zur Bestimmung von Peroxiden in Aerosolpartikeln in der Außenluft erfolgreich durchgeführt. Dabei wurden erhöhte Peroxidkonzentrationen tagsüber an Arbeitstagen gefunden, was auf eine photochemische und anthropogene Quelle der Peroxide hinwies. Weitere Untersuchungen sollten die Herkunft des TPPO-Hintergrunds sowie intra- und intermolekulare Effekte auf Ausbeute und Selektivität umfassen.

Die Entwicklung der Online-Silylierung gliederte sich in zwei Teile. Bei der sogenannten Offline-Silylierung wurden mittels *N*-Methyl-*N*-trimethylsilyl-trifluoressigsäureamid (MSTFA) zunächst Trimethylsilyl-Derivate langkettiger Monoalkohole, Mono- und Dicarbonsäuren nach Referenzmethoden hergestellt. Ihre jeweiligen Lösungen wurden zu Aerosolen zerstäubt, die mit dem AMS gemessen wurden. Dabei wurde das Trimethylsilylkation $[TMS]^+$ als Produkt der EI-Ionisation als gemeinsamer Marker für alle Testverbindungen gefunden. Weiterhin war das Signal dieses Ions proportional zur Anzahl der Hydroxyl- oder Carboxylgruppen unabhängig vom organischen Rest, so dass ein gemeinsamer Kalibrierfaktor für die Testverbindungen genutzt werden konnte.

Im zweiten Teil wurde bei der Online-Silylierung ein mit MSTFA angereicherter Stickstoffstrom zu Testaerosolen der langkettigen Monoalkohole, Mono- und Dicarbonsäuren gegeben. Dabei wurde das gleiche Verhältnis des $[TMS]^+$ -Signals zur Anzahl der Hydroxyl- und Carboxylgruppen wie bei der Offline-Silylierung gefunden,

was auf eine vollständige Umwandlung der Ausgangsverbindung in das Trimethylsilylderivat hinwies.

Die Silylierung von Verbindungen mit kürzerer Kohlenwasserstoffkette führte jedoch aufgrund der hohen Flüchtigkeit der Derivate zu einer Verdampfung der Partikel. In weiteren Untersuchungen könnten Tributylsilyl-Derivate mit geringerer Flüchtigkeit hergestellt werden, um die Methode für kurzkettige Verbindungen zu erweitern. Weiterhin sollten sterische und elektronische Effekte, der Einfluss der Mehrfachsilylierung auf den gemeinsamen Kalibrierfaktor und die Reaktion mit anderen funktionellen Gruppen wie Aldehyden, Ketonen und Aminen untersucht werden.

Abstract

Atmospheric aerosols are defined as liquid or solid particles suspended in the air. They scatter and absorb the radiation leading to a cooling and warming effect, respectively. They take up water forming clouds. The smaller the particles, the deeper they enter the respiratory system. Therefore, they have an important impact on climate and human health. The optical and toxicological properties vary strongly in time and space. They are depending on the origin of the air masses, on gaseous precursors, primary sources, reactive species like ozone, OH or NO₃ radicals, temperature, relative humidity and radiation. So-called online instruments, where sampling and analysis are performed simultaneously, are used to measure this short-term variation and to characterize aerosol sources, whereby mass spectrometers are preferred for the chemical characterization. The High-Resolution Time-of-Flight aerosol mass spectrometer (HR-ToF-AMS, or briefly AMS), mainly used during this Ph.D. thesis, contains an electron impact ionization (EI) source connected with a time-of-flight mass spectrometer. The EI source benefits the quantification of an aerosol with unknown composition since the sensitivity of the ionization is nearly the same for similar compounds. Calibration for a few standard compounds is required for the quantification of common ambient aerosol species. However, the particle components are not separated from each other before the ionization and the strong and simultaneous fragmentation of all compounds makes it impossible to obtain detailed chemical information about single compounds or functional groups, if no characteristic fragment or marker ion, is known. As a consequence, the organic species are usually summarized as “organic”.

In this Ph.D. thesis, the goal was the quantification of single functional groups in aerosol particles applying chemical detection or derivatization methods on airborne particles. Thereby, the focus was set on peroxides, which are important intermediates during the oxidation of organic and sulfur-containing compounds in the atmosphere. Their analysis, however, is still an analytical challenge because of their chemical reactivity and artifact formation. In a proof-of-principle study, a real-time method for alcohols and carboxylic acids should be developed using silylation reactions.

To achieve the respective detection reaction, the detection reagent, enriched in a carrier gas, and the aerosol particles were supplied into a mixing chamber, where the reagent condensed on the particles and was mixed with the particle components. The product was quantified using marker ions, formed at the EI source of the AMS. A crucial factor in both methods was the construction of the gas source of the reagent and the transition to the mixing chamber.

For the peroxide determination, triphenylphosphine (TPP), forming triphenylphosphine oxide (TPPO) was used as a reagent. It was heated over its melting point leading to the enrichment in a nitrogen flow and was mixed with the cooler aerosol flow leading to condensation on the particles. The molecular ion ([M]⁺) and the molecular ion with hydrogen abstraction ([M-H]⁺) for TPPO were found as marker ions and used for the calibration by tandem DMA-AMS (DMA: differential mobility analyzer). The TPP-peroxide method was named *online redox derivatization*

(ORD)-AMS. In so-called chamber experiments as first application, secondary organic aerosol (SOA) compounds were formed during the ozonolysis of monoterpenes. They nucleated to new pure SOA particles or condensed on preexisting ammonium sulfate seed particles. Thereby it was shown that the peroxide part of SOA first increased and then decreased. Furthermore, the final ratios of peroxide to SOA were in a range of 20 to 70% corresponding to those found in the literature.

A challenge of the method development was the background correction as the marker ion of TPPO was already detected on pure TPP particles and unreactive ammonium sulfate seed particles. As observed in the chamber experiment, the more TPP was added to the particles, the more similar the time series of TPP and TPPO became. Therefore, the background TPPO was connected to the TPP concentration by the reference ratio of TPPO and TPP when TPP was added to the unreactive seed aerosol. This reference ratio was also found as a minimum value at the outdoor measurement, which supports this correction method.

Finally, an online method for the determination of peroxide in ambient aerosol particles was successfully developed. The peroxide concentration increased during the daytime on the working days indicating a photochemical and anthropogenic source of the peroxides. Further investigation should include the origin of the TPPO background, intra- and intermolecular effects on the yield and selectivity.

The development of the online silylation reaction was divided into two parts. In the so-called offline silylation, trimethylsilyl derivatives of long-chained mono alcohols, mono- and dicarboxylic acids were produced with *N*-methyl-*N*-trimethylsilyl trifluoroacetamide (MSTFA) using reference methods. Their respective solutions were nebulized to aerosols, which were measured by the AMS. The trimethylsilyl cation ([TMS]⁺), a product of the EI ionization, was found as a common marker for all test compounds. Furthermore, the signal intensity of this ion was proportional to the number of hydroxyl or carboxylic groups independent of the organic residual.

The second part was the online silylation reaction. The silylation agent MSTFA was enriched in a nitrogen flow and added to test aerosols of the long-chained mono alcohols, mono- and dicarboxylic acids. The same ratio of the [TMS]⁺-signal to the number of hydroxyl and carboxylic groups was found as in the offline silylation reaction indicating complete conversion of the respective starting material to its trimethylsilyl derivative.

However, the silylation of compounds with shorter hydrocarbon chains lead to evaporation of the particles due to the high volatility of the derivatives. In further research, tributylsilyl derivatives with lower volatility could be produced to extend the method for short-chained compounds. Furthermore, steric and electronic effects, the influence of multiple silylation on the common calibration factor, and the reaction with other functional groups like aldehydes, ketones and amides needs to be further investigated.

Content

Zusammenfassung.....	v
Abstract.....	ix
1 Introduction.....	1
1.1 Atmospheric aerosols.....	1
1.1.1 Primary and secondary aerosol.....	1
1.1.2 The relation between size, chemical composition, source and lifetime..	1
1.1.3 Influence of aerosol particles on climate and human health.....	2
1.2 Organic aerosol chemistry.....	3
1.2.1 The occurrence of organic species in the particle phase.....	3
1.2.2 Physical properties with influence on particle chemistry.....	5
1.3 Chemical analysis of organic aerosols.....	6
1.4 Motivation.....	7
2 Instruments.....	11
2.1 Particle generation.....	11
2.2 Gas sources.....	11
2.3 Gas phase separation and particle dilution.....	12
2.4 Scanning mobility particle sizer.....	13
2.5 HR-ToF-AMS.....	14
2.5.1 Aerodynamic lens.....	17
2.5.2 Particle Time-of-Flight.....	17
2.5.3 EI mass spectrometry and quantification.....	18
2.5.4 ToF mass spectrometry and mass resolution.....	20
2.6 Calibration of the AMS.....	23
2.6.1 Density.....	23
2.6.2 PToF.....	24
2.6.3 Mass concentration.....	24
2.7 Mass spectrometer with soft ionization sources.....	26
2.7.1 APCI.....	26
2.7.2 AeroFAPA.....	27
2.7.3 Ion trap.....	28
2.7.4 Electron multipliers.....	30
3 Online redox derivatization for peroxide analysis.....	33
3.1 Introduction.....	33

3.2	Method development.....	34
3.2.1	Methods.....	35
3.2.2	Results and discussions.....	38
3.3	Peroxide analysis of SOA without seed aerosols.....	46
3.3.1	Method.....	46
3.3.2	Results.....	49
3.4	Ambient air measurements.....	55
3.4.1	Method.....	55
3.4.2	Results.....	55
3.5	Conclusions.....	57
4	Online silylation.....	59
4.1	Introduction.....	59
4.2	Method development.....	59
4.2.1	Method.....	60
4.2.2	Results.....	61
4.3	Online silylation at ambient aerosols.....	69
4.3.1	Method.....	69
4.3.2	Results.....	69
4.4	Conclusion.....	76
5	Summary and Outlook.....	79
6	References.....	84
7	Appendix.....	101
7.1	Supplement to section 3.2.....	101
7.1.1	Calibration setup.....	101
7.1.2	Calibration method.....	101
7.1.3	Result of the calibration.....	102
7.1.4	TPPO background.....	103
7.1.5	Calculation of the SOA concentration.....	104
7.1.6	Size distribution at SOA experiments.....	105
7.1.7	TPP excess to SOA.....	108
7.2	Supplement to section 3.3.....	109
7.3	Supplement to section 3.4.....	111
7.4	Supplement to section 4.2.....	112
7.4.1	Chemicals.....	112

7.4.2	Conditions for the determination of the calibration factor	112
7.5	Supplement to section 4.3.....	114
7.6	Lists.....	119
7.6.1	Abbreviation.....	119
7.6.2	Figure	120
7.6.3	Table	123
7.6.4	Equation	123
8	List of related publications and presentations.....	125
9	Acknowledgment	126
10	Curriculum Vitae	127

1 Introduction

1.1 Atmospheric aerosols

Atmospheric aerosols are defined as a suspension of particles or droplets dispersed in air, also referred to as particulate matter (PM). They can be liquid, solid or contain multiple phases such as gels surrounding solid cores, two phases' liquid particles or organic glasses. They have diameters between 2 nm and 10 μm , remain airborne for several hours to days due to the little mass inertia and are transported over long distances impacting air quality, climate and human health. (McNeill, 2017; Pöschl, 2005; Seinfeld and Pandis, 1998; Hallquist et al., 2009; Kolb and Worsnop, 2012)

1.1.1 Primary and secondary aerosol

Two pathways of aerosol formation in the atmosphere are known (Seinfeld and Pandis, 1998; Pöschl, 2005; Hoffmann et al., 2007; Chapleski et al., 2016; Kulmala et al., 2014; Zhao et al., 2013a; Cocker et al., 2001):

Primary aerosols are emitted directly into the atmosphere and secondary aerosols are formed chemically from gaseous precursors (Kolb and Worsnop, 2012), such as sulfur dioxide SO_2 , nitrogen oxides NO_x or organic vapors. At a low particle number concentration, the oxidation products with low volatility such as sulfuric acid and the so-called extremely low-volatile organic compounds (ELVOC) (Donahue et al., 2011; Donahue et al., 2012) form clusters. Ammonia, organic amines and water can be included as well (Hoffmann et al., 2007; Kulmala et al., 2014; Hallquist et al., 2009). This process is called homogenous nucleation, whereby one has to distinguish between homomolecular and heteromolecular nucleation (Seinfeld and Pandis, 1998). The first one describes the formation of new particles from one species and the latter one describes the particle formation from several different compounds. Gas-particle partitioning (Pöschl, 2005) or heterogeneous nucleation (Seinfeld and Pandis, 1998) describe the condensation or absorption of the oxidation- or acid-base addition products on preexisting so-called seed particles. Physical processes such as temperature-dependent evaporation, condensation of semi-volatile compounds, and chemical alterations in the gas or particle phase lead to a mixing of secondary and primary aerosol species which describes chemical aging (Kolb and Worsnop, 2012).

1.1.2 The relation between size, chemical composition, source and lifetime

The size, the chemical composition, and the lifetime of an aerosol depend heavily on the source of particles or particle species (Seinfeld and Pandis, 1998; Pöschl, 2005; Pandis, 2004). Primary particles are often produced via mechanical processes like sea spray, volcanic eruption, and wind-blown and are often found in the so-called coarse mode with diameters larger than 2.5 μm . They contain sea salt, minerals, industrial- and traffic dust or biogenic aerosols such as pollen and spores. The lifetime of these larger particles is in a range of several hours to a few weeks and is limited by dry deposition (Kolb and Worsnop, 2012; Pandis, 2004).

Particles with diameters smaller than 2.5 μm contribute to the so-called fine mode, which is divided into several subgroups (Pandis, 2004). Biomass or fuel-burning produce 20-30 nm primary soot particles containing elemental or black carbon (Seinfeld and Pandis, 1998). Primary particle species from meat charbroiling,

Introduction

cigarettes and wood-burning were also found in the fine mode (Kleeman et al., 1999; Nolte et al., 2002).

Secondary aerosol components occur mainly in the fine mode (Kavouras, 2002) and are composed of inorganic acids, their ammonium salts, and organic material (McNeill, 2017; Seinfeld and Pandis, 1998). The newly formed particles are in the nucleation- or ultrafine mode with diameters smaller than 100 nm. These particles have a short lifetime of several hours since they grow fast by gas-particle partitioning and coagulation to larger particles in the accumulation mode (Pandis, 2004). Particles in the accumulations mode (100 nm – 2.5 μm) disappear mainly by wet deposition (rain-out), precipitation and have a lifetime of weeks to months making them the dominant mode in the atmosphere (Pandis, 2004). Another type of ultrafine mode is the Aitken mode (10-100 nm) describing primary particles on which secondary material has been condensed (Pandis, 2004).

1.1.3 Influence of aerosol particles on climate and human health

Aerosol particles influence the radiation from the sun directly and indirectly in clouds and therefore have a strong influence on the climate (McNeill, 2017). Light-adsorbing materials like black carbon, polyaromatic hydrocarbons, carbonyl- and N-containing compounds transfer the radiation into heat, warming the surrounding atmosphere. Due to oxidation and “photobleaching” (Sareen et al., 2013; Lee et al., 2014; Zhao et al., 2015), the organic species become more non-refractive like sea salt or mineral dust, which scatter or reflect the light, leading to a cooler atmosphere (Myhre et al., 2013).

Aerosol particles take up water in supersaturated conditions and function as cloud condensation (CCN) or ice nuclei (IN) (Pöschl, 2005; McNeill, 2017; Köhler, 1936). Hereby, they grow to cloud droplets larger than 10 μm . They can reach a critical diameter due to further collision and growth so that they rain-out. Particles from anthropogenic sources contribute to a larger amount of smaller cloud droplets with higher cloud albedo and lifetime (McNeill, 2017; Albrecht, 1989; Twomey, 1977). The indirect effect of aerosols in clouds on the climate results in a cooling of the atmosphere but is still not entirely clear (Myhre et al., 2013) since the impact of the chemical composition on the CCN-ability is still poorly understood.

Aerosols are strongly connected to air quality and impact human health. Correlations with higher rates of mortality, cardio- and respiratory diseases are known (Dockery et al., 1993; Forman and Finch, 2018). Smaller particles enter deeper into the respiratory system (Hinds, 1999). Chemical alteration of proteins in pollen (Franze et al., 2005; Reinmuth-Selzle et al., 2014; Lang-Yona et al., 2016) or polyaromatic hydrocarbons PAH (Tomaz et al., 2017) due to ozone and NO_x radicals might be a reason for a higher rate of allergies and asthma in children in urban areas (Li et al., 2016b). Reactive oxygen species (ROS), including OH, O_2^- , HO_2 , O_3 and H_2O_2 , produced by transition metals, quinones and secondary organic aerosol (SOA) might increase the risk of respiratory disease (Lakey et al., 2016; Tong et al., 2017).

The organic chemistry will be described further because of the high contribution of organic material in the fine mode.

1.2 **Organic aerosol chemistry**

Organic aerosols are classified into a primary organic aerosol (POA) and SOA. POA contains hydrocarbons and fatty acids from traffic (Zheng et al., 2014; Schauer et al., 2002), cooking (Rogge et al., 1991) and pyrolyzed sugars from biomass burning, such as levoglucosan (Kleeman et al., 1999). SOA with multifunctional species is mainly produced by oxidation of volatile organic compounds (VOC), initiated by hydroxyl radicals, ozone, nitrate radicals or photolysis (Chapleski et al., 2016; Hallquist et al., 2009).

1.2.1 **The occurrence of organic species in the particle phase**

The vapor pressure, influenced by the Kelvin and the Raoult effect, can be used to estimate whether a species resides in the gas or the particle phase. According to Raoult's law, a semi-volatile compound condenses on absorbing material, even when its saturation concentration has not been reached in the gas phase (Hallquist et al., 2009). According to the Kelvin effect, smaller particles have a stronger curved surface leading to a higher volatility (Seinfeld and Pandis, 1998). The Kelvin effect becomes important for aqueous particles smaller than 50 nm in diameter and particles with high molecular weight organics (like dioctyl phthalate, *molecular weight* = 391 g/mol) smaller than 200 nm in diameter. The formation of stable clusters during the nucleation only occurs when the condensation rate overcomes the evaporation rate. This is due to the strong Kelvin effect in small particles of few nanometers. Thus, the condensation on preexisting particles is preferred over particle new formation (Kulmala, 2003). Only species with extremely low volatility like sulfuric acid, iodide and so-called ELVOCs (extremely low volatile organic compounds), supported by water, amines and ammonia, participate in the particle formation. Condensation of more volatile compounds occurs only after a critical size has been reached.

Highly oxidized multifunctional molecules (HOMs) with several geminal hydroxy and/or hydroperoxyl groups are proposed to participate in the particle formation (Zhao et al., 2013a; Ehn et al., 2012). Hereby, Mentel et al. (2015) pointed out that most of the ELVOCs must be HOMs and they have to be produced rapidly by autoxidation including several additions of elemental oxygen on the radicals, produced by hydroxyl radicals, ozone or nitrate radicals. Slow or stepwise oxidation of organic species will not lead to the formation of supersaturated vapors which are required for particle formation under atmospheric conditions. Increased concentrations of dicarboxylic acids were found in particles with 10 and 20 nm diameter while increased concentrations of carbonyl compounds and low-weighted organic acids were found in particles with 40 nm diameter during the SOA production in the ozonolysis of α -pinene (Winkler et al., 2012).

Particle compounds can undergo different kinds of chemical alterations (Figure 1). Heterogeneous chemistry includes the reactions of gas-phase species such as NO_x , RO_y and H_xO_y or O_x ($x=1-3$, $y= 1-2$) at the particle-gas interface. Liu et al. (2017) observed nitration and oligomerization of tyrosine during the exposure of ozone and nitrogen dioxide. Oligoperoxides, condensed from the gas phase, were detected in the particle phase during the ozonolysis of enol ethers (Sadezky et al., 2006). Another example of heterogeneous chemistry was the conversion of carbonyl groups to less volatile

Introduction

hemiacetals, acetals and hydrates from the gas phase in the presence of acidic seed aerosol particles, with the products remained in the particle phase (Czoschke, 2003).

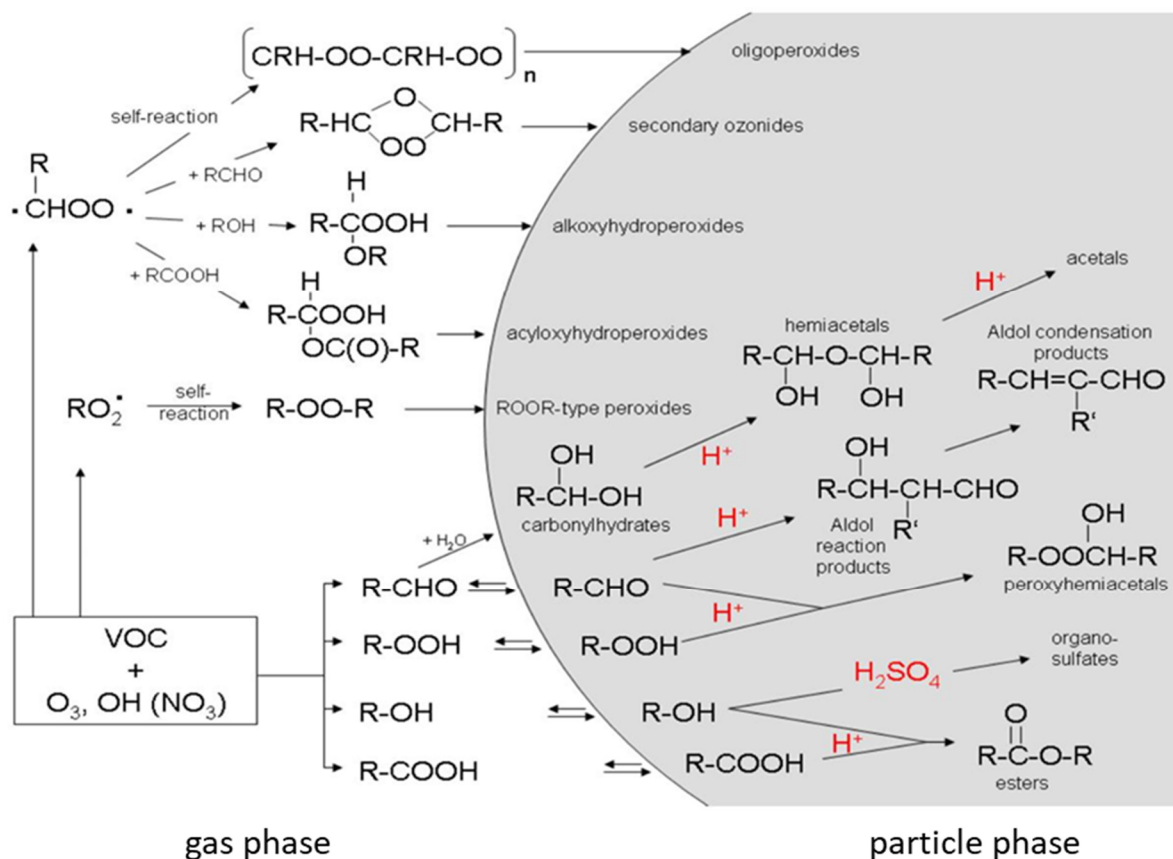


Figure 1: Organic chemistry in the gas- and particle phases (modified from Hallquist et al. (2009)).

Different reactions inside the particles lead to products with higher volatility than their precursors in the case of carbon chain breaking or to products with lower volatility due to further oxidation or oligomerization (chain elongation). The concentration of carboxylic acid groups is often increased in aged aerosols (Hallquist et al., 2009). Hydroperoxides can decompose forming hydroxyl radicals in the particle phase which can cause further oxidation there (Tong et al., 2016). Carbonyl groups undergo aldol- or geminal-diol reactions or formation of peroxyhemiacetals with hydroperoxides and especially formation of hydrates with water (Hall and Johnston, 2012). Methacrolein from the oxidation of isoprene produces polyesters under high NO_x -conditions while C_5 alkene triols and 2-methyltetrol form hemiacetal dimers under low- NO_x -conditions (Surratt et al., 2006).

All these different kinds of organic compounds, reactions and the high contribution of total organic fraction of 20-90% (Kanakidou et al. 2005) result in a strong impact on the physical, optical and physicochemical properties of the overall aerosol. Denjean et al. (2015) found that fresh-formed SOA particles from the ozonolysis of α -pinene have an increased concentration of less oxidized species at the surface inhibiting water absorption.

1.2.2 Physical properties with influence on particle chemistry

Physical properties like the hygroscopicity, the viscosity and the surface tension influence processes like condensation, evaporation, and diffusion inside the particles as well as chemical reactions and lifetime of the compounds therein (Shiraiwa et al., 2011; Zelenyuk et al., 2012; Abramson et al., 2013; Koop et al., 2011).

Abramson et al. (2013) showed that the evaporation rate of pyrene, trapped in SOA particles, was dependent on the viscosity of SOA particles. The viscosity ranges from 10^{-3} to 10^9 Pa s with coalescence times between 10^{-7} and 10^5 s, respectively (Power et al., 2013). The coalescence describes the relaxation of two aggregated particles forming a new particle. According to Koop et al. (2011), the glass transition temperature of a species, its molar mass and the water content are the most important parameters to predict the viscosity of a particle. The glass transition temperature describes the transition of a fast-cooled liquid in which the high viscosity prevents the arrangement of the molecules or atoms into the crystalline state (Virtanen et al., 2010; Debenedetti and Stillinger, 2001; Angell, 1995). Typical SOA components such as pinonic acid, pinic acid or multi-carboxylic acids have glass transition temperatures close to room temperature. Mixing these compounds can both increase and decrease the glass transition temperature depending on how the molecules interact with each other. Water acts usually as a plasticizer leading to particles being rather low viscous at high relative humidity.

The content of water and the viscosity of the particles also depend on the hygroscopicity of the aerosol (Koop et al., 2011), describing the ability to take up water. The deliquescence describes the liquefaction due to absorbing water and the efflorescence describes the transition from a liquid into a solid due to evaporation of water (Smith et al., 2011; Martin, 2000). Varutbangkul et al. (2006) showed that SOA from the oxidation of cycloalkenes, mono-, and sesquiterpenes are less hygroscopic than typical inorganic species such as ammonium sulfate. Formation of highly oxidized polar compounds and the formation of long-chained oligomers may increase and decrease the hygroscopicity, respectively. This was observed during the oxidation of cyclohexenes and sesquiterpenes.

The surface tension has an impact on gas-particle interfacial processes (Facchini et al., 2000) such as the mass transfer between the interface and the particle interior (Schwier et al., 2012). The smaller the particle diameter, the larger is the impact of the surface tension towards higher vapor pressure (Seinfeld and Pandis, 1998). Particles with lower surface tension have a larger CCN-ability (Ovadnevaite et al., 2017). For example, surface films of hydrophobic organic compounds inhibit the water uptake under sub-saturated conditions due to their water insolubility. However, they reduce the surface tension resulting in an increased water uptake under supersaturated conditions (Ovadnevaite et al., 2011). Ruehl et al. (2012) observed a reduction of 50-75% of the surface tension of SOA-coated sodium chloride particles when the organic layer had a thickness of at least 0.8 nm.

1.3 Chemical analysis of organic aerosols

Different detection methods are applied for the chemical characterization of organic aerosols due to the high diversity of organic aerosol components. In general, a distinction has to be made between offline and online techniques.

Offline methods include particle collection in the field, temporary and locally separated from the analysis in the laboratory. Typically, particles are collected on filters, impactors or impingers. The analytes of interest are extracted and can be detected using suitable instruments. Agents for derivatization or the formation of detectable products and separation techniques such as chromatography are used to get detailed molecular information about the aerosol species. (Laskin et al., 2018; Pratt and Prather, 2012a)

However, collection times of several hours are required to collect enough material. Artifacts might occur during collection when, for example, gas-phase species condense on the filters or aerosol species evaporate due to a change in ambient temperature. Furthermore, chemical alteration can occur during sampling, storage, transportation and especially during the sample preparation (Pratt and Prather, 2012b). For example, Mutzel et al. (2013) investigated the analysis of peroxides in SOA during the ozonolysis of α -pinene. Positive artifacts of hydrogen peroxide were found when an ultrasonic bath was used for the extraction of filters. OH-radical formation due to the agitation and recombination to H_2O_2 was proposed. Alteration of other SOA components was also observed.

Atmospheric aerosol species from certain sources such as industry, traffic or cooking occur only temporarily or locally in elevated concentrations (Pratt and Prather, 2012b). The chemical alteration, gas-particle conversion and evaporation depend on the surrounding gas-phase, temperature, relative humidity, and other meteorological parameters. These can vary strongly during the day. The oxidation of terpenes and hydrocarbons by ozone or OH-radicals is often simulated in chamber experiments. Here, the SOA formation takes place in a range of a few hours (Hoffmann et al., 1998; Docherty et al., 2005; Zhang et al., 2015; Nah et al., 2016; Zhou et al., 2018). Therefore, online or real-time instruments with time resolutions of several seconds to minutes are often applied simultaneously in addition to offline methods. Here, particle sampling and analysis take place at the same instruments. Especially mass spectrometers are often used due to their low detection limit and universal application (Kolb and Worsnop, 2012; Laskin et al., 2018). They contain an ionization source, a mass analyzer with a detector, and a vacuum system (de Hoffmann and Stroobant, 2007). An additional vaporizer is often required to transform the species from the particle into the gas phase (Pratt and Prather, 2012b). The two types of ionization sources are hard ionization, including electron impact (EI) ionization, and soft ionization, including chemical ionization (CI) or photo ionization. The first one has the advantage that all organic compounds have similar ionization efficiencies (Jimenez et al., 2003). Quantification of the organic material is possible even when the chemical composition is not known. On the other hand, strong fragmentation occurs during EI and the identification of single compounds and certain functional groups is strongly limited since no separation of the components is performed (Pratt and

Introduction

Prather, 2012a). In contrast, soft ionization sources cause less fragmentation and enables the identification of single components (Pratt and Prather, 2012b). However, the sensitivity of different species can vary strongly (Reinnig et al., 2009), limiting quantification significantly.

Finally, a combination of both offline and online instruments is often used during field measurements and chamber experiments to get enough chemical information about the aerosol. Their data can be compared with those of instruments measuring gas-phase species and meteorological parameters.

1.4 Motivation

In this Ph.D. thesis, the goal was to quantify functional groups in aerosol particles using the aerosol mass spectrometer (AMS) of Aerodyne Research Inc. as an online instrument. The aerosol particles containing compounds with the functional group of interest were mixed with a detection or derivatization agent in a condenser (mixing chamber). The product of the derivatization reaction was detected quantitatively by characteristic fragments produced at the EI ionization of the AMS (Figure 2). More specifically, the detection of peroxides using triphenylphosphine (TPP) as an agent and the silylation of hydroxylic and carboxylic groups using *N*-Methyl-*N*-trimethylsilyl trifluoroacetamide (MSTFA) were investigated.

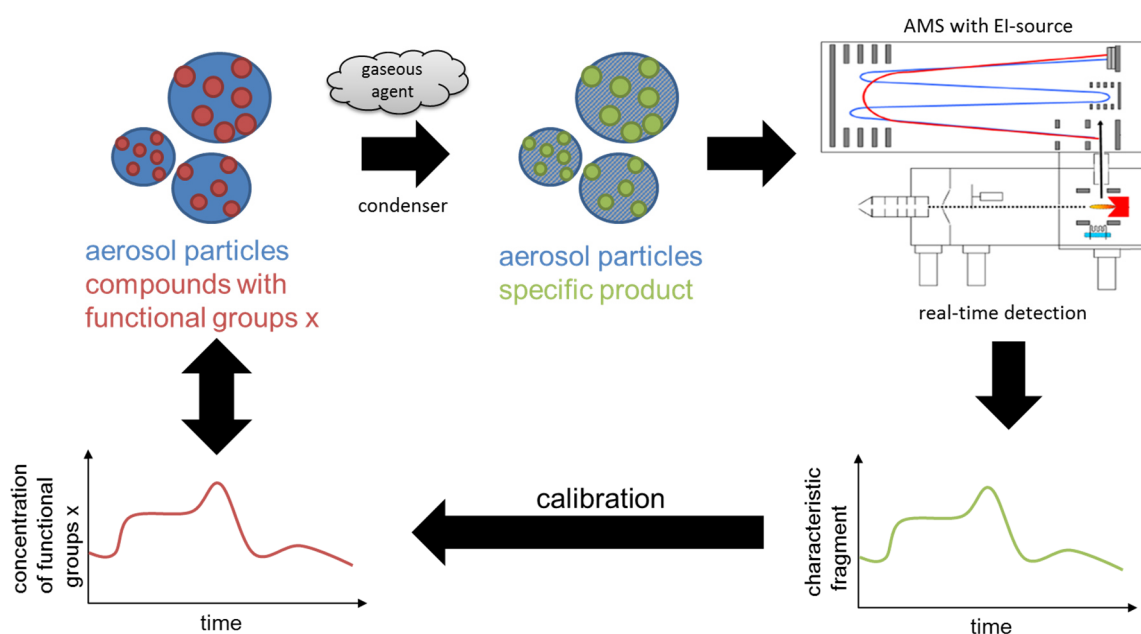


Figure 2: Schematic description of the determination of functional groups in the aerosol particles.

As shown in Figure 1 organic peroxides are involved in several processes in the atmosphere (Hallquist et al., 2009). It is suggested that they are dominant in HOMs and therefore in the particle formation from organic vapors (Tu et al., 2016; Ehn et al., 2012). Furthermore, they oxidize sulfur dioxide to sulfuric acid (Guo et al., 2014; Faust et al., 1993; Atkinson, 2000; Ye et al., 2018), another important component during particle formation. Docherty et al. (2005) estimated a percentage of 47% and 85% of peroxide to SOA mass during the ozonolysis of α - and β -pinene, respectively. Further details of the role of peroxide in the atmosphere are described in section 3.1.

Introduction

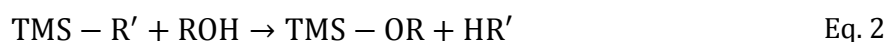
Traditionally, peroxide-containing particles are collected on filters or impactors. Their extracts are added to potassium iodide, which reacts with the peroxides forming iodine or triiodide-anions, detected using titration with sodium thiosulfate and spectroscopic methods, respectively (Mertes et al., 2012, 2012; Docherty et al., 2005; Mutzel et al., 2013; Surratt et al., 2006; Banerjee and Budke, 1964; Zhao et al., 2018).

Alternatively, triphenylphosphine (TPP) can be used as a reacting agent. As shown in Eq 1., TPP rapidly reacts with hydrogen peroxide, organic (hydro)peroxides and peroxy acids (ROOR') to triphenylphosphine oxide (TPPO) (Docherty et al., 2004; Ruiz et al., 2001), which can be detected spectrometrically (Porter et al., 1979), and the respective by-product (ROR'). There is only a limitation for tertiary peroxide groups. The main application of the TPP/TPPO-method is the determination of hydroperoxides from the autoxidation of oils and fats (Gotoh et al., 2011; Nakamura and Maeda, 1991; Wang et al., 2016).



However, as proven by Mutzel et al. (2013), positive artifacts occur during sample preparation and especially chemical artifacts can be expected during sampling, storing and transportation due to the high reactivity of peroxides (Epstein et al., 2014). Therefore, a real-time, so-called online derivatization method is required.

The silylation reactions is frequently used to convert low-volatile acids and alcohols into high volatile compounds enabling the analysis by gas chromatography coupled with a EI-mass spectrometer (Rontani and Aubert, 2004). Since the silylated compounds have a functional-group-specific fragmentation pattern, the online silylation provides a structural hint on the organic aerosol species (Urbach, 2012; Halket and Zaikin, 2003; Jaoui et al., 2005). However, a common characteristic fragment needs to be found and its signal needs to be proportional to the number of hydroxyl and carboxylic groups (ROH). This is required because the silylation of a mixture of compounds leads to the formation of different trimethylsilyl (TMS) compounds (TMS-OR) (Eq. 2) with different organic residuals R. In Eq. 2, TMS-R' is a silylation agent with at least one TMS group and a residue R' such as chloride, iodine, imidazole and trifluoroacetamide (Halket and Zaikin, 2003). HR' is the by-product of the silylation reaction.



Several requirements have to be considered for the online TPP - peroxide determination and the online silylation reaction (Figure 3). Firstly, the agent has to be mixed with the aerosol. Hereby, the agent has to be added as vapor, which condenses on the particles. Therefore, the volatility of the agent has to be sufficiently high so that it can be brought from a liquid or solid-state (reservoir of the reagent in Figure 3) into the gas phase. However, the volatility has to be low enough to condense in sufficient amounts onto the particles. Secondly, the aerosol should behave rather as a liquid for the fast diffusion of the reagent inside of the particle. Thirdly, the reaction product should have low volatility to avoid evaporation from the particle phase. Fourthly, the agent and the products have to be unreactive towards other species, especially towards oxygen and water as these compounds are highly abundant in the atmosphere and difficult to remove completely.

Introduction

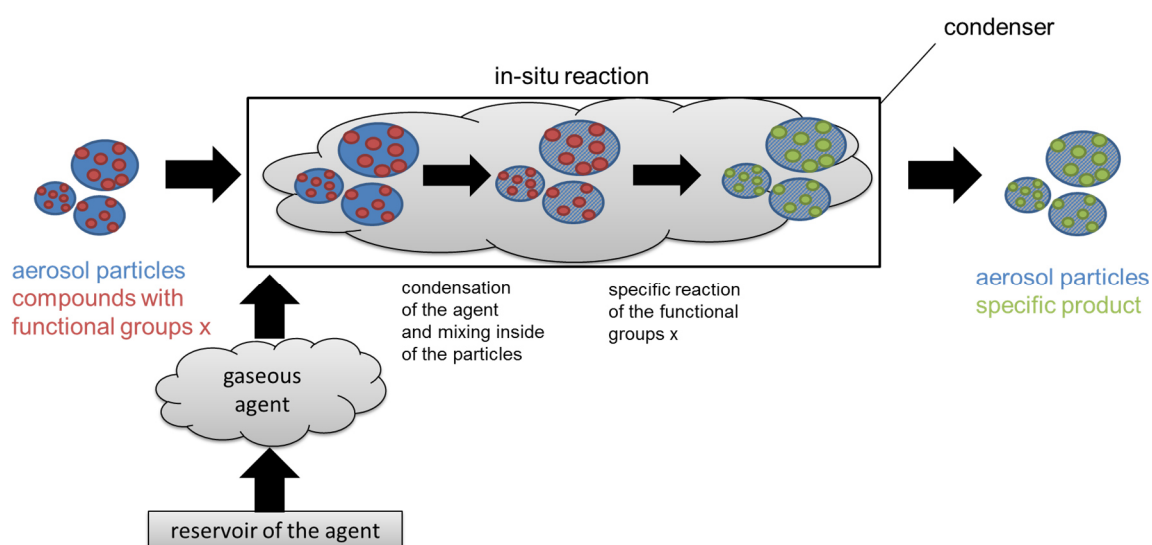


Figure 3: Scheme of the processes during the online analysis of functional groups.

The AMS consists of an EI-mass spectrometer in a high vacuum so that a matrix-independent quantification of the reaction products is principally expected (DeCarlo et al., 2006). Since there is no separation of the compounds before the ionization, the identification of the derivatization agent and product has to be done by characteristic fragment analysis. The instruments and methods, especially the AMS, are further described in chapter 2.

Finally, both methods need to be applicable for ambient aerosols. Therefore, the development of the methods includes not only the measurements of test aerosol with single components or with SOA mixtures, produced by ozonolysis of monoterpenes, but also includes the evaluation using outdoor measurements.

Introduction

2 Instruments

This chapter describes the instruments used in this Ph. D. thesis, focusing on particle and gas sources and physical and chemical aerosol analysis.

2.1 Particle generation

Test aerosols with a known composition must be generated to calibrate aerosol mass spectrometers. One possibility is the pneumatic nebulization of a solution containing a respective test compound. Its concentration is the most influential on the polydisperse size distribution. The higher the concentration, the larger are the particles (TSI, Instruction Manual, 2005). Monodisperse aerosol can be obtained when the polydisperse aerosol from the nebulizer is supplied through a differential mobility analyzer (DMA), as described in section 2.4.

Alternatively, a Sinclair-La Mer generator produces a monodisperse aerosol of a single compound. It contains a flask with the compound of interest and an air stream is supplied through the flask. When the flask is heated, a larger amount of the compound is introduced into the gas phase. The gas mixture is added to a second, cooler air stream in a condenser, where particles with a narrow size distribution are formed. The size of the particles depends on the ratio of the warmer gas mixture and the cooler air stream (Sinclair and La Mer, 1949).

Chamber aerosols are produced as a simulation of atmospheric processes like the oxidation of organic vapors by ozone, hydroxyl or nitrate radicals (Hoffmann et al., 2007). Hereby, the gases are supplied into the chamber, which can be a glass tube, a flask or a PTFE bag of several liter volume (Zhou et al., 2018; Hoffmann et al., 2007; Hoffmann et al., 1998). The aerosol, generated by homogenous nucleation (section 1.1.1), is polydisperse and contains several compounds. If seed aerosols are introduced into the chamber, particle formation will be inhibited in favor of the condensation on the preexisting seed particles (Huang et al., 2016).

2.2 Gas sources

Gas sources are often based on the shift of the equilibrium between the gas and liquid or solid phases of a volatile compound. The gas phase is perpetually removed by a carrier gas, thus the compound evaporates or sublimates continuously.

In a diffusion device (Figure 4a) as described by Thorenz et al. (2012) a 1.5 mL glass vial is placed in a tempered double-walled glass vessel. The vial contains the compound of interest and the cap of the vial is pierced by a silica capillary or a PTFE tube through its PTFE septum. The compound evaporates and diffuses through the capillary. The carrier gas is introduced by a spiral on the bottom of the vessel.

The permeation source (Figure 4b) contains a PTFE tube, filled with a liquid compound and sealed using stainless steel spheres. The polymer tube is permeable for the vapor, which forms over the liquid (Washenfelder et al., 2003). The tube is placed in a tempered double-walled vessel.

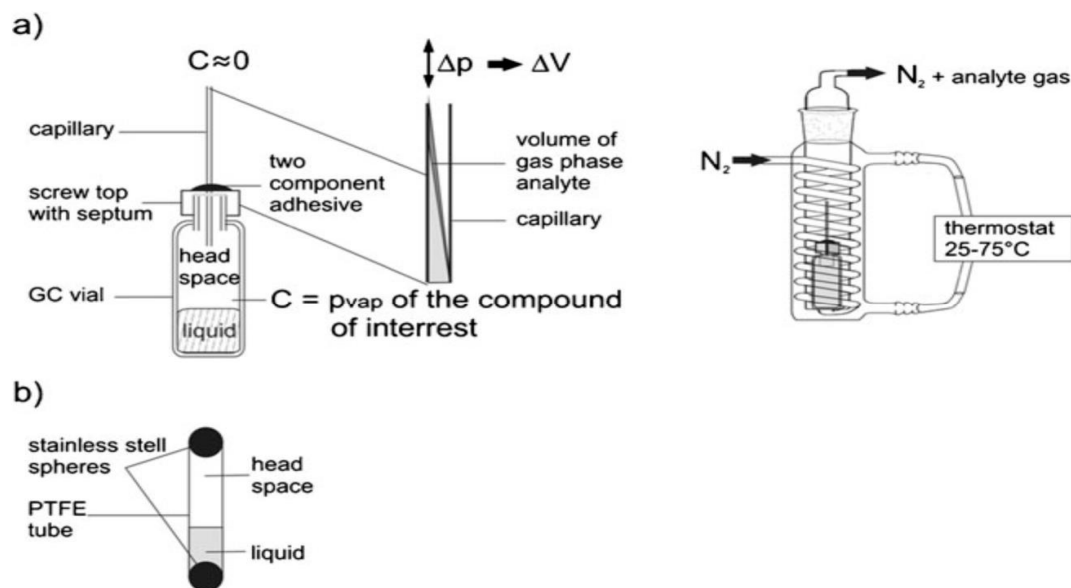


Figure 4: Gas sources: a) diffusion device b) permeation device (Reprinted by the permission from Springer Nature, Thorenz et al., © (2012)).

The vial of the diffusion device and the PTFE tube of the permeation source are weighed to measure the output of the respective compound (Thorenz et al., 2012). The output can vary due to the temperature in the vessel, the flow rate of the carrier gas and the material of the vial, its cap or the capillary and the material of the permeation tube. Thorenz et al. (2012) pointed out that diffusion devices are more suitable than permeation tubes for volatile or semi-volatile compounds because the output rate can be easily calculated. Permeation sources are preferred for stable test gas flow at low concentrations since the emission from diffusion devices is affected by hardly controllable pressure variations.

Alternatively, the carrier gas can be saturated with the respective compound by supplying it through a reservoir as used in Isaacman et al. (2014). The reservoir can be a glass vial which the carrier gas enters and leaves via two capillaries.

2.3 Gas phase separation and particle dilution

The aerosol particles must be separated from gas phase species for the online derivatization of functional groups to avoid reactions of compounds in the gas phase with the respective agent. Denuders or diffusion dryer are often used to reduce gas phase species. They contain an outer and an inner tube. The inner one is a cylindrical metal grid. The gap between the two tubes is filled with an absorbing material such as activated charcoal for organic material or silica gel for water. The aerosol is supplied through the inner tube and gas phase species are removed by absorption because of its stronger diffusion through the metal net to the absorbing material. Meanwhile, the particles follow the main flow direction in the tube. However, the smaller the particles, the higher its diffusion is so that also smaller particles are partly removed in the denuder (Rohling and Neidhart, 1995).

So-called high-efficiency particulate air (HEPA) filters remove the particle phase (Schroth, 1996), often used for background correction in aerosol mass spectrometry

(Canagaratna et al., 2007). Besides, HEPA-filters are used to dilute the particle concentration in the carrier gas. For this purpose, the aerosol is split into two streams and reunited after removing the particles of one of the streams. The ratio of the flowrates of the two streams sets the final particle concentration (Field ToF-AMS Operation).

2.4 Scanning mobility particle sizer

The scanning mobility particle sizer (SMPS) is a frequently used instrument for the determination of the particle size distribution, the particle number and the particle mass. It contains a neutralizer, a DMA and a condensation particle counter (CPC).

Aerosol particles in the atmosphere and especially from nebulized solutions contain one or several charges. The aerosol is supplied from the inlet through the neutralizer and the DMA to the CPC. The neutralizer contains a radioactive source such as ^{241}Am whereby a Boltzmann charge distribution on the particles is obtained. The DMA consists of an inner and outer cylindrical electrode. A sheath air stream is applied to generate a laminar flow parallel to the electrodes. The particles follow the laminar flow due to the kinetic force. An electrical field is generated by applying a voltage between the electrodes, leading to a curved trajectory of the charged particles towards the electrodes. The deviation from the trajectory parallel to the electrodes is called mobility and depends on the charge-to-diameter ratio of the particles. The smaller the charge-to-diameter ratio is, the more efficient the particles migrate to the electrodes. The outlet of the DMA is placed at the end of the inner electrode. At a certain voltage, only particles with a certain charge-to-diameter ratio exit the DMA. The voltage is kept constant in the single mode, which can be used to generate a monodisperse aerosol. Stepwise decreasing of the voltage is applied in the scanning mode used for the determination of the particle size distribution (Heim et al., 2004; Steiner et al., 2010).

The counting principle of the CPC is based on the light scattering of particles, which generally depends on the number, size and refractive index of the particles as described by Mie theory. The aerosol particles are supplied through a saturator, where they are mixed with a saturated vapor, typically with isopropanol or 1-butanol. The mixture is introduced into the condenser, where the vapor condenses on the particles forming droplets with diameters in the micrometer range (Stolzenburg and McMurry, 1991; Ahn and Liu, 1990).

Since all particles up to a certain diameter (tens of nanometers) grow to droplets with an almost equal diameter (Ahn and Liu, 1990) and since the droplets have almost the same refractive index (Szymanski, 2002), the intensity of the scattered light only depends on the particle number.

Particles in the DMA are in the so-called transition regime, which describes a flow regime of the gas around the particles and is determined by the Knudsen number Kn . Kn is the ratio of the mean free path to the particle radius. The continuum regime is the limit, when $Kn \ll 1$ and the free molecular regime is the other limit when $Kn \gg 1$. The transition regime is in between these limiting cases and describes the reduced drag force compared to the drag force in the continuum regime. The drag force affects

the particle mobility in the DMA in the opposite direction of the attraction due to the electric field. The mobility also depends on the particle shape. An aspherical particle with the same physical diameter d_{ve} as a spherical particle exits the DMA at a higher voltage due to the larger surface and drag force. Besides, the electric force depends on the diameter to charge ratio. A singly charged particle will exit the DMA at the same voltage as a twofold larger doubly charged particle. Therefore, the diameter, measured by the SMPS, is called electrical mobility diameter d_m , which is related to d_{ve} for singly charged particles using Eq. 3:

$$d_m = d_{ve} \cdot \frac{\chi_t}{C_C(d_{ve})}, \quad \text{Eq. 3}$$

where χ_t is the dynamic shape-factor in the transition regime. The size-dependent Cunningham Slip Correction Factor $C_C(d_{ve})$ describing the deviation in shape from a sphere and the effect of the drag force, respectively. χ_t also depends on $C_C(d_{ve})$ and both depend on Kn . However, neither χ_t nor $C_C(d_{ve})$ is known for ambient aerosol (DeCarlo et al., 2004).

The mass concentration c_m obtained by the SMPS is given in Eq. 4.

$$c_m = \rho_{eff} \cdot V(d_m) \cdot c_p, \quad \text{Eq. 4}$$

where $V(d_m)$ is the volume of a particle with mobility diameter d_m , ρ_{eff} the effective density, further explained in section 2.6.1 and c_p the particle number concentration, measured by the CPC. (DeCarlo et al., 2004)

2.5 **HR-ToF-AMS**

The High-Resolution Time-of-Flight AMS by Aerodyne Research (HR-ToF-AMS, Figure 5), presented by DeCarlo et al. (2006), is a further development of the Quadrupole AMS (Q-AMS), described by Jayne et al. (2000), and the Compact-ToF-AMS (CToF-AMS), described by Drewnick et al. (2005). Their functionalities are reviewed by Canagaratna et al. (2007). Briefly, the AMS is mainly used to quantify non-refractory (NR) compounds in the $PM_{1.5}$ fraction of an aerosol and to determine the particle size distribution (Canagaratna et al., 2007). NR-compounds are ammonium salts, primary and secondary organic aerosol species in the fine mode as mentioned in section 1.1. Furthermore, the HR-ToF-AMS allows the determination of the elemental composition of the organic fraction (Canagaratna et al., 2015; Aiken et al., 2008).

All three types of AMS consist of an aerodynamic lens system, a particle time-of-flight (PToF) chamber and a mass spectrometer. The mass spectrometer contains an ionization chamber with a vaporizer and an ionization source, typically electron impact (EI) ionization, and an analyzer. In the case of the HR-ToF-AMS, it is a time-of-flight MS from ToFwerk AG (H-TOF Platform, Thun, Switzerland), containing an extractor, an ion time-of-flight (iToF) chamber with an ion reflector, a hardmirror and microchannel plates (section 2.7.4) as detector. It is connected orthogonally to the EI source. The vacuum is about 1.5 Torr in the aerodynamic lens, about 10^{-5} Torr in the PToF chamber and about 10^{-8} Torr in the ionization chamber and the analyzer (DeCarlo et al., 2004), generated by five turbomolecular pumps (TP in Figure 5) and a diaphragm pump.

Instruments

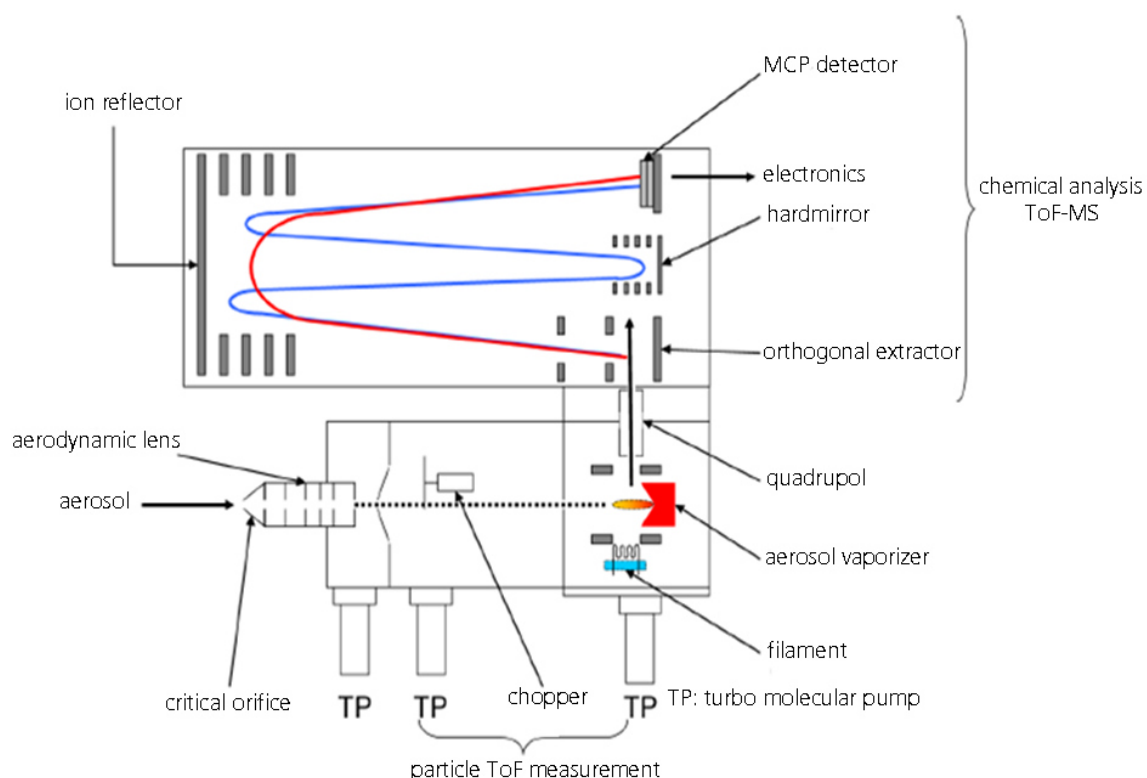


Figure 5: Schematic setup of an HR-ToF-AMS, based on DeCarlo et al. (2006).

The aerosol is sampled through a 100 μm critical orifice into the aerodynamic lens reducing the pressure strongly from ambient pressure to about 1.5 Torr. Hygroscopic droplets may dry during the transport through the lens (Zelenyuk et al., 2006). Particles with diameters between 35 nm and 1.5 μm are focused to a beam and accelerated due to the supersonic expansion into the PToF chamber (DeCarlo et al., 2006). The gas phase is removed by the vacuum pumps by a factor of 10^7 (Canagaratna et al., 2007). A chopper with two slits at an angle of 180° is placed at the beginning of the PToF chamber. It can be set to block the particle beam (*closed* position), to pass packages of particles through the slits during rotation (*chopped* position) and to pass the beam completely (*open* position). NR compounds of the particles evaporate in a few milliseconds on the resistively heated porous tungsten vaporizer in the ionization chamber. The vaporized compounds are ionized by EI ionization (Canagaratna et al., 2007). High fragmentation occurs due to the high temperature of 600 $^\circ\text{C}$ and due to the high ionization energy of 70 eV, with the result that most of the generated fragment ions have mass-to-charge (m/z) ratios below 100 (DeCarlo et al., 2006). Direct current transfer optics (quadrupole in Figure 5) supply the fragment ions in a collimated beam to the extractor. An orthogonal pulse accelerates them into the iToF chamber. The application of the ion reflector and the hard mirror leads to V- or W-shape trajectories of the ions (red and blue curves in Figure 5) towards the detector, respectively. As the time of flight from the extractor to the detector increases with increasing m/z , the ions are separated by their m/z ratio. The signals of the detector are 55 times amplified and sampled with an 8-bit analog-to-digital converter (ADC, ACP240, Aquiris, Geneva, Switzerland). The ADC co-averages the signals and transfers them to the PC RAM every few seconds, where the

Instruments

signals can be further averaged and saved according to user settings (DeCarlo et al., 2006).

The HR-ToF-AMS can be operated in three modes (DeCarlo et al., 2006). The MS mode is used to calculate the mass concentrations. In this mode, background mass spectra are measured at the *closed* position and subtracted from the spectra at the *open* position, forming the so-called *difference* spectra. The V- and W-mode are submodes corresponding to the respective ion trajectories in the iToF chamber. Some of the detected ions are specific for inorganic species such as nitrate, sulfate and ammonium (Allan et al., 2004), and the signals of these ions are used to calculate the concentrations of the respective species. Since there is no separation of the compounds and strong fragmentation occurs at the ionization, organic compounds cannot be identified without known specific ion. Their signals are usually grouped as “organic” species for the quantification (Canagaratna et al., 2007; Zhang et al., 2005). The general quantification is further described in section 2.5.3.

The particle size distribution is determined in the PToF mode with the chopper in the *chopped* position. The chopper device contains an LED and a photodiode giving the start signal when one of the slits interrupts the light barrier (Canagaratna et al., 2007). The particle packs contain only 1 – 4% (Canagaratna et al., 2007) of the total particle amount, which is why the mass concentrations are not measured in the PToF mode. The supersonic expansion from the aerodynamic lens into the PToF chamber leads to an acceleration of the particles, as the same force is applied to all particles. This leads to a decreasing acceleration and terminal velocity with increasing size, resulting in a separation of the particles. The arrival times of the particles are measured by the mass spectrometer as time series of the single ions during a chopper cycle (half-turn of the wheel). The advantage of this is that size distributions of individual species are obtained if an ion is specific for the respective component. The time of the particle detection by the ToF-MS within 30 μs is negligible to the particle time of flight of several milliseconds (DeCarlo et al., 2006) which is why EI-ToF-MS can be used as the detector for the particle time of flight. The particle time of flight is converted to the vacuum aerodynamic diameter d_{va} , which will be further explained in section 2.5.2.

The third mode is the “brute-force single-particle” (BFSP) mode with the chopper in the *chopped* position and normally used for the calibration of the mass concentrations (section 2.6.3). While the ADC co-averages several mass spectra in the MS- and PToF-mode, the mass spectra of every single chopper-cycle are saved in the BFSP mode allowing single particle counting. Single or several ions are selected. When the signals of the ions exceed a threshold during a chopper cycle, this is classified as one particle. For the calibration, the particle number concentration must be set low enough to ensure that only a single particle is detected during a chopper cycle. (DeCarlo et al., 2006; Field ToF-AMS Operation)

Further details of the single components and functionalities of the AMS are described in the subsections 2.5.1 to 2.5.4. The ions produced in the ion source will be labeled as [molecular formula]⁺ to distinguish them from compounds or fragments of molecules. Isotopes are labeled with the atomic weight as a superscript prefix if the

isotope does not have the highest abundance. The isotope with the highest abundance is called isotope parent. For example, $[C_3O]^+$ with three ^{12}C atoms and one ^{16}O atom is the isotope parent of $[^{13}CC_2O]^+$ with one ^{13}C , two ^{12}C and one ^{16}O atom. Furthermore, it is distinguished between the exact mass m and the unity or integer mass m_{unity} .

2.5.1 Aerodynamic lens

The aerodynamic lens consists of a cascade of multiple lenses in series and a nozzle at the end, where the particles enter into the PToF chamber (Liu et al., 1995a, 1995b). The particle-air mixture undergoes mass and size dependent axisymmetric contractions in the lenses and enlargements between them.

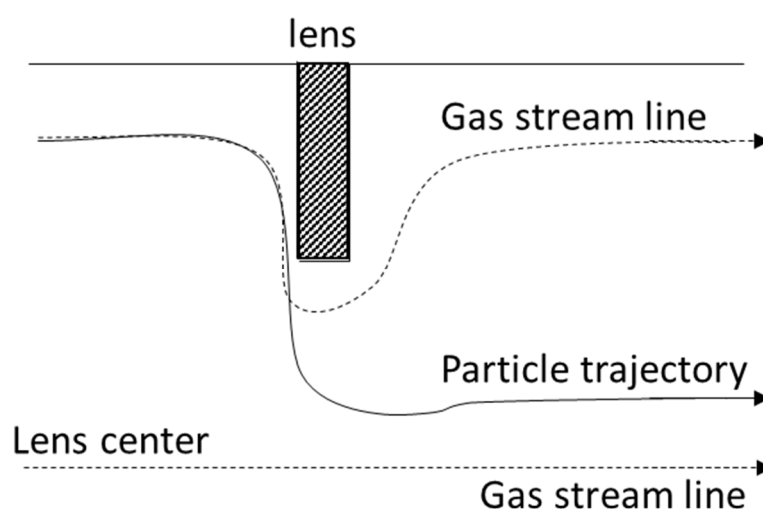


Figure 6: Trajectories in aerodynamic lenses (based on Zhang et al., 2002).

Figure 6 illustrates the trajectory of particles relative to the gas stream through a lens. The gas and the particles are accelerated when they approach the lens. The particles overshoot the gas because of its larger mass inertia. Now, they follow the gas streamlines closer to the center of the lens system. The smaller the particles, the lower are their inertias and the closer are their trajectories to the gas streamlines. Particles near the center remain at the center due to small radial drag forces (Liu et al., 1995a). There is a reduction of about 40% for particles with a diameter larger than 2500 nm because they impact the surface of the first lens due to their inertia (Zhang et al., 2004). Small particles with a diameter smaller than 15 nm follow the gas expansion strongly and are lost through the interception on the plate due to Brownian motion. 100% transmission is obtained for spherical particles with a radius of 70 to 500 nm (Canagaratna et al., 2007; Jayne et al., 2000). The cascade of lenses leads to a narrow particle beam, but Brownian motion and especially lift forces on non-spherical particles limit the final focusing capacity of the lens system (Liu et al., 1995a).

2.5.2 Particle Time-of-Flight

The particles are in the transition regime when they pass the aerodynamic lens and are accelerated due to drag forces into the free-molecular regime in the PToF chamber (DeCarlo et al., 2004). The terminal velocity is already reached after about 1 cm from the exit of the lens because collisions with gas molecules do not occur anymore in the

high vacuum region. The forces due to the mass inertia of the particles become equal to the opposite drag forces. The higher the mass, the higher are the inertia and the lower the acceleration. Particles with the same mass can have different volumes due to different particle densities ρ_p or/and internal voids but they have the same inertia. The drag force increases with a higher surface. An aspherical particle will have higher acceleration and terminal velocity than a spherical particle with the same mass. Therefore, the size distribution is given as a function of the vacuum-aerodynamic diameter d_{va} , which refers to a sphere with standard density ρ_0 of 1 g/cm³. The effect of irregular shapes in the vacuum is expressed as shape factor χ_v .

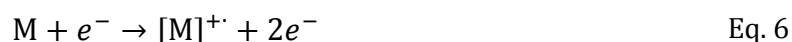
According to Jimenez et al. (2003), the physical diameter d_{ve} is connected to the vacuum-aerodynamic diameter d_{va} using Eq. 5.

$$d_{va} = \frac{\rho_p \cdot d_{ve}}{\rho_0 \cdot \chi_v} \quad \text{Eq. 5}$$

In general, neither ρ_p nor χ_v is known of ambient aerosol particles and the particle size distribution is given as a function of d_{va} .

2.5.3 EI mass spectrometry and quantification

The EI ionization in the gas phase is independent of matrix effects such as ion-molecule reactions due to the vacuum of 10⁻⁸ Torr (DeCarlo et al., 2006). The electrons are emitted from a tungsten filament and accelerated into the vapor. The ionization causes an abstraction of electrons, mostly one, from the vaporized molecules (M) and the molecular ions [M]⁺ are generated in a primary reaction (Skoog and Leary, 1996).



The electrons transmit a part of their kinetic energy to the molecules. Only a part of the energy transferred is needed for ionization. The molecular ions are in highly excited states due to the excess energy, resulting in their fragmentation. In many cases, multiple fragmentations and rearrangements, which can be used for structural analysis occur (Skoog and Leary, 1996).

According to Jimenez et al. (2003), the molecule flux M of one species s in the ionization region is linear to the ion (formation) rate $I(s,f)$ of a fragment ion f (Eq. 7).

$$M(s) = \frac{I(s, f)}{\chi(s, f) \cdot IE(s)}, \quad \text{Eq. 7}$$

where $\chi(s, f)$ is the fraction of the ion f of the total ion rate $\sum_{all\ f} I(s, f)$ of species s (Eq. 8), and $IE(s)$ is the ionization efficiency of species s . IE describes the ratio of molecules that are ionized compared to all molecules introduced into the ion source (ca. one of 10⁷ molecules (Skoog and Leary, 1996)).

$$\chi(s, f) = \frac{I(s, f)}{\sum_{all\ f} I(s, f)} \quad \text{Eq. 8}$$

The mass concentration $c_m(s)$ is calculated using Eq. 9.

Instruments

$$c_m(s) = \frac{M(s) \cdot MW(s)}{N_A \cdot Q} = \frac{MW(s)}{N_A \cdot Q} \cdot \frac{\sum_{all f} I(s, f)}{IE(s)}, \quad \text{Eq. 9}$$

where $MW(s)$ is the molecular weight of the species s , N_A is Avogadro's number and Q the sampling flowrate of the AMS.

Jimenez et al. (2003) pointed out that IE is proportional to the number of electrons in the molecule, which in turn is linearly dependent on MW of the molecule.

$$constant = \frac{MW(s)}{IE(s)} \quad \text{Eq. 10}$$

The ratio of the number of electrons to MW is very similar for typical aerosol compounds containing carbon, nitrogen, oxygen, sulfur and hydrogen. Since the ratios $MW(s)/IE(s)$ of all species are constant according to Eq. 10, the ratio of a species $s1$ can be expressed as a factor of the ratio of another species $s2$.

$$\frac{MW(s1)}{IE(s1)} = \frac{MW(s2)}{IE(s2)} \cdot RIE, \quad \text{Eq. 11}$$

where the factor is called relative ionization efficiency RIE .

There is no separation of single species before the ionization. The signals, specific to a species, are used to calculate the concentration of the respective species. Generally, IE is determined for nitrate (NO_3) during calibration and the concentration of other species is calculated by Eq. 12.

$$c_m(s) = \frac{MW(\text{NO}_3)}{N_A \cdot Q \cdot IE(\text{NO}_3)} \cdot \frac{\sum_{all f} I(s, f)}{RIE(s)} \quad \text{Eq. 12}$$

Organic compounds which yield the same fragments produce the same ions. Even molecular ions would not be distinguished from fragment ions in a mixture of compounds. Therefore, identification and quantification of single organic compounds without known specific fragments are impossible in ambient aerosols (Canagaratna et al., 2007). All organic material is grouped, called "organic". As IE and RIE are approximately the same for all organic species (organic s), the organic mass concentration is calculated from the total signal of all ions f , corresponding to the organic species, $\sum_{all \text{ organic } f} I(\text{organic } f)$ without knowing the chemical composition (Zhang et al., 2005; Jimenez et al., 2003; Canagaratna et al., 2007).

$$\begin{aligned} c_m(\text{organic}) &= \sum_{all \text{ organic } s} c_m(\text{organic } s) && \text{Eq. 13} \\ &= \frac{MW(\text{NO}_3)}{N_A \cdot Q \cdot IE(\text{NO}_3) \cdot RIE(\text{organic})} \cdot \left(\sum_{all \text{ organic } s} \sum_{\text{organic } f} I(\text{organic } s, f) \right) \\ &= \frac{MW(\text{NO}_3)}{N_A \cdot Q \cdot IE(\text{NO}_3) \cdot RIE(\text{organic})} \cdot \sum_{all \text{ organic } f} I(\text{organic } f) \end{aligned}$$

Several fragment ions originate from different species. For example, the ion $[\text{CO}_2]^+$ is produced by CO_2 and carboxylic acids (Canagaratna et al., 2007; Allan et al., 2004). The contribution of carbon dioxide is calculated by the relative concentration of CO_2 to N_2 in ambient air and is subtracted from the total signal of $[\text{CO}_2]^+$ to get its contribution from the carboxylic acids. One advantage of EI is that the mass spectra

are very robust and reproducible. The fraction $\chi(s, f)$ is constant (Eq. 8), which means that the ratios of the intensities between different fragment ions of the same species are constant as well. The ratios of the intensities of $[\text{CO}_2]^+$ to $[\text{CO}]^+$ and of $[\text{CO}_2]^+$ to $[\text{H}_2\text{O}]^+$, generated at EI of carboxylic acids, are about 1:1 and 1:0.25 (Allan et al., 2004). $[\text{CO}]^+$ has the same integer mass of 28 as $[\text{N}_2]^+$, which is detected with high intensity because of the large amount of nitrogen in the air. $[\text{H}_2\text{O}]^+$ originates from water and also from ammonium sulfate. Therefore, the contributions of $[\text{CO}]^+$ and $[\text{H}_2\text{O}]^+$ to $\sum_{\text{all organic } f} I(\text{organic } f)$ are calculated from the $[\text{CO}_2]^+$ signal and the respective ratios to $[\text{CO}_2]^+$ from carboxylic acids. (Canagaratna et al., 2007; Allan et al., 2004)

Several particle losses occur between the AMS inlet and the vaporizer and depend on the aggregate state and shape of the particles (Huffman et al., 2005; Matthew et al., 2008; Middlebrook et al., 2012). Aspheric particles have a lower transmission efficiency in the aerodynamic lens. Solid particles suffer rather from a higher bounce-off at the vaporizer. The loss is expressed as collection efficiency (CE). The mass concentration of an aerosol species is calculated as follows (Canagaratna et al., 2007):

$$c_m(s) = \frac{10^{12} \cdot MW(\text{NO}_3)}{N_A \cdot Q \cdot IE(\text{NO}_3)} \cdot \frac{\sum_{\text{all } f} I(s, f)}{RIE(s) \cdot CE} , \quad \text{Eq. 14}$$

where 10^{12} is a conversion factor to $\mu\text{g}/\text{m}^3$.

The generated ions are accelerated and focused into an ion beam towards the extractor. The velocity of the ions decreases with an increasing mass-to-charge ratio. Larger ions remain for a longer time in the extraction region than smaller ions. This is why the ion rate at the microchannel plate (MCP) detector (I_{MCP}) of an ion with a certain m/z ratio is normalized to 28 ($[\text{N}_2]^+$). I_{MCP} is obtained by the determination of the single-ion area SI , which is the detection rate S_{MCP} of a single ion, estimated by low abundant signals of background species. The ion rate of a single ion f with a certain m/z is calculated using Eq. 15 (Freutel, 2012; Hings, 2006).

$$I(f) = I_{\text{MCP}}(f) \cdot \sqrt{\frac{28}{m/z}} = \frac{S_{\text{MCP}}(f)}{SI} \cdot \sqrt{\frac{28}{m/z}} \quad \text{Eq. 15}$$

2.5.4 ToF mass spectrometry and mass resolution

The ions are separated by their m/z ratios in the mass analyzer. In a ToF-MS, all ions from the ion source are detected according to their time of flight, and discrete packs of ions are supplied into the iToF chamber. However, the EI source produces ions continuously, therefore the ion packs are introduced by an electric pulse orthogonally to the source. (de Hoffmann and Stroobant, 2007).

As described by de Hoffmann and Stroobant (2007), the detection of ion f with a certain $m/z(f)$ depends on the time of flight $t(f)$ from the extractor to the detector. An electric pulse of an electrical energy E_V accelerates the ions from the extractor into the iToF-chamber.

Instruments

$$E_V = e \cdot z(f) \cdot U, \quad \text{Eq. 16}$$

where e is the elementary charge, $z(f)$ the number of charges of the ion f and U the voltage of the electric field. E_V is transformed into the kinetic energy E_{kin} of the accelerated ions.

$$E_{kin} = \frac{1}{2} \cdot m(f) \cdot v(f)^2, \quad \text{Eq. 17}$$

where $m(f)$ and $v(f)$ are the exact mass and velocity of the ion f . Since the electric energy is equal to the kinetic energy (Eq. 18) and the ion velocity in the iToF chamber is calculated using Eq. 19, $m/z(f)$ is determined using Eq. 20.

$$E_V = E_{kin} \quad \text{Eq. 18}$$

$$v = \frac{L}{t}, \quad \text{Eq. 19}$$

$$\frac{m}{z}(f) = \frac{2 \cdot e \cdot U}{L^2} \cdot t(f)^2, \quad \text{Eq. 20}$$

where L is the pathway from the extractor to the detector. The mass resolution R describes the ability of a mass analyzer to separate ions. It is defined according to Eq. 21 (de Hoffmann and Stroobant, 2007).

$$R = \frac{m_{\text{unity}}}{\Delta m} = \frac{t}{2 \cdot \Delta t}, \quad \text{Eq. 21}$$

where m_{unity} is the integer or unity mass and Δm is the full width at half maximum.

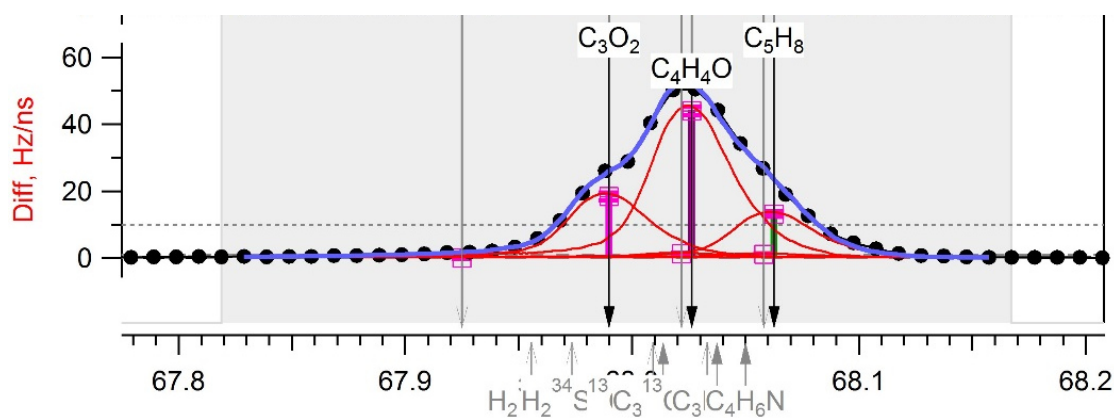
The ion reflector and the hard mirror (Figure 5) give two advantages to increase the mass resolution. Firstly, they extend the pathway L to 1.3 m and 2.9 m compared to a linear setup or the CToF-AMS. Secondly, the ions have different initial positions in the extractor leading to different kinetic energies and velocities of the ions in the iToF chamber. The higher the initial velocity, the deeper the ions enter the reflector and the longer is the path to the detector. Therefore, identical ions with different positions in the pulse direction have the same time of flight. The mass resolution is 2100 for the V-mode and 4300 for the W-mode (DeCarlo et al., 2006; de Hoffmann and Stroobant, 2007).

Figure 7 illustrates the raw signal (black dots) of the *difference (diff)* mass spectra at the integer mass of 68 in a) V- and b) W-mode. The *diff* mass spectra are obtained by subtracting the background mass spectra from the mass spectra with the chopper in the *open* position. The raw signal is the linear combination of signals of ions with the same integer mass. All signals are peaks of Gaussian shape. The goal of the data processing is to choose ions (the chosen ions in Figure 7 are highlighted in boldface), whose signals fit together the raw signal, indicated as the blue line. In the case of Figure 7, the raw signal is resolved as three individual peaks in the W-mode, making it easier to select the corresponding ions than in the V-mode. In contrast, the intensity of the signal is much smaller in the W-mode than in the V-mode due to the higher loss of ions on the longer trajectory. Generally, isotopes must be considered when

Instruments

choosing the combination of ions. For example, the ion $[^{13}\text{CC}_3\text{H}_3\text{O}]^+$ has the integer mass of 68. Its signal is calculated from the peak area of the parent isotope $[\text{C}_4\text{H}_3\text{O}]^+$ and the natural isotope abundance. The calculated signal of ion $[^{13}\text{CC}_3\text{H}_3\text{O}]^+$ is subtracted automatically from the raw signal at its exact mass (DeCarlo et al., 2006).

a)



b)

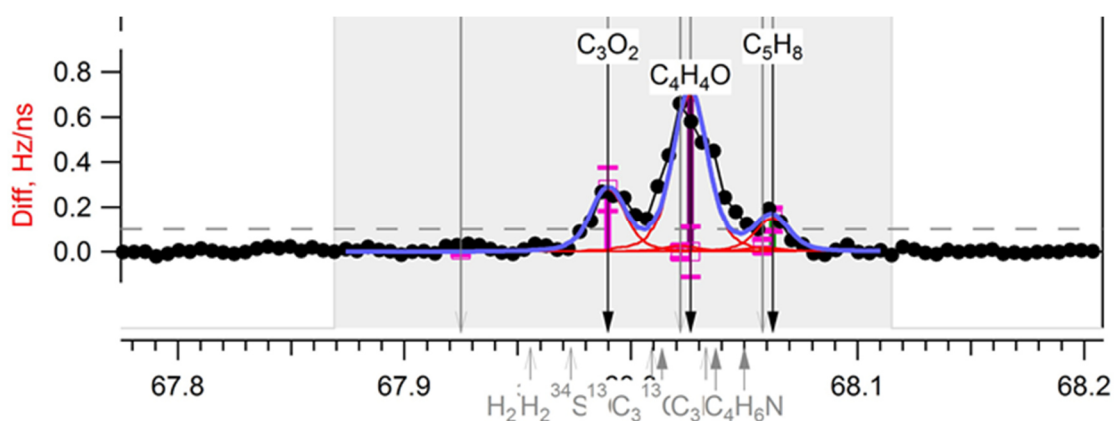


Figure 7: Difference (Diff) mass spectra, obtained by subtraction of the mass spectra with chopper in *closed* position from the mass spectra with the chopper is in *open* position. Raw signal (black dots) of the integer mass 68 and the fit (blue) obtained by choosing single fragment ions with the same nominal mass a) in V-mode b) in W-mode. The fit is a superposition of the peak areas (red) of the chosen ions. The horizontal line at the signal intensity of 0 is the baseline.

The m/z calibration is performed using signals of background species, measured in the *closed* position of the chopper. Three ion species, typically $[\text{H}_2\text{O}]^+$, $[\text{N}_2]^+$ and $[\text{W}]^+$, are used for calibration during the measurement, while the calibration can be extended with other isolated ions during data processing (Field ToF-AMS Operation). The m/z ratio is fitted to a power-law function so that m/z ratios can be determined outside of the calibration range (DeCarlo et al., 2006). The peak width and shape are calibrated from peaks of isolated ions with the known exact mass in the background spectra. This allows the determination of peak areas of overlapping peaks, as can be seen for the ions $[\text{C}_3\text{O}_2]^+$, $[\text{C}_4\text{H}_4\text{O}]^+$ and $[\text{C}_5\text{H}_8]^+$ in Figure 7a). When the mass spectrum is shown at unit mass resolution, the total area under the raw signal, marked with a grey background, is calculated. Normally, peaks are not expected in the area with the white background at ambient air, so that this area can be used to recalculate the baseline of the peaks (red line in Figure 7) (Field Data Analysis Guide).

2.6 Calibration of the AMS

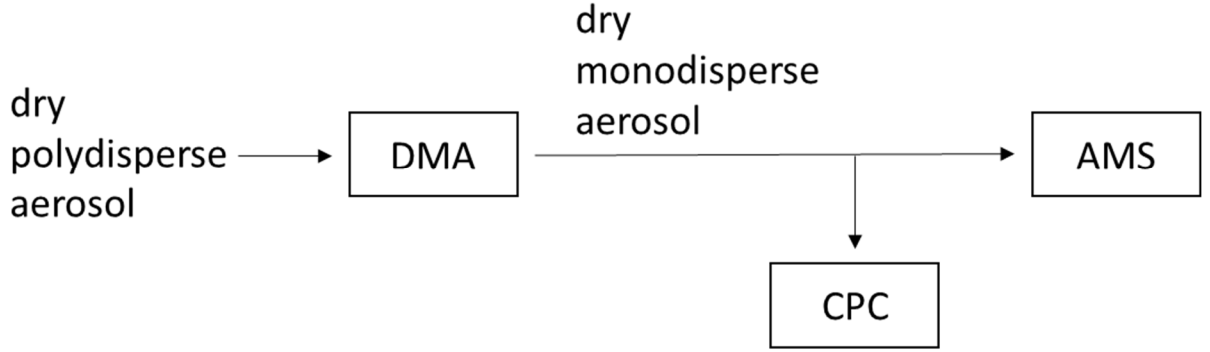


Figure 8: Schematic setup of tandem DMA-AMS for the calibration.

2.6.1 Density

It is important to generate an aerosol with known diameter and composition of the particles to calibrate the size distribution and the mass concentration of the AMS. A tandem DMA-AMS setup is frequently used for this purpose (Figure 8). Particles with a mobility diameter d_m are selected using the DMA. The mobility diameter is connected to the particle mass m_p by Eq. 22.

$$m_p = \rho_{eff} \cdot V_p(d_m), \quad \text{Eq. 22}$$

where ρ_{eff} is the effective density and $V_p(d_m)$ the particle volume with mobility diameter d_m assuming a spherical volume (Eq. 23).

$$V_p = \frac{\pi}{6} \cdot d_m^3 \quad \text{Eq. 23}$$

The effective density ρ_{eff} includes the deviation from the spherical volume (Zelenyuk et al., 2008). If the particles contain only one single species s , the mass concentration $c_m(s)$ at the inlet of the AMS can be calculated using Eq. 24.

$$c_m(s) = m_p \cdot c_p, \quad \text{Eq. 24}$$

where c_p is the particle number concentration measured by the CPC.

However, knowledge about ρ_{eff} and the relationships between physical, mobility and vacuum-aerodynamic diameters (Eq. 3 in section 2.4 and Eq. 5 in section 2.5.2) are required to calculate m_p .

According to Jayne et al. (2000) and DeCarlo et al. (2004), the relationship between mobility and vacuum-aerodynamic diameter of spherical and mildly aspherical particles is given in Eq. 25.

$$d_{va} = S \cdot \frac{\rho_m}{\rho_0} \cdot d_m, \quad \text{Eq. 25}$$

where S is the Jayne shape factor. The bulk material density ρ_m is equal to the particle density ρ_p if no voids are in the particles. The Jayne shape factor S equals one for spherical particles. In addition, DeCarlo et al. (2004) demonstrated the relationship between the effective and material density (Eq. 26).

$$\rho_{eff} = S \cdot \rho_m \quad \text{Eq. 26}$$

For a few compounds like ammonium nitrate, S and ρ_m are known (Canagaratna et al., 2007; Jayne et al., 2000), so that those species can be used to calibrate the particle time-of-flight and the mass concentration. Based on the calibration with ammonium nitrate, ρ_{eff} of other compounds and mixtures like SOA from the ozonolysis of α -pinene (Zelenyuk et al., 2008) can be determined using Eq. 25 and Eq. 26. The obtained ρ_{eff} can be used to calculate the mass concentration using the SMPS (Eq. 4 in section 2.4).

Furthermore, ρ_{eff} depends on the particle size and shape for non-spherical particles. The measurement of the d_{va} - size distribution of a DMA selected aerosol provides information about particle shape and density (Slowik et al., 2004; Zelenyuk et al., 2006; Zelenyuk et al., 2008). For example, asymmetric particles will have a different orientation in the gas streamline in the aerodynamic lens, which influences the draft forces on the particles and the particle time of flight, resulting in a broader size distribution than for spherical particles (Zelenyuk et al., 2008). Zelenyuk et al. (2006) observed size-dependent ρ_{eff} of particles containing dry sodium chloride, ammonium sulfate and organic compounds. The effective density was constant for spheres but decreased with increasing mobility diameter for cubes and agglomerates. Both pure inorganic compounds showed aspherical behavior, while the mixture of ammonium sulfate with the organic species and the pure organic species showed spherical behavior.

2.6.2 PToF

As mentioned in section 2.6.1, the Jayne Shape factor and the material density are well known for ammonium nitrate, which can be used for the calibration of the size distribution using the tandem DMA-AMS setup. Alternatively, monodisperse polystyrene latex spheres (dynamic shape factor equals one (DeCarlo et al., 2004)) with known physical diameter d_{ve} and density (Jayne et al., 2000) (eq. Eq. 25 in section 2.6.1) can be used. In both cases, the aerosol is produced from nebulized aqueous solutions or suspensions and dried by denuders containing silica (Field ToF-AMS Operation).

The particle velocity v_{PToF} in the PToF chamber is calculated by the measured particle time of flight t_{PToF} and the path length L_{PToF} of 29.5 cm (Field ToF-AMS Operation) between the chopper and the ionization chamber using Eq. 19 in section 2.5.4. The particle velocity is plotted to d_{va} , obtained from Eq. 25 in section 2.6.1 and Eq. 5 in section 2.5.2, respectively and fitted using Eq. 27 (Allan et al., 2003).

$$v_{PToF} = v_{lens} + \frac{v_{gas} - v_{lens}}{1 + \left(d_{va}/d^*\right)^b} \quad \text{Eq. 27}$$

d^* and b are empirical parameters. The gas velocity in the aerodynamic lens v_{lens} is about 15 m/s at 1.4 Torr. The gas velocity at the exit of the lens v_{gas} can be calculated from the nitrogen signal at the integer mass of 28.

2.6.3 Mass concentration

According to Eq. 9 in section 2.5.3, the mass concentration $c_m(s)$ of a species s is calculated from the sum of the ion rates $\sum_{\text{all } f} I(s, f)$ of all ions f , which are produced

Instruments

during ionization of the species s , using the ionization efficiency IE (Jimenez et al., 2003).

As pointed out, IE of one species can be converted to an IE of another species using the relative ionization efficiency RIE (Eq. 11 in section 2.5.3), and the $IE(\text{organic } s)$ of organic compounds are approximately equal. Therefore, the calibration has to be done only for one species, typically nitrate from ammonium nitrate particles (Canagaratna et al., 2007).

A DMA-AMS setup is applied with additional CPC (Figure 8) for the IE calibration. The particles must contain only one single compound, which is completely vaporized in the ionization chamber, as assumed for ammonium nitrate (Canagaratna et al., 2007). The molecule flow $M(s)$ is connected to the mass concentration $c_m(s)$ measured by the AMS, using Eq. 7 to Eq. 9 in section 2.5.3. The mass concentration measured by the AMS is equal to the mass concentration measured by the SMPS, using Eq. 22 to Eq. 26 in section 2.6.1. The $IE(s)$ of a species s can be calculated using Eq. 28.

$$IE(s) = \frac{\sum_{\text{all } f} I(s, f)}{N_A \cdot Q} \cdot \frac{\rho_0 \cdot 6}{c_p \cdot S \cdot \rho_m \cdot \pi \cdot d_m^3} \quad \text{Eq. 28}$$

If the fraction $\chi(s, f)$ of an ion f to $\sum_{\text{all } f} I(s, f)$ is known (Eq. 8 of section 2.5.3), the ion rate $I(s, f)$ can be used to calculate $IE(s)$ (Eq. 29) or can be integrated as $IE(s, f)$ (Eq. 30).

$$IE(s) = \frac{I(s, f)}{\chi(s, f) \cdot N_A \cdot Q} \cdot \frac{\rho_0 \cdot 6}{c_p \cdot S \cdot \rho_m \cdot \pi \cdot d_m^3} \quad \text{Eq. 29}$$

$$IE(s, f) = \chi(s, f) \cdot IE(s) = \frac{I(s, f)}{N_A \cdot Q} \cdot \frac{\rho_0 \cdot 6}{c_p \cdot S \cdot \rho_m \cdot \pi \cdot d_m^3} \quad \text{Eq. 30}$$

Using the MS/CPC-method, $\sum_{\text{all } f} I(s, f)$ is measured in the MS mode of the AMS and c_p is measured using the CPC. The mobility diameter d_m is selected using the DMA. Alternatively, the BFSP mode (section 2.5) can be used for calibration. The particle number concentration must be low enough in order to detect only one particle per chopper cycle. $\sum_{\text{all } f} I(s, f)$ refers to the number of ions per particle, IPP , and c_p equals 1 particle/cm³ in Eq. 28 to Eq. 30. The BFSP mode brings the advantage that the collection efficiency does not have to be considered (Eq. 14 in 2.5.3). Furthermore, d_m -size selected aerosol also contains multiple charged particles with the same d_m , which are detected separately by the AMS because of their different d_{va} . The contribution of multiply charged particles to $I(s, f)$ must be negligibly low compared to the contribution of the singly charged particles of interest in the MS/CPC method and their size distribution should not overlap with those of single charged particles in the BFSP mode (Field ToF-AMS Operation).

The ionization efficiency of all compounds depends on the sensitivity of the detector and ion losses on the way from the ionization chamber to the detector. Stronger fluctuations and successive changes in the sensitivity can be corrected by the so-called airbeam (AB), which is the ion rate of the integer masses 28 and 32 produced by

nitrogen and oxygen (Canagaratna et al., 2007). The IE for an actual measurement is (Field ToF-AMS Operation) given in Eq. 31.

$$IE_{\text{actual}} = \frac{IE_{\text{calibration}}}{AB_{\text{calibration}}} \cdot AB_{\text{actual}} \quad \text{Eq. 31}$$

This relationship is also used to calculate the IE for the W-mode (Field ToF-AMS Operation).

2.7 Mass spectrometer with soft ionization sources

For online application, mass spectrometers with atmospheric-pressure chemical ionization (APCI) and aerosol flowing atmospheric-pressure afterglow (AeroFAPA) source, respectively, were also used (Hoffmann et al., 1998; Brüggemann et al., 2015). In contrast to the EI source of the AMS, ionized molecules fragment rarely at these two soft ionization sources, because excess energy from the ionization process is transferred to surrounding gas-molecules by collision (Mitchum and Korfmacher, 1983). The detected signals correspond to the molar mass or molecular formula, providing information about single compounds. Both ion sources can be hyphenated to quadrupole ion trap (IT) mass analyzers.

2.7.1 APCI

The atmospheric-pressure chemical ionization (APCI) utilizing a corona discharge was developed by Carroll et al. (1975) and described for online application by Hoffmann et al. (1998). It consists of a ceramic inlet tube as inlet, a vaporizer tube, a corona discharge needle and two outlets (Figure 9). The aerosol exits the sample tube through a nozzle and is optionally mixed with a sheath gas in the heated vaporizer tube. Particle species are evaporated depending on the temperature and their volatility. Only species in the gas phase are ionized and detected. A high voltage of several kV is applied to the corona needle so that electrons are emitted in the discharge region around the needle. The main components of the air, such as nitrogen and oxygen, are ionized by EI to primary ions, nitrogen forming positive ions and oxygen forming negative ions. The respective charges are transferred from nitrogen or oxygen to water molecules by intermediate reactions, forming clusters of oxonium or superoxide ions with several water molecules (Horning et al., 1973; Sekimoto and Takayama, 2011). These clusters finally protonate or deprotonate the aerosol species. One of the outlets, which is close to the corona needle, is connected to the mass analyzer. The other outlet is placed perpendicular to the vaporizer tube and is connected with an additional pump supporting aerosol sampling.

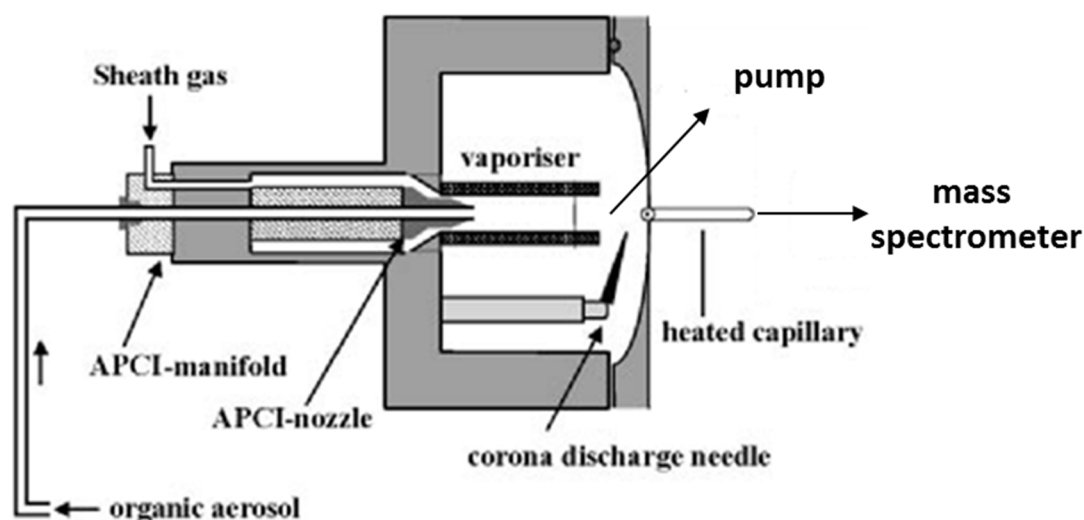


Figure 9: Schematic setup of online APCI-MS, modified reprint from Warscheid and Hoffmann (2001).

The ionization rate and sensitivity depend on external parameters, such as the sample and sheath flow rates, the position of the sample tube and the vaporizer temperature, but also on the affinity of the respective species to get protonated or deprotonated (Hoffmann et al., 1998). For example, carboxyl groups rather form negative ions, carbonyl groups rather form positive ions (Reinnig et al., 2009). Therefore, aerosol components are usually not determined quantitatively due to the lack of appropriated calibration methods and standards. In some cases, fragmentation due to the ionization is observed, as for hydroperoxides, where H_2O_2 is eliminated from the protonated molecular ion (Reinnig et al., 2008). However, the quasi-molecular ion $[\text{M}+\text{H}]^+$ or $[\text{M}-\text{H}]^-$ usually gives the most intensive peak in the mass spectrum (Hoffmann et al., 1998).

2.7.2 AeroFAPA

In the aerosol flowing atmospheric-pressure afterglow (AeroFAPA) ionization source (Figure 10), the aerosol particles are supplied into the afterglow region of a helium plasma, where the compounds are chemically ionized (Brüggemann et al., 2015). The ion source design is based on the pin-to-capillary FAPA, described by Shelley et al. (2011).

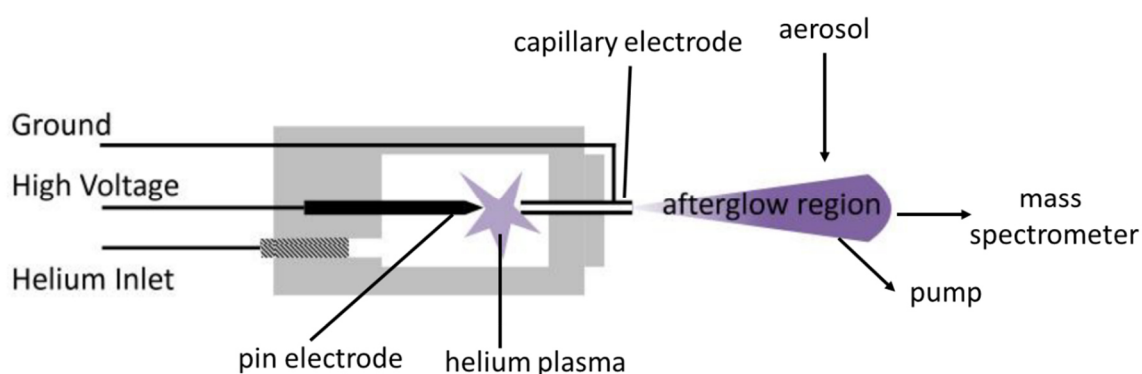


Figure 10: Schematic FAPA setup (Reprinted (adapted) from Brüggemann et al. (2015)).

Instruments

The aerosol inlet, the afterglow exit and the inlet of the mass analyzer must be placed orthogonally to each other. An additional pump, added next to the afterglow region, sets the sampling flowrate. The inlet is heated to vaporize the aerosol species before the ionization. The ion source consists of a ceramic chamber with two stainless steel electrodes and a helium inlet. The outlet to the afterglow region is the anode as a small capillary (outer diameter 3.18 mm, inner diameter 1.40 mm). The cathode is a pin (outer diameter 3.00 mm) with a negative potential of 15 V. By glow discharge, the helium atoms become excited or ionized and leave the discharge chamber into the afterglow region. Similarly, as in the APCI source (section 2.7.1), several charge-transfer reactions with ambient nitrogen, water and oxygen result in a protonation or deprotonation of the aerosol compounds. In general, the quasi-molecular ions $[M+H]^+$ and $[M-H]^-$ are the peaks of the highest intensity in the mass spectra. However, other species, produced in the afterglow region, can form adducts or may react with aerosol components. Brüggemann et al. (2015) observed the formation of nitrate as a primary ion, but the adducts with aerosol components had even integer m/z ratios and could be distinguished from the $[M-H]^-$ with uneven integer m/z ratios. Furthermore, tricarboxylic acids were esterified with methanol during the ionization. Oxidation products of fatty acids detected in the positive mode were explained by the incorporation of elemental oxygen during the ionization. Brüggemann et al. (2016) further investigated the ionization pattern for different functional groups by introducing the compounds of interest into the afterglow region by desorption from a glass slide in front of the ion source. In the positive and negative mode, loss of molecules such as H_2O , CO and CO_2 , formation of different adducts with O , O_2 , NO_2 and NO_3 , and oxidation products were observed. As in the APCI, the ionization efficiency of a molecule depends on the ability to get protonated or deprotonated, but also on the setup conditions, which is why a quantification of aerosol species in aerosol mixtures is usually not done. However, the mass spectra are generally dominated by $[M+H]^+$ and $[M-H]^-$ ions, so time curves of the uncalibrated signals of single aerosol components can be monitored representing the relative temporal variation of the respective components.

2.7.3 Ion trap

The quadrupole ion trap, as described at Stafford et al. (1984) and Yoshinari (2000), consists of one ring electrode and two perforated end cap electrodes, where the ions enter or leave the trap to the detector (Figure 11), respectively. The detector is usually an electron multiplier with a conversion dynode (section 2.7.4). The ions are injected from the ion source passing a skimmer, octopoles and a gating lens, which controls the number of ions in the trap. The vacuum is provided by differential pumping (de Hoffmann and Stroobant, 2007).

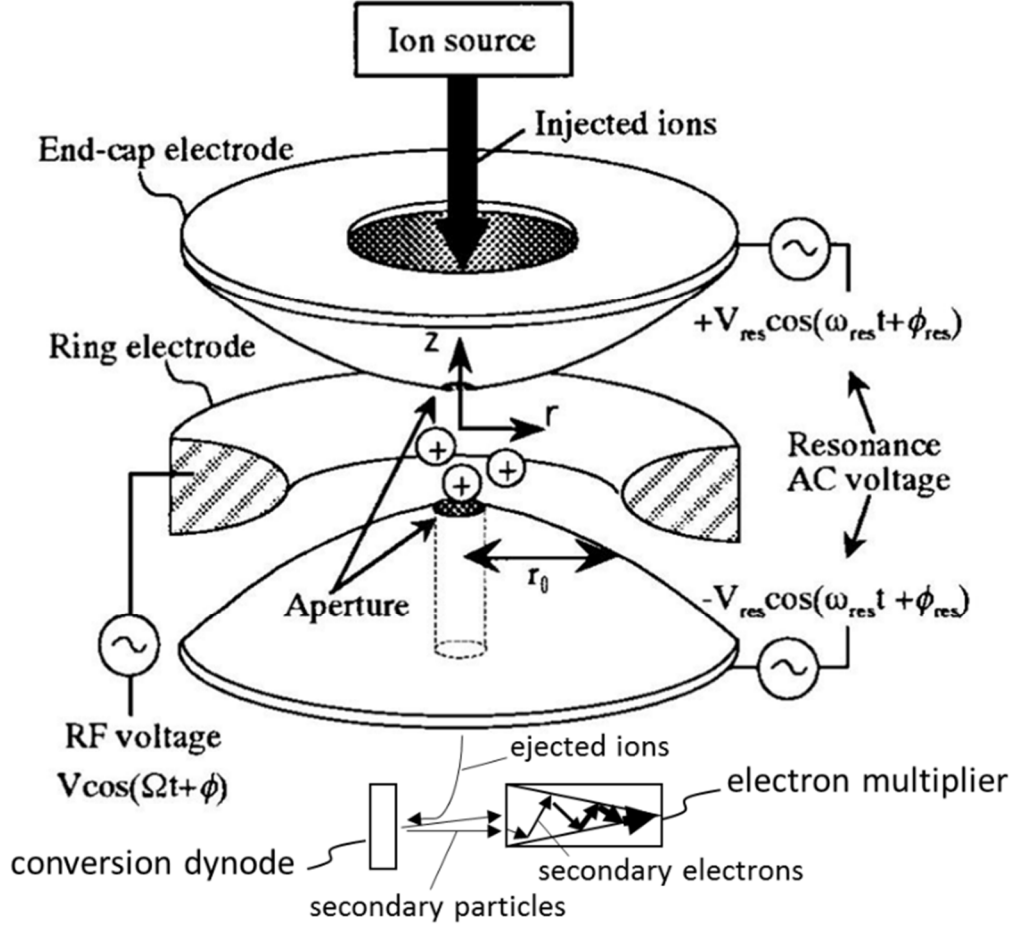


Figure 11: Scheme of a quadrupole ion trap, modified from Yoshinari (2000).

A superposition of an alternating current, direct current and a resonance frequency trapping voltage creates a three-dimensional electric field between the electrodes. The Mathieu equation describes the ion movements in this field, with the Mathieu parameters a_u (Eq. 32) and q_u (Eq. 33) depending on the inner radius of the ring electrode r_0 , the distance of the end cap electrodes from the center z_0 , the voltages U and V , the angular frequency of oscillating ν , ω , the angular velocity and m/z of an ion.

$$a_u = \frac{-16 \cdot z \cdot e \cdot U}{m \cdot r_0^2 + z_0^2 \cdot \omega^2} \quad \text{Eq. 32}$$

$$q_u = \frac{8 \cdot z \cdot e \cdot V}{m \cdot r_0^2 + 2 \cdot z_0^2 \cdot \omega^2} \quad \text{Eq. 33}$$

$$\omega = 2 \cdot \pi \cdot \nu \quad \text{Eq. 34}$$

There is a stability area at certain values of a_u and q_u where the ions within a certain m/z range are oscillating in stable orbits. The direct voltage U is often set to zero and the scanning of the m/z ratio is performed by increasing the resonance frequency voltage V . There is a threshold of q_u , when the ion movement becomes unstable in z_0 direction and the ions move towards both end cap electrodes. Since V increases, ions of smaller m/z ratio exceed the threshold and are detected earlier than ions of greater

Instruments

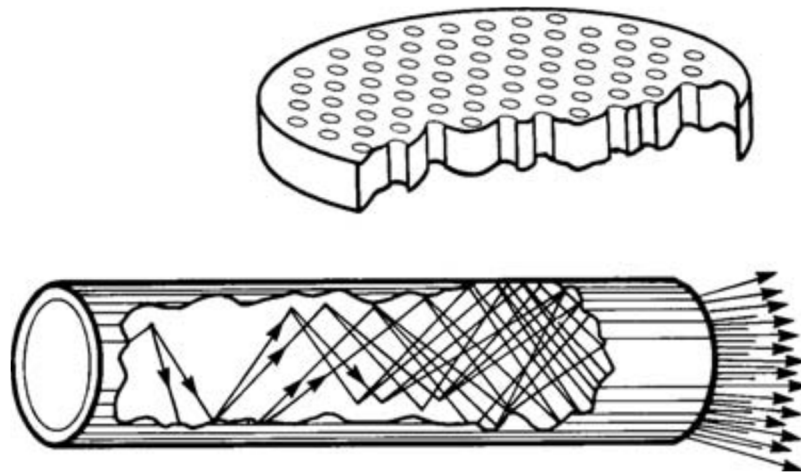


Figure 12: Cross-section of a microchannel plate and visualization of the electron multiplication (Reprint from de Hoffmann and Stroobant, 2007).

m/z ratio. The initial resonance frequency voltage sets the minimum of the m/z -range, while the highest applied voltage limits its maximum.

A light gas, such as helium or hydrogen, is added into the ion trap to a pressure of about 10^{-3} torr. The gas dampens the ion motions resulting in a more focused ion packs and smaller orbits of the ions. This enhances the mass resolution and the sensitivity by compacting the ion packs and diminishing the loss of ions through the impact on the electrodes (de Hoffmann and Stroobant, 2007).

In the so-called time-dependent tandem MS, also called MS/MS or MS^n experiment, the ions with the mass of interest must be isolated. Therefore, ions with differing masses are removed by applying their respective resonance or ejection frequencies on the end cap electrodes. The isolated ions with the m/z ratio of interest are kinetically accelerated to their resonance excitation. The collisions with the gas lead to the fragmentation of the ions (collisional induced dissociation, CID). The fragmentation pattern principally allows structural analysis of the isolated ions. For example, carboxylic acids show the elimination of a CO_2 fragment. A fragment ion can be isolated and fragmented again giving further information about the structure of the compound (de Hoffmann and Stroobant, 2007; Vogel, 2014).

2.7.4 Electron multipliers

HR-ToF-AMS (section 2.5) and ion trap instruments (section 2.7.3) both possess electron multipliers as detectors. The ions from the mass analyzer or secondary particles from a conversion dynode strike a surface of the cathode leading to the emission of secondary electrons, which are accelerated towards the anode. In a channel electron multiplier, the cathode can be a funnel-like resistor with increasing voltage towards the anode (Ayres and Heather, 1999). The emitted electrons strike the inner wall, leading to the emission of further electrons. In this way, a cascade of electrons is created, leading to a current amplification by a factor of 10^2 – 10^4 at the anode (de Hoffmann and Stroobant, 2007).

In Figure 11, the electron multiplier is placed opposite of the concave-shaped dynode, and the ion beam from the mass analyzer passes between the multiplier and the dynode. This off-axis position is needed to avoid that the neutral molecules from the analyzer collide with the cathode surface of the electron multiplier. The ions are attracted by the dynode. The collision with the dynode surface induces the emission of secondary particles, including electrons, charged or neutral molecules (Ayres and Heather, 1999).

The microchannel plates (Figure 12) in the HR-ToF-AMS contain several parallel channel electron multipliers allowing the detection of ion beams without focalization. The cathodes are cylindrical tubes, coated with a semiconductor. A metal blade as anode behind the tubes collects all emitted secondary electrons. The short electron path in the tubes provides a fast response time, suitable for the iToF analyzer. Several plates can be connected in series providing amplification of 10^8 (de Hoffmann and Stroobant, 2007).

3 Online redox derivatization for peroxide analysis

3.1 Introduction

Peroxides are assumed to play an essential role in SOA (secondary organic aerosol) formation and aging, including participation in particle new formation (Zhou et al., 2018; Li et al., 2016a; Riva, 2016; Ehn et al., 2012). Besides their effects on the formation of SOA, particle-phase peroxides are speculated to cause adverse health effects since they are a major fraction of those chemical constituents with oxygen atoms that are highly reactive, the so-called reactive oxygen species (ROS) (Zhou et al., 2018; Tong et al., 2017; Lakey et al., 2016).

Organic peroxides are formed by oxidation of volatile organic compounds in the gas phase (Zhou et al., 2018; Atkinson, 2000). Compounds with hydrocarbon chains react with OH radicals and ozone, forming carbon radicals. These radicals react with elemental oxygen to peroxy radicals, which form hydroperoxides by abstraction of hydrogen from another part of the hydrocarbon chain. The new radical groups on the hydrocarbon chain react further with oxygen. In this circle, highly oxidized molecules (HOM) are formed (Rissanen et al., 2014). It is assumed that they contain several peroxy groups, enabling a strong contribution to the particle new formation (Tu et al., 2016; Ehn et al., 2012). Alternatively, peroxides are formed by the recombination of (hydro)peroxy radicals (Guo et al., 2014), suggested as the major source (Zhao et al., 2013b), or the reversible reaction of hydroperoxides with aldehydes and ketones to peroxyhemiacetals and peroxyhemiketals. The gas-particle partitioning by absorption or condensation may be the major uptake of peroxides in the particle phase. Their sinks are the reaction with SO₂ (Guo et al., 2014; Faust et al., 1993; Atkinson, 2000; Ye et al., 2018) and photolytic decomposition in hydroxyl and alkoxy radicals (Epstein et al., 2014).

However, the formation and reactions of peroxides with other components in the particle phase are not well known (Claflin et al., 2018; Riva et al., 2017). They can be formed by disproportionation of solvated hydroperoxy or organic peroxy radicals (Jackson and Hewitt, 1999) or by secondary autoxidation processes, initiated by the absorbed primary peroxide products. Peroxyhemiacetals can be formed as the adduct of hydroperoxides to aldehydes (Zhao et al., 2013b; Ziemann, 2003; Docherty et al., 2005). Inter- and intramolecular autoxidation processes of fats and oils (Gotoh et al., 2011; Wang et al., 2016; Nakamura and Maeda, 1991), which are emitted as primary aerosols during cooking and roasting (McDonald et al., 2012; Rogge et al., 1991), could be also a source for hydroperoxide groups in the particle phase.

Generally, peroxides are very explosive because of the thermally labile oxygen-oxygen bond (Epstein et al., 2014). Commercially available standards often have to be stabilized, e.g. benzoyl peroxide with water. Peroxy groups oxidize alcohols, aldehydes and ketones to aldehydes, carboxylic acids and esters, respectively (Claflin et al., 2018). Rearrangements, such as the Hock or Baeyer-Villiger reactions, are often involved in oxidation reactions (Yaremenko et al., 2016). Epoxides can be formed by the reaction of peroxides and the double bond of alkenes (Surratt et al., 2010).

detected via AMS. The technique is called *online redox derivatization-AMS* (ORD-AMS). SOA as test aerosol is generated by the ozonolysis of monoterpenes. According to the literature, the formation of particle phase peroxides is expected in this process. As only condensed TPP can be detected by the AMS, a seed aerosol of unreactive ammonium sulfate (AS) is supplied through the chamber and the ORD-setup to the AMS. Thus, the condensation of TPP and TPPO formation are monitored in a period with only unreactive AS and with a mixture of AS and SOA containing peroxides.

3.2.1 Methods

ORD-AMS

Figure 14 shows a schematic diagram of the experimental setup for the AMS online measurements. The aerosol was first dried by two charcoal filled denuders (inner tube: diameter = 2 cm, length 40 cm, outer tube: diameter 13.5 cm, length 40 cm) and its number, surface, volume and mass concentration were measured using a scanning mobility particle sizer (SMPS, Grimm Aerosol Technik, Ainring, Germany).

In the case of the ORD-AMS mode (blue path in Figure 14), the dried particles were introduced into a 500 mL glass tube (35 cm length, max. diameter 4.5 cm), the condensation/reaction volume. Here, the aerosol was mixed with the gaseous reactant TPP (99%, Acros Organics BVBA, Geel, Belgium), which was supplied from a modified Sinclair-La Mer setup (see Figure 14, blue triangle). The TPP source consisted of a 100 mL two-necked round bottom glass filled with TPP and was heated to a temperature of 90 °C. Nitrogen was used as a carrier gas to deliver TPP to the condensation/reaction volume, where TPP condensed on the available particle surface. After passing the condensation/reaction volume, the aerosol was led through a third denuder filled with active charcoal to remove gas-phase TPP. Finally, the aerosol was introduced into the AMS and a condensation particle counter (CPC, PortaCountPlus, TSI In., Shoreview, MN, USA). A total flow rate of 1.74 L/min was obtained using an additional pump (sampling rate = 1000 mL/min). The residence time of the aerosol in the flow tube and the denuder was about 35 s.

In the case of the AMS mode (red path in Figure 14), the aerosol was directly supplied to the AMS and the CPC. The change between the two modes was achieved by a manual change of the connections (PTFE tubes). The data acquisitions of the AMS and the SMPS were disrupted in this time and continued after the stabilization of the particle number concentration, measured by the CPC (1-2 min).

The nitrogen stream enriched with TPP was added to the aerosol stream in the ORD-AMS mode resulted in a dilution of the aerosol. The correction for this dilution was done by comparing the particle number concentrations, measured in the ORD-AMS and AMS mode using the CPC. The ratio between the particle number concentrations of the two modes was used as a dilution factor.

ToF-AMS

The aerosol particles were introduced into the ToF-AMS (Aerodyne Research Inc., Billerica, MA, USA). The ToF-AMS was either operated in the mass spectrum (MS) or the Particle Time-of-Flight (PToF) mode using a time resolution of 2 min (3 x 20 s MS V-mode and 20 s PToF mode). The mass spectra acquisition was performed in the

positive ion mode (m/z range 12–546). The AMS data were processed using the Igor Version Pro 6.37 based programs “SQUIRREL 1.57 G” unit mass resolution and “PIKA 1.16H” high resolution according to the guidelines available (Field Data Analysis Guide; High Resolution ToF-AMS Analysis Guide).

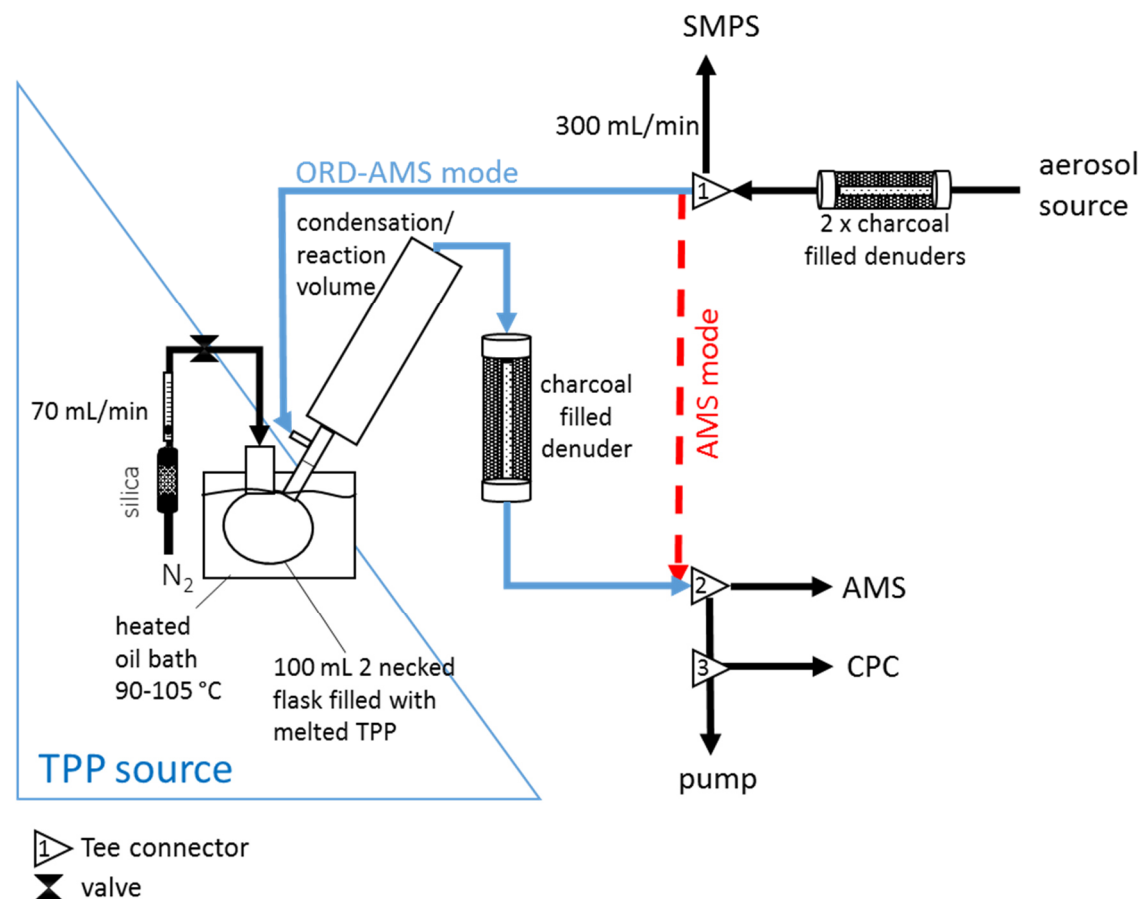


Figure 14: Schematic setup of ORD-AMS. The gas phase of the aerosol is removed, typically by two denuders containing charcoal. A Scanning Mobility Particle Sizer (SMPS) measures the particle number, surface, volume and mass concentration of the original particles. They are mixed with a nitrogen stream with a flow rate of 70 mL/min containing gaseous TPP. Not absorbed TPP is removed by charcoal filled in a denuder. The absorption of TPP and the reaction to TPPO is monitored by the AMS and a CPC. The TPP-source is based on a Sinclair-La Mer setup containing a two necked flask filled with melted TPP. The flask is heated to 90 °C. The red line indicates the setup when the original aerosol has been measured.

Additional Physical Aerosol Characterization

A Scanning Mobility Particle Sizer (SMPS, Grimm Aerosol Technik, Ainring, Germany, $Q = 300$ mL/min) was used to measure aerosol number size distributions of the incoming aerosol. It consists of a ^{241}Am source as neutralizer, a differential mobility analyzer (model L-DMA) and a condensation particle counter (CPC 5416). Besides the measurement of the aerosol size distribution, the instrument can be used to generate monodisperse aerosols for the calibration of the AMS (Slowik et al., 2004; DeCarlo et al., 2004). A CPC of PortaCountPlus (TSI In., Shoreview, MN, USA) was applied for further determination of the particle number concentration.

Nebulizer

The EI-spectra of the derivatization agent TPP and its reaction product with peroxides TPPO (> 98 %, Merck KGaA, Darmstadt, Germany) were recorded using the nebulizer setup (Figure 39 in the supplementary information, section 7.1.1). Pure TPP and TPPO particles were produced from solutions in methanol (Optima® LC/MS grade, Fisher Scientific, Loughborough, UK) and *n*-heptane (HPLC grade, Carl Roth GmbH + Co. KG, Karlsruhe, Germany), respectively. For the calibration of TPP and TPPO, the particles from the *n*-heptane solution were size-selected using the DMA.

Reaction Chamber as SOA Aerosol Generator

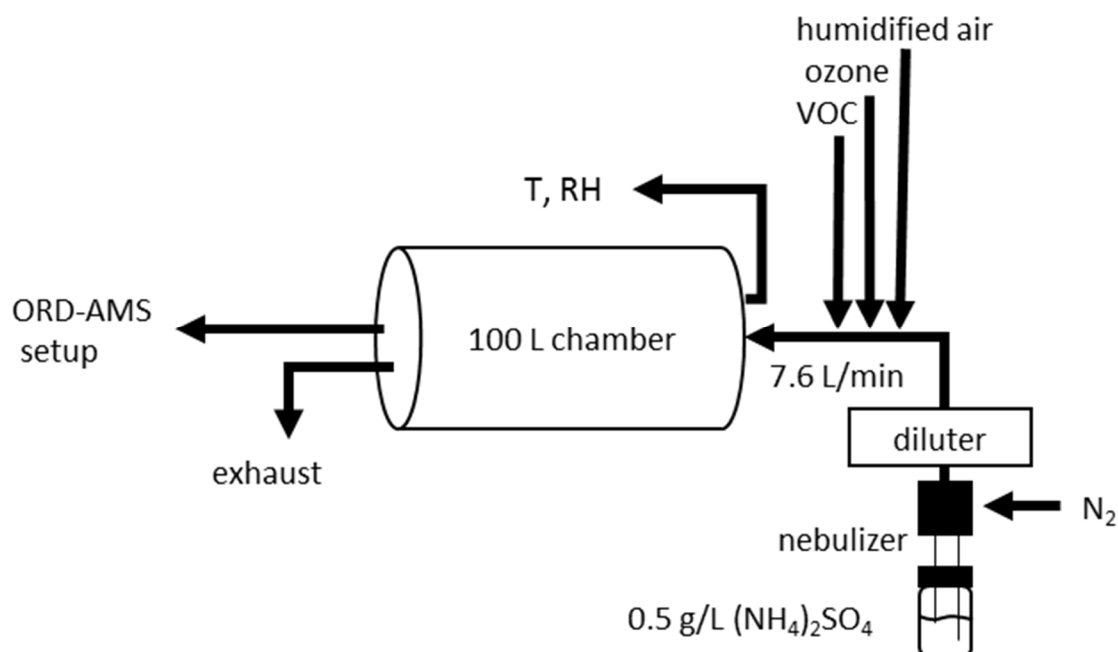


Figure 15: Setup of the SOA seed experiments. The seed aerosol is produced by the nebulization of ammonium sulfate (AS) solution and supplied to a 100 L continuous stirred-tank reactor. The AS concentration is set by a diluter. Wet air, dry air supplied through the ozone generator and dry air supplied through the terpene source was added generating a total chamber flow rate of 7.6 L/min. A thermo/hygrometer measures the chamber temperature T and the relative humidity RH . Ambient pressure was obtained by an additional exit for the exhaust. The chamber air was supplied at a sampling flow rate of 2.1 L/min to the ORD-AMS setup in Figure 14.

For the studies on SOA, a photochemical reaction chamber in CSTR mode (continuous stirred-tank reactor, Figure 15) was used. Synthetic air was produced by a generator (Jun-air/Gast Manufacturing, Inc. Benton Harbor, MI, USA). The air was supplied with a total flow rate of $Q = 5.9$ L/min through a diffusion source ($Q = 600$ mL/min), described by Thorenz et al. (2012), the ozone generator (Dasibi Environmental Corp. Model 1008 RS O3 analyzer, Glendale, CA, USA, $Q = 2700$ mL/min) and a gas washing bottle ($Q = 2600$ mL/min), filled with ultrapure water, to a 100 L glass chamber. The synthetic air was enriched with the terpenes in the diffusion source and with water in the gas washing bottle. Hereby, a GC vial filled with the respective terpene was put into the diffusion source, which consists of a tempered double-wall vessel at 30 °C. A capillary was put through the cap of the vial. An aqueous solution of ammonium sulfate (AS, ca. 0.5 g/L, > 99.5%, Merck KGaA, Darmstadt, Germany) was nebulized using technical nitrogen and the resultant seed aerosol was introduced into the

chamber ($Q = 1700$ mL/min). Temperature and relative humidity were 25 °C and 61% at the α -pinene ozonolysis and 22 °C and 59% at the β -pinene ozonolysis. They were monitored by a thermo/hygrometer (Amarell, ama-digit ad 910 h, Kreuzwertheim, Germany). The chamber was set under overpressure. The wall was covered with aluminum foil to avoid OH radical formation.

For the ozonolysis of α -pinene (> 99%, Fluka, Seelze, Germany), the chamber had been first enriched with the terpene before the ozone generator was switched on. Ozone was added before the terpene for the ozonolysis of β -pinene (99%, Sigma Aldrich Chemie GmbH, Steinheim, Germany). The ozone concentration was roughly estimated to 1 ppm, the α -pinene concentration to 290 ppbv and the β -pinene to 380 ppbv. The formed secondary organic aerosol was supplied to the ORD-AMS setup in Figure 14.

3.2.2 Results and discussions

Identification of TPPO and TPP.

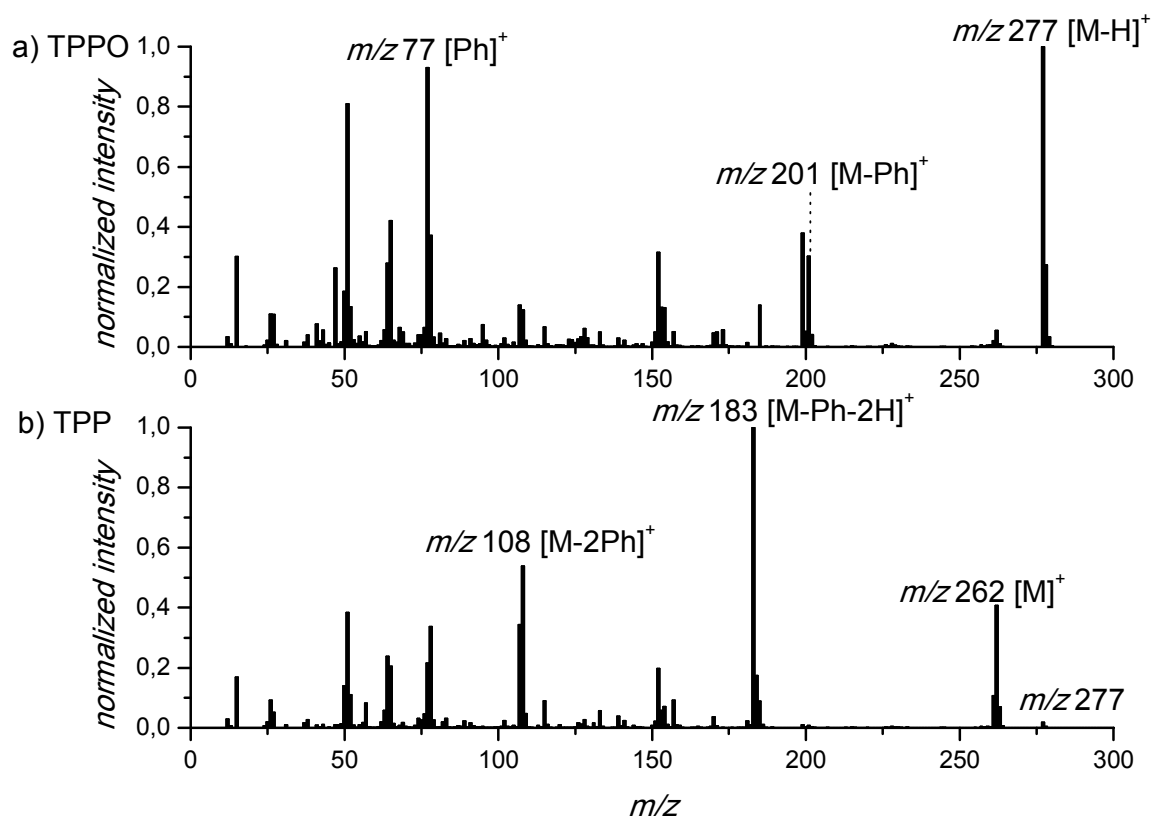


Figure 16: Mass spectra of a) triphenylphosphine oxide (TPPO) and b) triphenylphosphine (TPP).

Figure 16 shows the obtained mass spectra of TPPO and TPP. The EI spectra of the two reference compounds measured by the AMS are comparable to the spectra measured before (Koch et al., 1977:626; Williams et al., 1968). The base peak for TPPO is at $m/z 277$ originating of a hydrogen abstraction [M-1]⁺ from the molecular ion (M⁺, $m/z 278$). The second-largest peak is $m/z 77$ formed from the abstraction of a phenyl (Ph) cation. The base peak for TPP is at $m/z 183$ originating from the abstraction of two hydrogens and a phenyl group, probably a result of a weak aromatic stabilization of the resulting dibenzophosphole cation (Williams et al., 1968). However, also the

molecular ion of TPP at m/z 262 is visible. More important is the small but still observable $[M-1]^+$ ion of TPPO in the TPP spectra.

Quantification

The molar concentration c_n of TPP and TPPO were calculated from the signal at m/z 262 and m/z 277 using Eq. 35 and Eq. 36.

$$c_n(\text{detected TPP}) = \frac{10^{12}}{\frac{IE}{AB}(TPPO, \frac{m}{z} 262) \cdot AB \cdot Q \cdot N_A} \cdot I\left(\frac{m}{z} 262\right) \quad \text{Eq. 35}$$

$$c_n(\text{detected TPPO}) = \frac{10^{12}}{\frac{IE}{AB}(TPPO, \frac{m}{z} 277) \cdot AB \cdot Q \cdot N_A} \cdot I\left(\frac{m}{z} 277\right) \quad \text{Eq. 36}$$

IE are the ionization efficiency of the compound, AB the airbeam, defined as the signal at m/z 28, reflecting the detection efficiency, Q the flowrate of the AMS, N_A Avogadro's number and 10^{12} a conversion factor to $\mu\text{mol}/\text{m}^3$. Since other ions at nominal mass 277 are not expected to be measured, the signal at the unit mass of 277 (unit mass resolution) can be used instead of the signal at the exact mass of the $[M-1]^+$ ion of TPPO (high mass resolution) at the data processing.

The ion yield (IE) at m/z 277 was normalized to the airbeam in the calibration, yielding IE/AB (TPPO, m/z 277) = $2.61 \cdot 10^{-13} \text{ Hz}^{-1}$. The concentration of TPP was determined using the ion rate at a unit mass of 262 and the corresponding normalized ion yield IE/AB (TPP, m/z 262) = $2.01 \cdot 10^{-13} \text{ Hz}^{-1}$. The experimental procedure to estimate IE/AB is discussed in more detail in the supplementary information (section 7.1.2-7.1.3). It is based on the guidelines available online (Field ToF-AMS Operation).

Background Correction

As mentioned above, also pure TPP aerosol particles show a small but non-negligible TPPO signal. This is likely due to traces of peroxides in the solvents used to generate the aerosol particles when the nebulizer was used (Kleindienst et al., 1988; Banerjee and Budke, 1964) and TPPO impurities in the TPP itself (Mochida and Nakamura, 2006). Consequently, a background (backgr.) correction procedure had to be introduced to account for this effect. To do so, pure ammonium sulfate (AS) aerosol particles were investigated with different initial AS concentrations with the ORD-ToF-AMS setup. These experiments showed an average background contribution of 1.22 (+/-0.10)% TPPO from the conversion of TPP (Table 6 in the supplement, section 7.1.4). Therefore, the molar concentration of peroxides $c_n(\text{ROOR}')$ was calculated as follows:

$$c_n(\text{backgr. TPPO}) = 0.0122 \cdot c_n(\text{detected TPP}) \quad \text{Eq. 37}$$

$$c_n(\text{produced TPPO}) = c_n(\text{detected TPPO}) - c_n(\text{backgr. TPPO}) \quad \text{Eq. 38}$$

$$c_n(\text{ROOR}') = c_n(\text{produced TPPO}) \quad \text{Eq. 39}$$

Ozonolysis of α -pinene

Peroxide concentration. The ozonolysis of α -pinene was performed in the presence of AS seed particles and the results of a typical chamber run are shown in Figure 17. After the particle concentration became constant, the α -pinene was introduced into the chamber. In the run shown in Figure 17, for example, this was the case after 34 min. Following an initial period to monitor background peroxide concentrations in the AS seed aerosol/ α -pinene system, ozone was introduced, e.g. after 135 min in the α -pinene run shown in Figure 17. Periods without the addition of TPP are marked in grey in Figure 17 and were used to determine the dilution factor and the concentration of SOA using the AMS.

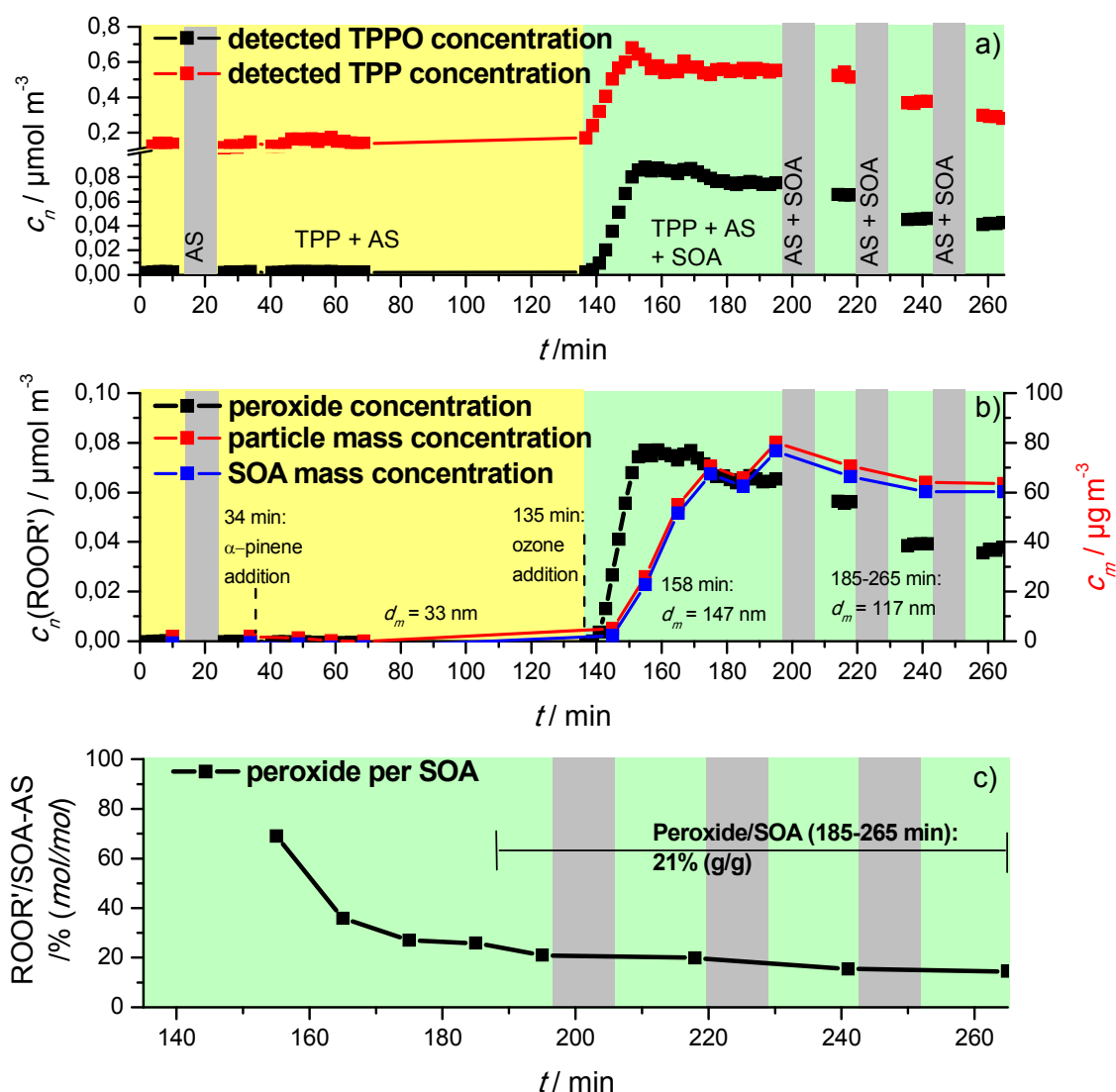


Figure 17: Time series a) of detected TPPO (black) and detected TPP (red), b) of peroxide concentration (black) after background correction and mass concentration of the aerosol and SOA (red), and c) of peroxide per SOA (black). Periods without the addition of TPP are marked with a grey background, periods before the addition of ozone are marked in yellow and during the ozonolysis in green. α -pinene was continuously added after 34 min and ozone after 135 min. Peroxide mass per SOA mass ratio was determined for the last 80 min (185-265 min) of the ozonolysis, assuming average molar masses of 250 g/mol for SOA.

The yellow and green backgrounds mark the periods before and during the ozonolysis, respectively. As can be seen in Figure 17a), the detected concentrations of

both TPPO and TPP were quickly rising during the first 20-25 min after the ozone generator was started, followed by a slow decrease towards the end of the experimental run. Peroxides were only detected when SOA was formed, indicated by the time series of the SOA concentration in Figure 17b). The SOA concentration was not directly measured but it was calculated from the total aerosol concentration, measured using the SMPS, and the AS concentration, measured using the AMS (more details see section 7.1.5).

The ratio of peroxide to SOA (Figure 17c) shows a continuous decrease towards the later stage of the experiment. Several studies suggest that organic peroxides are first-generation oxidation products and decompose rapidly, promoting SOA aging (Li et al., 2016a; Riva et al., 2017; Krapf et al., 2016; Zhao et al., 2018; Mertes et al., 2012). The SOA concentration was about $69 \mu\text{g}/\text{m}^3$ during the last 80 min (185-265 min in Figure 17b). Docherty et al. (2005) proposed an average molar mass of 300 g/mol for SOA peroxides, resulting in a percentage of peroxide mass to SOA mass of 47%. In our study, 21 (+/- 5) % peroxide to SOA was obtained, matching rather with the value of 22% of Epstein et al. (2014) and 21% of Li et al. (2016a). Mertes et al. (2012) observed 34%, 17% and 12% for 15-35 min, 4 hours and 6 hours filter samples, respectively. Therefore, the difference in the peroxide content could result from different sampling times, which is also supported by the decrease of the peroxide/SOA ratio.

Formation of pure SOA particles parallel to condensation of SOA on seed particles. The AS concentration was $0.01 \mu\text{mol}/\text{m}^3$ before the ozonolysis and $0.02 \mu\text{mol}/\text{m}^3$ during the last 80 min of the ozonolysis, the particle number concentration was 7100 and 14000 particles/ cm^3 , respectively. The SMPS size distribution of the particle number concentration (Figure 42 in the supplementary information, section 7.1.6) indicates the growth of the seed particles due to SOA condensation, but also particle new formation of pure SOA. Particle growth could change the particle loss rate in the chamber or during the transport from the chamber to the SMPS. According to Nah et al. (2016), Pierce et al. (2008) and Crump and Seinfeld (1981), the initial seed particles with a mean diameter of 33 nm will have a higher loss due to a higher diffusion than the particles with mean diameters of 147 nm at 158 min and 117 nm during the last 80 min (185-265 min in Figure 17). The surface area concentration was $59 \mu\text{m}^2/\text{cm}^3$ before the ozonolysis and $1400 \mu\text{m}^2/\text{cm}^3$ in the last 80 min. According to Huang et al. (2016), the latter value is already classified as a low seed surface area. Therefore, the nucleation rate might have decreased and the condensation rate on preexisting aerosol increased after the pure SOA and the mixed SOA-AS particles had grown. Finally, the change in the AS mass and particle number concentrations was a result of the particle new formation and a change in the particle loss rate due to particle growth.

Size distribution. One of the advantages of the AMS is the determination of the size distributions of single m/z ratios. If an m/z ratio is characteristic for an aerosol component, e.g. m/z 30 and m/z 46 for nitrate, the distribution of this component can be obtained. Figure 18 a)-d) shows the size distributions of m/z 277 (black), 262 (blue), 43 (green) and of sulfate (red) for the periods before (top) and during the last 80 min of the ozonolysis (bottom) with (right) and without (left) added TPP. The

distributions are normalized to their respective maxima. m/z 277 corresponds to the detected TPPO, m/z 262 to the detected TPP and m/z 43 to SOA species. Size distributions of TPP could only be obtained when TPP was added to the aerosol. As expected, neither m/z 277 (TPPO) nor characteristic SOA fragments showed characteristic size-dependent distributions before the ozonolysis. However, there is a clear overlap for m/z 277 and m/z 43 in Figure 18d), demonstrating the simultaneous presence of TPPO and SOA species in the particle phase.

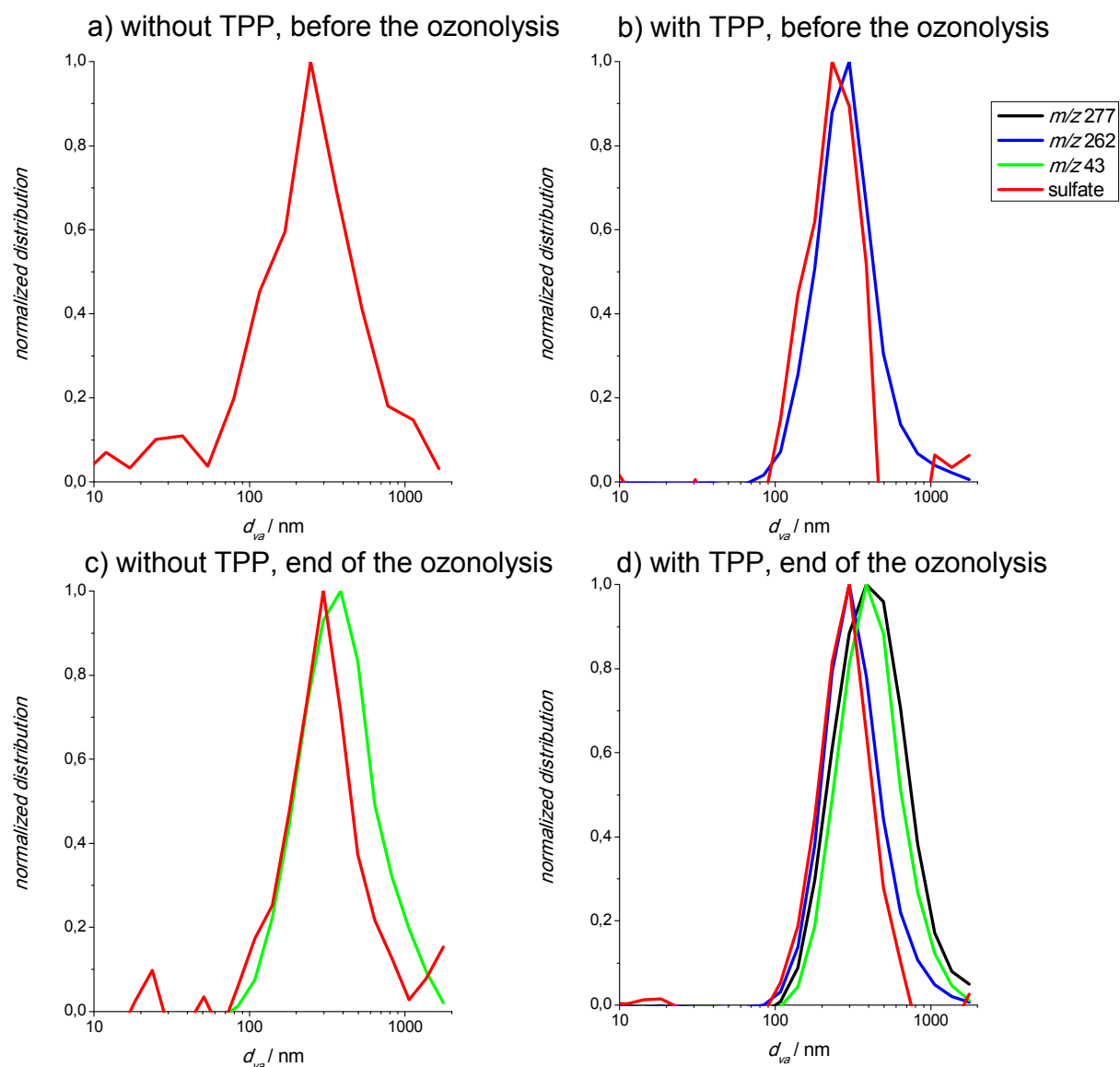


Figure 18: Size distributions of m/z 277 (black, TPPO), m/z 262 (blue, residual TPP), m/z 43 (green, SOA), sulfate (red) for following periods: before the start of the ozonolysis a) without and b) with adding TPP, at the end (185-265 min) of the ozonolysis c) without and d) with adding TPP. All distributions were normalized to their maximum.

As already mentioned, there was a formation of pure SOA particles simultaneously to the growth of the seed particles. During further ozonolysis, however, the size distribution became unimodal (Figure 43 in the supplementary information, section 7.1.6). According to AMS size distributions of the first 10, 20 and 30 min (Figure 44, 45 and 46), SOA and TPPO were found in smaller particles at the beginning of ozonolysis and in larger particles towards the end, compared to sulfate. There is

always an overlap of the distributions of SOA and TPPO like in Figure 18d), which supports evidence of the formation of TPPO due to peroxides in the particle phase.

The mean diameter of TPP is slightly larger than that of sulfate in Figure 18d). For the moment, it is still not clear whether the distribution of the residual TPP (= detected TPP) is a result of a higher conversion of TPP to TPPO in the larger particles or a size-dependent condensation of TPP. In future research, monodisperse aerosol without peroxide species should be measured using ORD-AMS for a better understanding of the condensation of TPP on the aerosol.

SOA formation of β -ozonolysis in the presence of AS seed aerosol

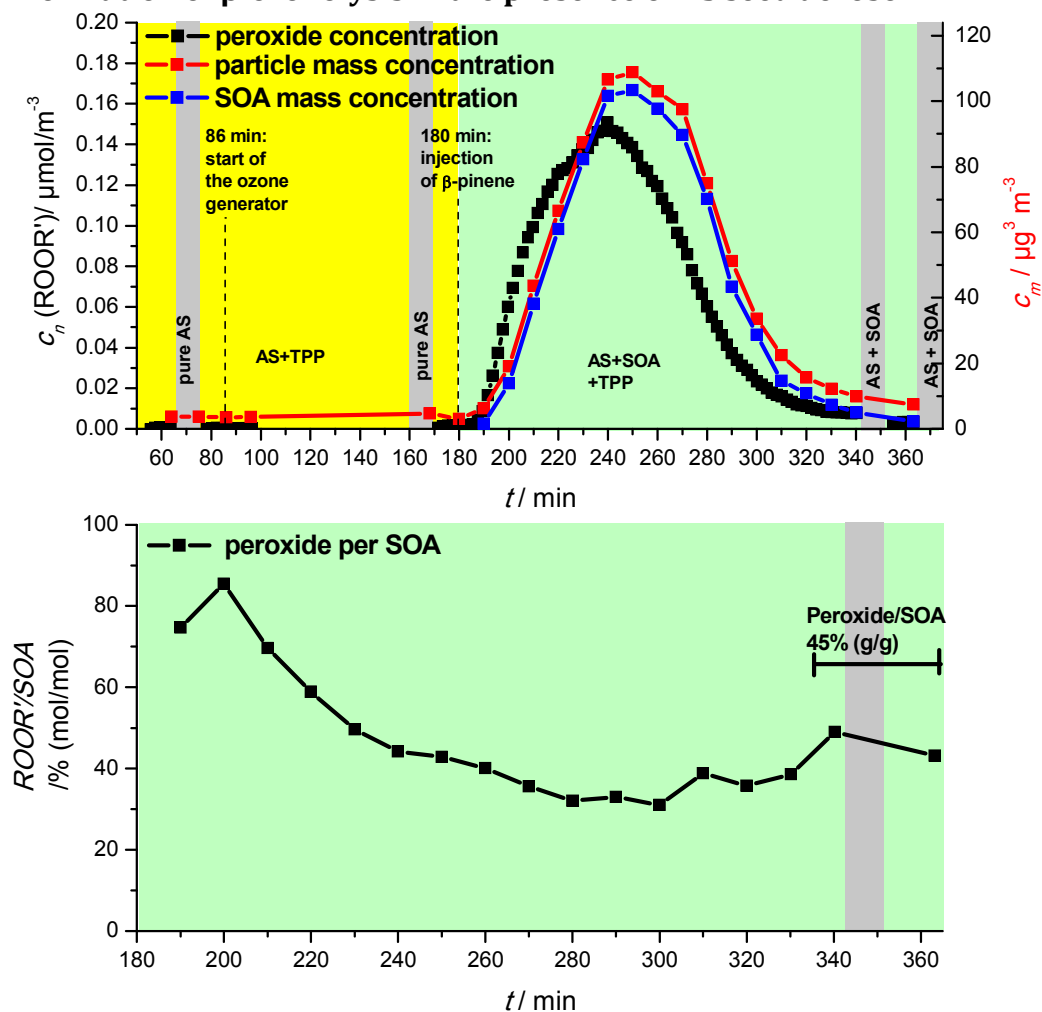


Figure 19: Ozonolysis of β -pinene in the presence of AS aerosol. Time series of a) the concentration of peroxide (black), particles (red), and SOA (blue) and b) peroxide/SOA. Ozone was added from 86 min, β -pinene from 180 min. To determine the peroxide/SOA ratio, mean molar masses of 250 g/mol were assumed for SOA.

To exclude ozone as an oxidant for TPP, the ozonolysis of β -pinene was performed in the presence of AS seed aerosol as well (run shown in Figure 19). Ozone was introduced into the chamber after 86 min and the terpene after 180 min. The peroxide concentration is illustrated together with the mass concentration of the chamber aerosol and SOA in Figure 19a). As in the case of α -pinene, the peroxide concentration increased rapidly after the injection of β -pinene with the formation of SOA, once again demonstrating the direct connection of SOA and peroxide formation via the detection

of TPPO. The comparison of the profiles of SOA (red) and peroxide (black) demonstrates the very rapid peroxide formation followed by the decreasing contribution of peroxide to the particle phase in the later stages of the experiment, which is a consequence of consecutive reactions of the peroxides to non-peroxidic products. The strong decrease of total SOA after 240 min is induced by the end of β -pinene addition to the reaction system.

Discussion about selectivity and quantification.

The experiment with β -pinene showed that there was no reaction of TPP with ozone. Aerosols of nebulized solutions of TPP in *n*-heptane and methanol had background contributions of TPPO to TPP ratios of 5% and 16%, respectively, using technical nitrogen as the carrier gas for the aerosol. Mochida and Nakamura (2006) determined oxygen in the air as the oxidant, which reacted faster with TPP when it was dissolved. A part of TPP might have been oxidized already before it was dissolved in methanol and *n*-heptane and was further oxidized in solution. The generation of peroxides in solvents is well known (Kleindienst et al., 1988; Banerjee and Budke, 1964). This could explain the higher background level than in the SOA seed experiment, where background contribution was 1.2% at an oxygen content of 14% in the carrier gas.

However, molecular oxygen was in large excess to TPP at the SOA experiments. Generally, the reaction velocity can depend on the respective concentrations of the reaction partners. If one of them is in large excess, the reaction will become independent of it (IUPAC, 2014; Atkins and de Paula, 2006; order of reaction, *n*; Tinoco et al., 1995). Therefore, the reaction between TPP and oxygen depends only on the TPP concentration and not on the oxygen concentration, since the latter is quasi constant. This would explain the dependence of background TPPO on detected TPP.

Finally, the overlap of the SOA and TPPO size distribution in Figure 18d) and Figure 44, 45 and 46 in the supplementary information (section 7.1.6) showed strong evidence that TPPO is formed by the reaction of TPP with peroxides in the particle phase. In contrast, no size distribution of TPPO was obtained before the ozonolysis had started (Figure 18b). Furthermore, the TPP method is often used for the determination of peroxide with the same yield as the iodometric determination in aged oils and fats (Nakamura and Maeda, 1991; Mochida and Nakamura, 2006; Wang et al., 2016). Different oxygen-containing species can be expected in these samples as well (Lercker et al., 1998; Köckritz and Martin, 2008).

As no experiments of test aerosols with known concentration of commercially available peroxides was shown, there might be a question if the reaction of TPP with peroxides is quantitative. To answer this question, the ratio between the concentration of peroxides and SOA at the end of the ozonolysis of α -pinene was compared with the results of Epstein et al. (2014), Li et al. (2016) and Mertes et al. (2012). In the references, the peroxide concentration was measured during the ozonolysis of α -pinene using filter or impactor sampling, followed by the extraction and iodometric analysis of the peroxide content. Several parameters such as the terpene and ozone concentration, their ratio to each other, temperature and relative humidity and the use of an OH scavenger vary, and a seed aerosol was not used. The

chamber conditions at Li et al. 2016 matches best with the conditions in this study. However, all peroxide/SOA ratio are in a range of 17 to 47% and are in a good agreement with each other, which can be considered as a validation. Furthermore, Mertes et al. (2012) and Li et al. (2016) found a continuous decrease of the peroxide/SOA ratio, which was also observed in this study. Besides, according to the result of Koop et al. (2011), SOA is rather expected to be a liquid than a solid under the chamber conditions with temperatures of 22 to 25 °C and a relative humidity of 60%. The seed aerosol was also not dried by a silica filled denuder. The seed particles should be liquid as well since the dehydration of ammonium sulfate particles started at a relative humidity of 30% (Matthew et al., 2008). The diffusion time of TPP within the particles should be approximately a second (Koop et al., 2011), which is shorter than the residence time of 35 seconds of the aerosol in the ORD-setup (Figure 14). Furthermore, TPP was added at least twofold in excess to the SOA species (as seen in Figure 47 and Figure 48 in section 7.1.7). Following the results of R. A. Stein and V. Slawson (1963), a reaction of TPP with peroxides is expected for all types of peroxides except tertiary peroxides.

In the end, regarding the agreement of the peroxide/SOA ratio, the diffusion time and the excess of TPP to SOA, a quantitative reaction of TPP with peroxide to TPP is assumed. However, in future investigations, the method should be revalidated using commercially available test peroxides as pure aerosol particles, in mixtures with other compounds and using particles with different viscosities.

3.3 Peroxide analysis of SOA without seed aerosols

In this section, the new ORD-AMS method was tested with peroxides in SOA from the ozonolysis of monoterpenes. In contrast to section 3.2, the experiments were performed without seed particles.

3.3.1 Method

Chemicals

TPP (99%), (-)- α -pinene ($\geq 99\%$), (-)- β -pinene and R-(+)-limonene (97%) were purchased from Acros Organics BVBA (Geel, Belgium), Fluka (Seelze, Germany), Sigma Aldrich Chemie GmbH (Steinheim, Germany), and Merck KGaA (Darmstadt, Germany), respectively.

Setup for the peroxide determination

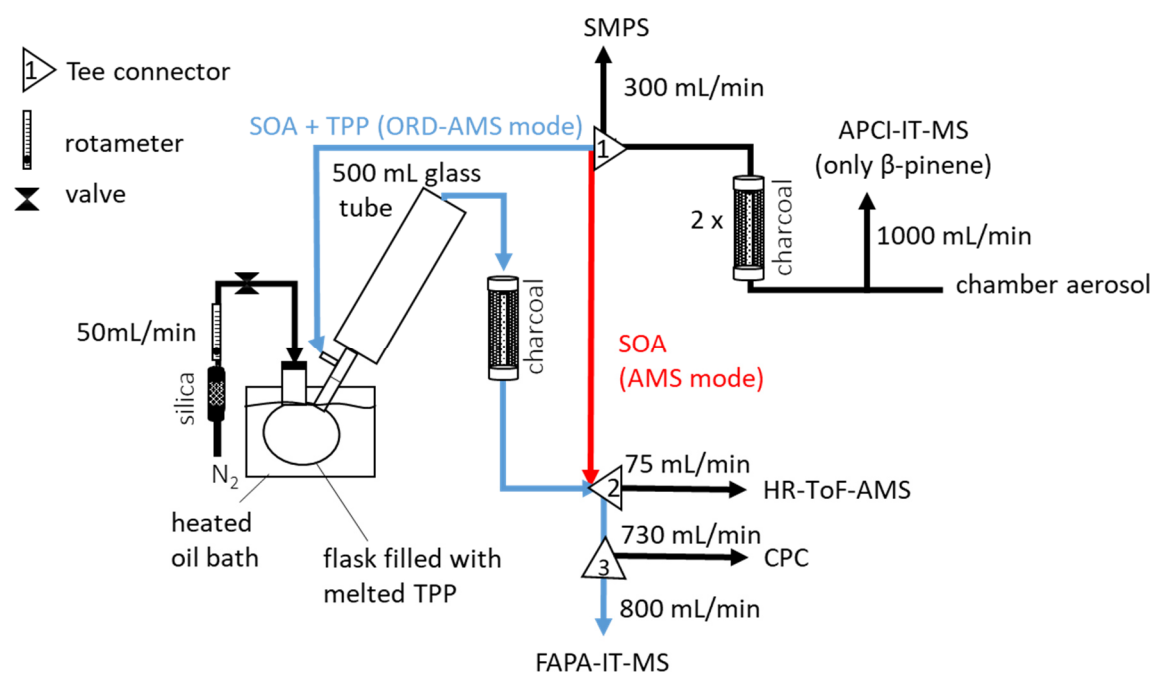


Figure 20: Schematic setup of peroxide analysis.

The setup for the peroxide analysis is given in Figure 20. The chamber aerosol was first introduced through two denuders (inner tube: diameter = 2 cm, length 40 cm, outer tube: diameter 13.5 cm, length 40 cm) with charcoal to reduce the gaseous species. In the ORD-AMS mode (blue path), the aerosol was combined with a nitrogen stream enriched with gaseous TPP in a T-piece, further connected to the TPP source and a 500 mL glass tube (35 cm length, max. diameter 4.5 cm). The gaseous TPP was produced by heating TPP to its melting point in a two-neck flask. Nitrogen was supplied from a cannula through a septum into the flask, where it was enriched with TPP. The flow rate of 50 mL/min of the nitrogen stream was controlled by a rotameter and a valve. The mixture of TPP and the aerosol was introduced into the glass tube and to a third charcoal denuder. The condensation of TPP on the particle and the formation of TPPO were mainly monitored using a high-resolution time-of-flight aerosol mass spectrometer (HR-ToF-AMS, Aerodyne Research, Inc., Billerica, MA, USA). A scanning mobility particle sizer (SMPS, Grimm Aerosol Technik, Ainring,

Online redox derivatization for peroxide analysis

Germany) was used to detect the concentration of the particle number c_P , surface c_S , volume c_V and mass c_m of the original aerosol. The original aerosol composition was also measured when the aerosol source was directly connected to the mass spectrometers (AMS mode, red path). A condensed particle counter (CPC, Portacount plus, TSI Corp., USA) was used to determine the dilution factor, which results from the additional nitrogen stream and possible wall loss. A lab-built Flowing Atmospheric-Pressure Afterglow (FAPA) ionization source (Brüggemann (2015)) coupled to an LCQ Deca XP Plus ion trap (IT-MS, Thermo, San José, CA, USA) was used for qualitative information about peroxides in the SOA experiments and to monitor the time series of the terpenes. PTFE tubing was used as connectors between individual components of the setup. An APCI-IT-MS (LCQ-IT, Finnigan, MAT, USA) was added to the setup in front of the first two charcoal filled denuders in the case of the β -pinene ozonolysis. The sampling flow rates of the instruments are given in Figure 20.

The change between the ORD-AMS and AMS mode was achieved by a manual change of the connections (PTFE tubes). The data acquisitions of the AMS and the SMPS were disrupted in this time and continued after the stabilization of the particle number concentration, measured by the CPC (1-2 min).

SOA experiments

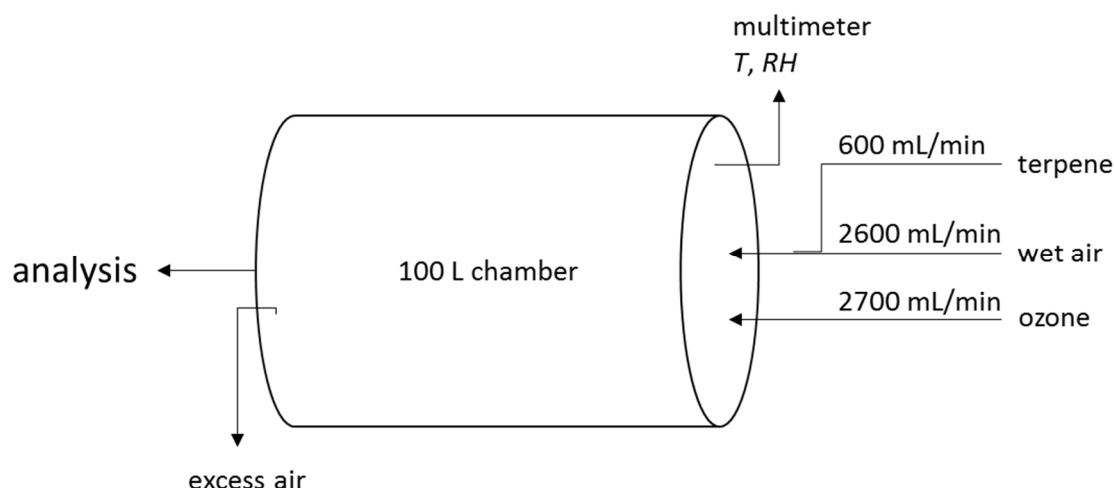


Figure 21: Schematic setup for the SOA generation.

The setup of the aerosol source is shown in Figure 21. A 100 mL glass chamber, darkened by aluminum foil, was cleaned by supplying pure synthetic air for one night. It was generally set under overpressure. A thermo/hygrometer (Amarell, ama-digit ad 910 h, Kreuzwertheim, Germany) measured the temperature and the relative humidity inside the chamber. The inlet was connected to a terpene source (Thorenz et al., 2012), an ozone generator (Dasibi Environmental Corp. Model 1008 RS O₃ analyzer, Glendale, CA, USA) and a gas wash bottle, where the air was supplied through ultra-pure water to increase the relative humidity. The ozone concentration without reaction with the terpene in the chamber was 1 ppm. The terpene source contains a diffusion source where the air was introduced through a heated coil into the double-wall container. A GC vial filled with the respective terpene was placed inside the double-wall container. A thermostat regulated the temperature to about

30 °C in the container and thus the diffusion of terpenes through a capillary in the cap of the vial. The initial terpene concentration was determined by weighing the vial before and after the experiment. The synthetic air with a relative humidity of about 30% was produced by a generator (Jun-Air / Gast Manufacturing, Inc. Benton Harbor, MI, USA) and was precleaned by a carbon trap (Big Hydrocarbon Trap - BHT-4, Agilent, Santa Clara, CA, USA).

General procedure. Experiments started by measuring the chamber background without the addition of the terpene and ozone. The respective terpene was added into the chamber and the ozone generator was switched on after at least 60 min of enrichment when the terpene concentration became constant. The oil bath with the TPP flask was heated to 90 °C. After the nucleation burst, the temperature was increased to 100-110 °C. When the particle mass concentration at the SMPS became constant, the aerosol was measured alternating in the ORD-AMS (blue path in Figure 20) and the AMS mode (red path in Figure 20). Before the achievement of the constant mass concentration, only the ORD-AMS mode was used. A deviation from the general procedure was done for the ozonolysis of limonene, where an initial oil bath temperature of 105 °C led to an overload of TPP during the nucleation. The measurement was interrupted for 40 min to protect the mass spectrometers from overloading.

Instruments

HR-ToF-AMS and quantitative determination of peroxides. In the following experiments, 3 x 20 s MS V-mode and 20 s PToF mode were applied, resulting in a time resolution of 2 min. The mass spectra acquisition was performed in the positive ion mode (m/z range 12–546). The raw data was processed by the Igor Pro (Version 6.37) based programs SQUIRREL 1.57G and PIKA 1.16H according to the guidelines available online (Field Data Analysis Guide; High Resolution ToF-AMS Analysis Guide).

The peroxide concentration was calculated as described in section 3.2.2.

SMPS. The size distributions of the particle number, surface, volume and mass concentration were obtained by calculation of the instrument software Grimm Universal. The SMPS contains a differential mobility analyzer (model L-DMA) with a ^{241}Am source as a neutralizer and a condensational particle counter (CPC 5416) with 1-butanol as working material (>99.5%, Carl Roth GmbH Co. KG, Karlsruhe, Germany). The time resolution of the SMPS was 200 s with a size range of 12.33 to 808.48 nm for SOA of α - and β -pinene. 300 s with a size range between 12.33 – 1094.31 nm was applied for SOA of limonene. A median effective density of 1.2 g/mL (Zelenyuk et al., 2008) was used to calculate the particle mass concentration. The data of the ozonolysis of α -pinene were transformed into the AMS time resolution, as shown in Figure 49 in the supplementary information (section 7.2).

CPC. The CPC measured the particle number concentration without automatic data acquisition. The values were noticed manually. It uses isopropanol (UV-IR-grade, Carl Roth GmbH Co. KG, Karlsruhe, Germany) as working material.

FAPA-IT-MS and APCI-IT-MS. The time resolution of the FAPA-IT-MS and APCI-IT-MS were set to 2 s per data point. The raw data was processed by XCALIBUR (Thermo, San José, CA, USA). The data of the ozonolysis of α -pinene were transformed to the AMS time resolution, as shown in Figure 51 in the supplementary information (section 7.2).

3.3.2 Results

Table 1 lists the final ratios of peroxide mass to SOA mass, called peroxide/SOA yield $Y_{PO/SOA}$, the chamber temperature T and relative humidity RH , the initial monoterpene concentration and the theoretical ozone concentration without reaction with the monoterpene. The results from previous studies from Docherty et al. (2005), Mertes et al. (2012), Li et al. (2016a), Gong et al. (2018) and section 3.2 are also shown for comparison. In all cases, an average molar mass of 300 g/mol, proposed by Docherty et al. (2005) for SOA peroxides, was assumed for the calculation of $Y_{PO/SOA}$. Since Docherty et al. (2005) used 1.0 g/cm³ and Mertes et al. (2012) 1.3 g/cm³ as particle density, their original results were converted for 1.2 g/cm³ as density, as applied in this study.

Table 1: Yield of peroxide mass per SOA mass during the last 60 min of the experiments, the chamber temperature and relative humidity, the initial terpene concentration, the ozone concentration without reaction with the terpene and the reference. *ppb or ppm. **transformed values including particle densities of 1.2 g/cm³. A density of 1 g/cm³ was used at Docherty et al. (2005) and 1.3 g/cm³ at Mertes et al. (2012). ***OH-scavenger added. ****in the presence of seed aerosol

Terpene	$Y_{PO/SOA}$ / %	T / °C	RH / %	terpene / ppmv	ozone / ppmv	reference
α -pinene	33 (+/-8)	23	53	0.058	1	this study
	20	25	60	0.290	1	section 3.2****
	25	25	60	0.275	42	(Li et al., 2016a)
	32-16**	20	50	0.090*	0.5*	(Mertes et al., 2012) ***
	41**	25	50	4.5	2.7	(Docherty et al., 2005) ***
β -pinene	67 (+/- 11)	25	55	1.046	1	this study
	45	23	60	0.380	1	section 3.2****
	69**	20	50	4.5	2.7	(Docherty et al., 2005)
limonene	48 (+/- 3)	24	55	0.071	1	this study
	47	25	50	0.183	19	(Gong et al., 2018)

In principal, all obtained $Y_{PO/SOA}$ are in the double-digit range of 16 to 70% demonstrating the importance of peroxides in SOA formation. The respective yields for α -pinene, β -pinene and limonene are in the same range as the yields found in the literature (Docherty et al., 2005; Mertes et al., 2012; Li et al., 2016a; Gong et al., 2018). As found by Docherty et al. (2005), $Y_{PO/SOA}$ is much higher for β -pinene than for α -pinene. The yield of 48% for the limonene ozonolysis is in between the yield of α -pinene and β -pinene. Mertes et al. (2012) observed a time-dependent yield of 32%

after the first 15-35 min, 16% after 4 h and 11% after 6 h for the ozonolysis of α -pinene. The ozone generation was stopped after 95 min in Mertes et al. (2012). This is a hint that peroxides are first-generation products of the ozonolysis. They react in consecutive reactions in the particle phase leading to chemical aging of the particles. The production of ozone and first-generation products was continuously running in this study. That might be the reason of the higher yield of 33% after approximately 2 hours of the α -pinene ozonolysis in this study while 16% after 4 hours was obtained by Mertes et al. (2012). Seed particles were introduced into the chamber during SOA formation in the experiments in section 3.2. The yield of 20% in the SOA-seed experiments match rather with the yield of 25% obtained by Li et al. (2016a). However, it is difficult to explain the higher yield in the seed-free experiments since temperature, relative humidity and the ratio between the concentration of ozone and terpene were different. A systematic variation of these parameter should be part of further studies.

SOA peroxide concentrations as a function of experiment duration

Figure 22 shows the time series of the measured peroxide and SOA mass concentration for the α -pinene ozonolysis. The resulting yield of peroxide to SOA ($Y_{PO/SOA}$, red curves in Figure 22) increased during the first 15 min to 95% and decreased afterward to approximately 30%. The ozonolysis of β -pinene (Figure 23) followed a similar trend, but the maxima were reached later: the maximum of peroxide concentration of $78 \mu\text{g}/\text{m}^3$ after 50 min, of the SOA mass concentration of $100 \mu\text{g}/\text{m}^3$ after 70 min and of the peroxide/SOA yield of 94% after 40 min. The yield decreased again to a value of approximately 65% after 160 min.

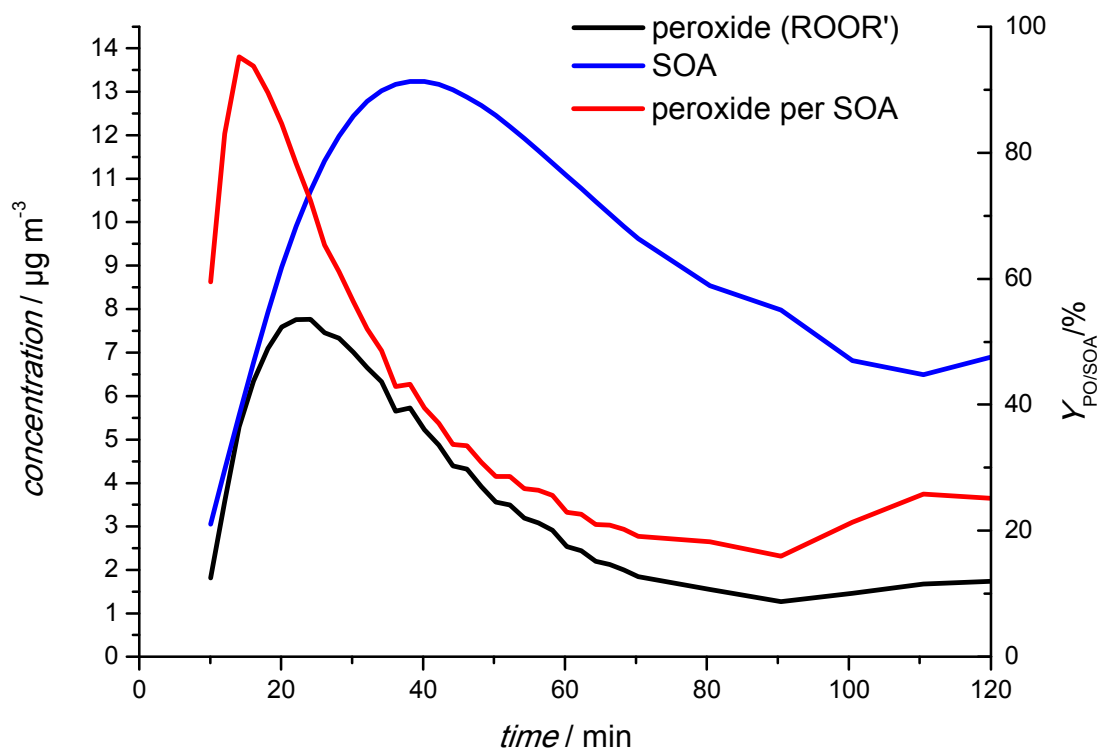


Figure 22: Ozonolysis of α -pinene. Time series of peroxide (black), SOA mass concentration (blue) and the peroxide / SOA yield (red).

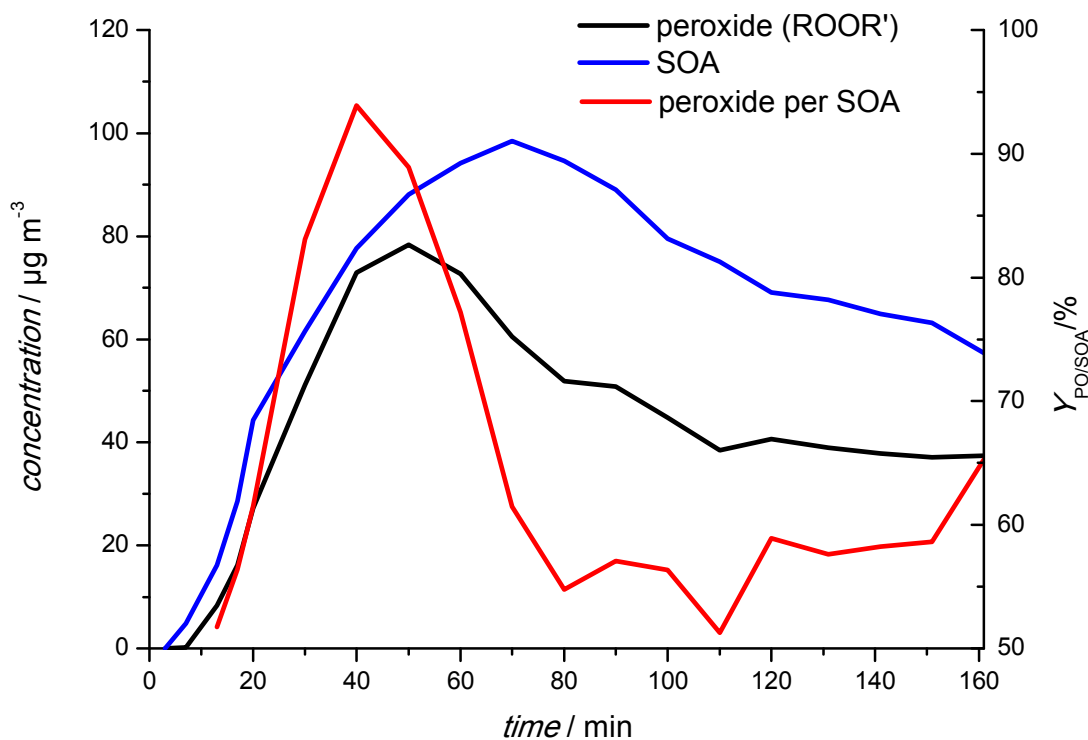


Figure 23: Ozonolysis of β -pinene. Time series of peroxide (black) and SOA mass concentration (blue) and the peroxide / SOA yield (red).

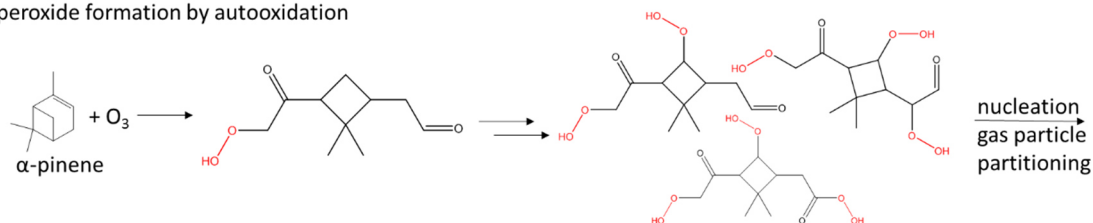
Discussion of the peroxide fate during the ozonolysis of α -pinene

Several studies suggest that peroxides are key compounds in the particle new formation (Zhang et al., 2017; Li et al., 2016a; Krapf et al., 2016; Ehn et al., 2012). The formation of peroxides in the gas phase and their gas-particle partitioning are the main sources or uptake of peroxides in the suspended phase. Formation of peroxide groups due to secondary autoxidation reaction in the particle phase might happen, but reactions inside of the particle or on the particle surface are expected to be rather a sink of peroxide groups (Epstein et al., 2014; Claflin et al., 2018). Accordingly, a continuous decrease of the peroxide / SOA yield would have been expected, as observed by Li et al. (2016a) and Mertes et al. (2012). However, a maximum is observed at the beginning of the ozonolysis (Figure 22 and Figure 23), indicating that the rate of the peroxide uptake was increased compared to the rate of peroxide loss.

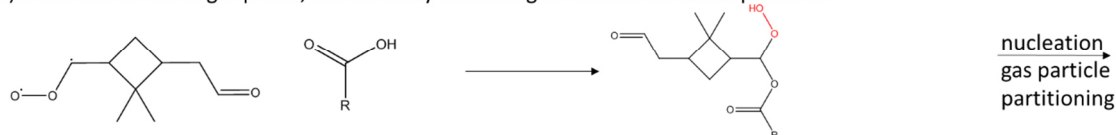
In principle, there are different ways for peroxides to occur in the particle phase (Figure 24). In all cases, the peroxides are produced from the reaction of ozone and the monoterpene in the gas phase. Peroxides with low volatility quickly undergo partitioning into the particle phase. HOMs are expected to be first-generation products of the ozonolysis and to contain several peroxide groups (Rissanen et al., 2014). They are formed by autoxidation (Figure 24a) and their contribution to particle new formation is expected because of their low volatility. In the gas phase, higher volatile peroxides react with carboxylic acids via the stabilized Criegee intermediate (Zhao et al. (2018), Claflin et al. (2018)) to low volatile dimers (chained molecules), which also contribute to the nucleation or the particle growth (Figure 24b). As dimerization requires the reaction of two molecules in the gas phase, an increasing concentration of dimers in the particle phase will occur with an increasing

concentration of oxidation products in the gas phase. Alternatively, hydroperoxides in the gas phase react with aldehydes at the particle surface, yielding low volatile peroxyhemiacetals, which remain in the particle phase (Figure 24c, Docherty et al., 2005) The formation of peroxyhemiacetals increases with increasing concentration of hydroperoxides in the gas phase and increasing surface.

(a) peroxide formation by autooxidation



(b) dimerization in the gas phase, facilitated by increasing amount of oxidation products



(c) gas-particle partitioning due to peroxyhemiacetal formation, facilitated by increasing surface area:

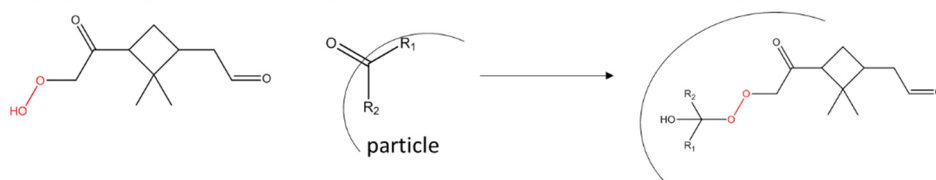
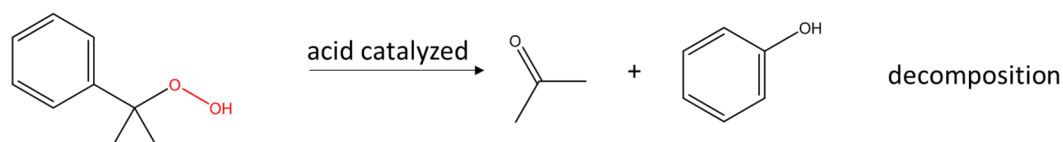
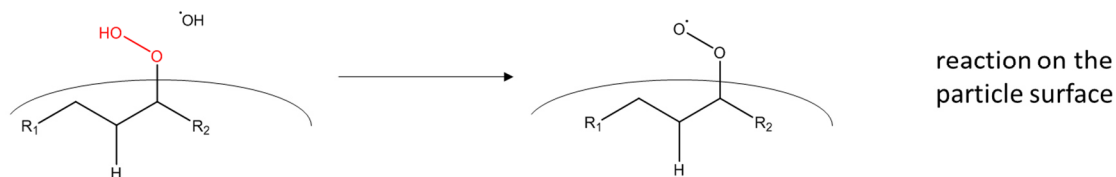


Figure 24: Peroxide formation a) by autooxidation, b) by dimer formation in the gas phase and c) peroxyhemiacetal formation on the particle surface. Peroxy groups are highlighted in red.

(a) dependent on the concentration and reactivity of the hydroperoxide group



(b) dependent on the particle surface area



(c) dependent on the number of molecules per particle

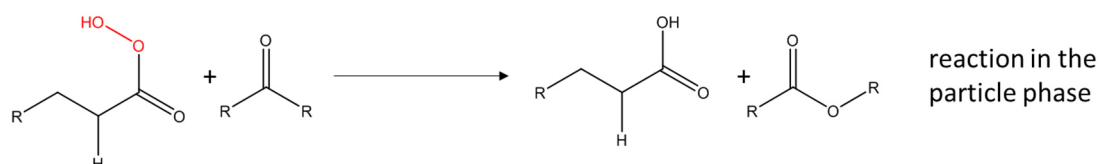


Figure 25: Peroxide sinks a) by thermal or acid-catalyzed decomposition, b) by reactions on the surface, such as the reaction with OH radicals and c) by the oxidation of other functional groups, such as ketones to esters. Peroxide groups are highlighted in red.

In general, three different reaction classes leading to the loss of peroxy groups in the particle phase can be distinguished. The first one is the thermal decomposition, depending only on the reactivity and concentration of the respective peroxide. A well-known example from bulk chemistry is the acid-catalyzed Hock phenol synthesis (Figure 25a, Yaremenko et al., 2016; Brinkhorst et al., 2008). The unimolecular decomposition is also well established in polymer science, where peroxides are sources for free radicals and initiation of polymerization (Krapf et al., 2016). The second class is the heterogeneous reaction on the particle surface, such as the reaction of peroxides with OH radicals proposed by Li et al. (2016a) and shown in Figure 25b). Khan et al. (2015) suggested that 95% of organic peroxides are lost by this reaction in the atmosphere. The third class is the reaction inside the particles (Figure 25c). According to Claflin et al. (2018), peroxides oxidize alcohols, aldehydes and ketones in the particle phase to aldehydes, carboxylic acids and esters. These reactions are also known in bulk chemistry (Yaremenko et al., 2016).

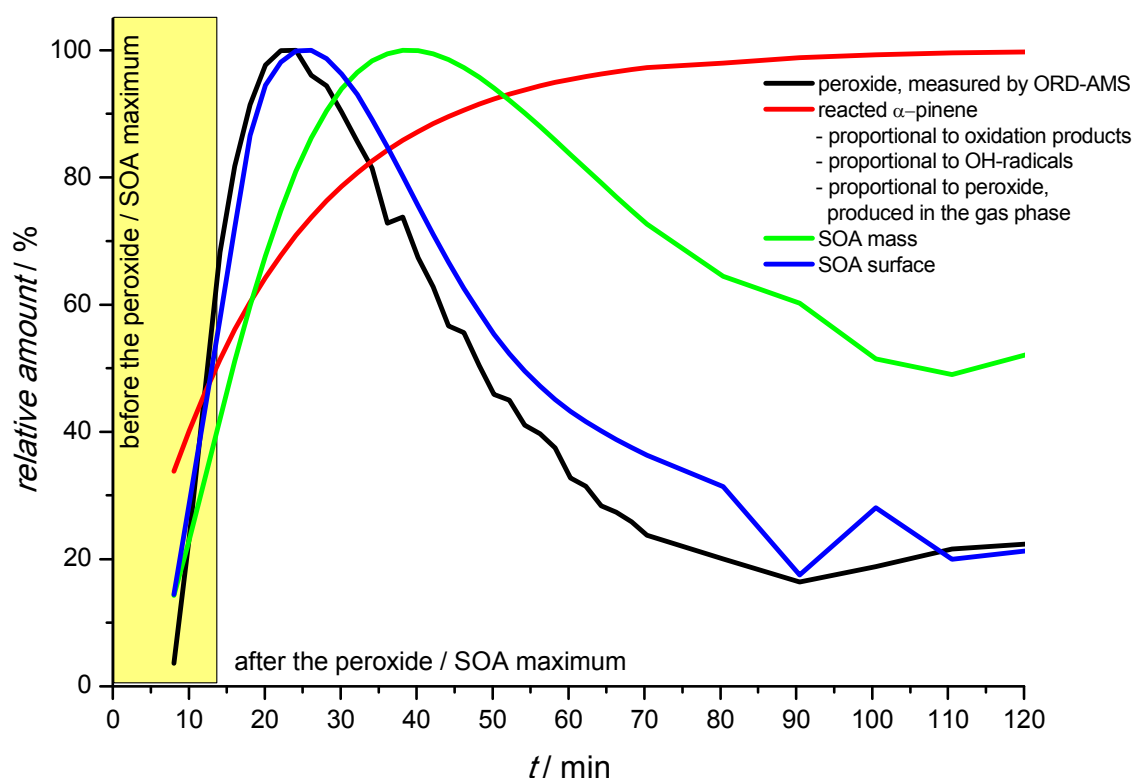


Figure 26: The time series of the relative amounts of peroxide (black), reacted α -pinene (red), SOA mass (cyan) and SOA surface. The amount of reacted α -pinene is proportional to the number of oxidation products including peroxides and OH-radicals. The period before the maximum of the peroxide/SOA ratio is highlighted in yellow.

Figure 26 shows the temporal evolution of the relative amount of the measured peroxides, reacted α -pinene, the SOA mass and SOA surface. Besides, the time series of reacted α -pinene is suggested to be proportional to the amount of products produced at the ozonolysis of α -pinene including also peroxides and OH-radicals. As can be seen, the surface and the number of oxidation products including peroxides increased in the beginning. These would favor the formation of dimers and peroxyhemiacetals. The uptake of peroxides in the particle phase increases therefore. Besides, the course of the peroxide is closed to the course of the surface until the

maximum of the peroxide amount. As the amount of OH-radicals is increasing parallel to the amount of the oxidation product, the rate of the reactions on the surface will increase as well. This might be the reason that the amount of peroxide decreased earlier than the SOA surface. Besides, the SOA mass increased, delayed to the measured peroxide concentration indicating an increasing rate of bulk reactions. Consequently, one cause of the increase in the ratio of peroxide to SOA in the first 14 minutes of ozonolysis is an increasing rate of formation and uptake of peroxide dimers and peroxyhemiacetals in relation to their chemical loss rates.

Another or additional explanation is a change in the contribution of different types of SOA peroxides to the chemical aerosol composition due to their different volatility and reactivity. HOM-peroxides are formed due to the autoxidation reaction and are first-generation products in the gas-phase (Figure 24a). They might have low volatility due to the high number of peroxy and other oxygen-containing groups. Therefore, they can contribute to the particle formation from the beginning of the ozonolysis. Dimers and peroxyhemiacetals are formed by consecutive reactions of peroxide monomers with other molecules. Due to the linking of the carbon chain, their volatility is very low even without a high number of peroxy groups. Thus, they contribute strongly to the particle formation and growth, but later than HOM-peroxides as they are formed in consecutive reactions. However, the reactivity of peroxidic compounds regarding thermal decomposition (Figure 25a), increases with the increasing number of peroxy groups. HOMs with a high number of peroxy groups should be more reactive than dimers and peroxyhemiacetals with a lower number of peroxy groups.

In conclusion, at the very beginning of the ozonolysis, compounds with a high number of peroxide groups such as HOMs might contribute to the particle new formation more strongly than dimers and peroxyhemiacetals. When the number of oxidation products and the particle surface increases, the contribution of the dimers and peroxyhemiacetals to the particle formation and growth increases compared to the contribution of highly reactive HOM-peroxides. Therefore, the chemical loss rate of peroxide groups should decrease compared to the uptake rate of peroxide groups, which could explain the increase of the ratio of peroxide to SOA in the first 14 min of the ozonolysis (Figure 22).

Finally, the increase of the ratio of peroxide to SOA in the beginning of the ozonolysis can be explained by increasing amount of dimers and peroxyhemiacetals due the increasing amount of gas phase products and increasing particle surface. Alternatively or in addition, the particle composition with highly reactive HOM peroxides at the beginning of ozonolysis could change to less reactive dimers and peroxyhemiacetals in the further course of ozonolysis. The decrease of the ratio of peroxide to SOA is explained by increased possibilities to react on the particles surface and in the bulk. These interpretations still support the hypothesis that peroxides are key species for the particle new formation and chemical aging of SOA.

3.4 Ambient air measurements

3.4.1 Method

The ORD-AMS method was tested with ambient air directly outside the chemistry building located at the campus of the Johannes Gutenberg University of Mainz (49.9915928 N, 8.2312864 E). The measurements were performed between May 4th (starting time 9:30 am) and May 9th, 2018 (5:30 pm). Meteorological data were measured and provided by the Institute of Physics, also located at the campus of the university. During the measurement period, the air masses came from north, northeast or east and air mass composition can be expected to be mainly influenced by the Frankfurt Rhine-Main Metropolitan Region with approximately 5.8 million inhabitants. Figure 52 in the supplementary information (section 7.3) shows 72 h backward trajectories of the air masses (every 24 hours) from May 4th to May 10th, 2018. The aerosol was sampled in front of the laboratory window through PTFE tubes to the setup shown in Figure 14. The blank value for the seeded SOA experiments was used for the background correction. Values below the quantification limit were set to zero.

3.4.2 Results

Figure 27a) shows the concentration ratios of TPPO to TPP during the measurement period and Figure 27b) the course of the particle phase peroxide concentration. Figure 27c) shows the course of the global radiation and temperature reflecting day and nighttime. The lowest values of detected TPPO to TPP shown in Figure 27a) are very close to the estimated blank value level of 1.22% (red line) found in section 3.2.2. Values of the peroxide concentration above the limit of quantification (LOQ, blue line) were only obtained during weekdays (May 5th was a Saturday; May 6th was a Sunday) and daytime. The enhanced concentration during weekdays and daytime indicates local sources of peroxides in combination with photochemistry, an observation that is in agreement with the result from previous peroxide measurements (Hua et al., 2008; Guo et al., 2014). However, due to highly variable emission sources directly outside the chemistry building the selected measurement site was certainly not ideal for general studies about particle-phase peroxide chemistry. Nevertheless, this short proof-of-principle study demonstrates that peroxides in atmospheric aerosols can be detected by the new ORD-AMS system.

Online redox derivatization for peroxide analysis

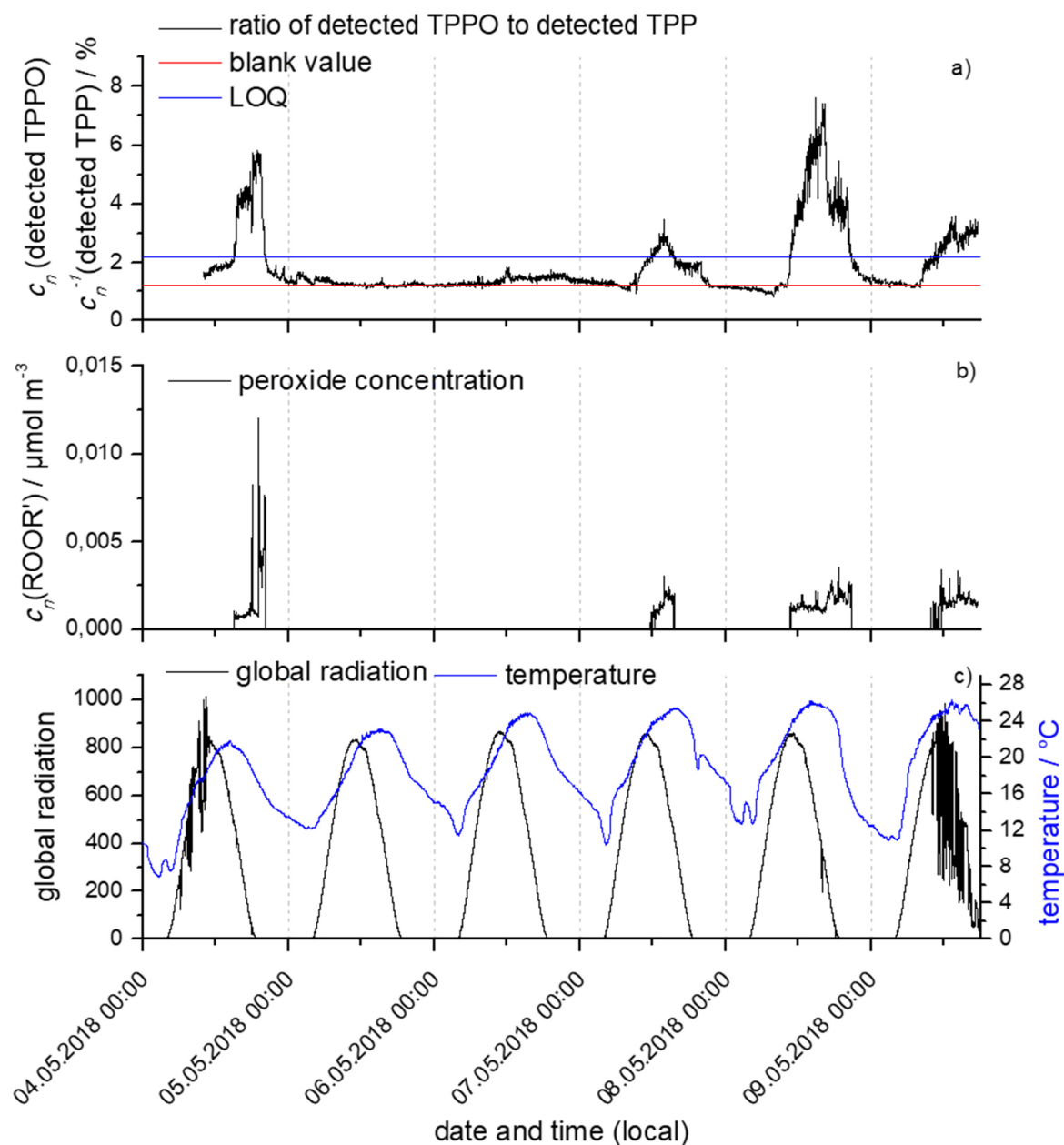


Figure 27: a) Time series of the relative amount of detected TPPO to detected TPP, LOQ and blank value, b) diurnal variation of the estimated peroxide concentration and c) time series of the global radiation and temperature.

3.5 **Conclusions**

The real-time detection of peroxides by adding gaseous TPP to aerosol particles was successfully realized using an aerosol mass spectrometer in combination with a specifically designed online derivatization unit. The ozonolysis of α - and β -pinene in the presence of ammonium sulfate seed aerosol was used to demonstrate the potential of the analytical procedure. The results clearly show the conversion of TPP to TPPO and hence the presence of peroxides in biogenic SOA. Especially in the early phase of SOA formation, the contribution of peroxides is exceptionally high (up to approx. 70%). Besides, the time-resolved measurements also show a rapid further reaction of the peroxides to non-peroxidic compounds indicative of consecutive reactions of the peroxides. The developed instrumental setup can also be used to obtain particle size-resolved information about particle-phase peroxides.

Furthermore, the method was successfully applied for the ozonolysis of monoterpenes and SOA formation in the absence of seed particles. The obtained peroxide/SOA yields at the end of the ozonolysis are in good agreement with the values determined by offline analysis (Docherty et al., 2005; Mertes et al., 2012; Li et al., 2016a; Gong et al., 2018). In addition, the high time resolution made it possible to observe a time curve that passes over a maximum of the peroxide/SOA yield. However, a continuous decrease of the yield had been expected based on the assumption made at studies using offline analysis (Mertes et al., 2012; Li et al., 2016a). As a first interpretation of the maximum, the contribution of different kind of peroxides and reactions vary during the ozonolysis. In the very beginning, reactive compounds with a high number of peroxy groups might have a larger contribution than less reactive dimers and peroxyhemiacetals, which are formed in consecutive reactions. The contribution of the dimers and peroxyhemiacetals increased with increasing amounts of oxidation products and increasing particle surface. As a result, peroxide uptake increased compared to peroxide loss, leading to the observed increase in the ratio of peroxide to SOA. An increasing rate of formation and absorption of dimers and peroxyhemiacetals compared to their chemical loss rates could be another reason for the increase in the peroxide/SOA ratio. The decrease thereafter can be explained by the increased reaction rate at the surface and inside the particle as the amount of gas phase reactants, SOA surface area and SOA mass increased. To sum up, peroxides can be considered as key compounds in the particle formation and chemical alteration in the particle phase.

Finally, the method was successfully tested in a proof-of-principle field study with ambient air outside of the laboratory. The results presented here represent the first attempt to better characterize the role of organic peroxides in atmospheric aerosols. Future laboratory and field studies are certainly needed to better understand the chemistry of peroxides in organic aerosols.

4 Online silylation

4.1 Introduction

The silylation of alcohols and carboxylic acids is a common method to convert polar, low volatile materials into nonpolar, volatile compounds for the analysis with GC-EI-MS (Rontani and Aubert, 2004). Hereby, the method provides the advantage of structure characterization due to the formation of characteristic fragment ions (Urbach, 2012; Jaoui et al., 2005; Halket and Zaikin, 2003). The molecular ion $[M]^+$ and the molecular ion with an elimination of a methyl group $[M-CH_3]^+$ are often significantly detected (Flores and Doskey, 2015). Normally, different response factors are used for the quantification whereby factors from standards are applied for unknown species with similar fragmentation patterns to one of the standards.

4.2 Method development

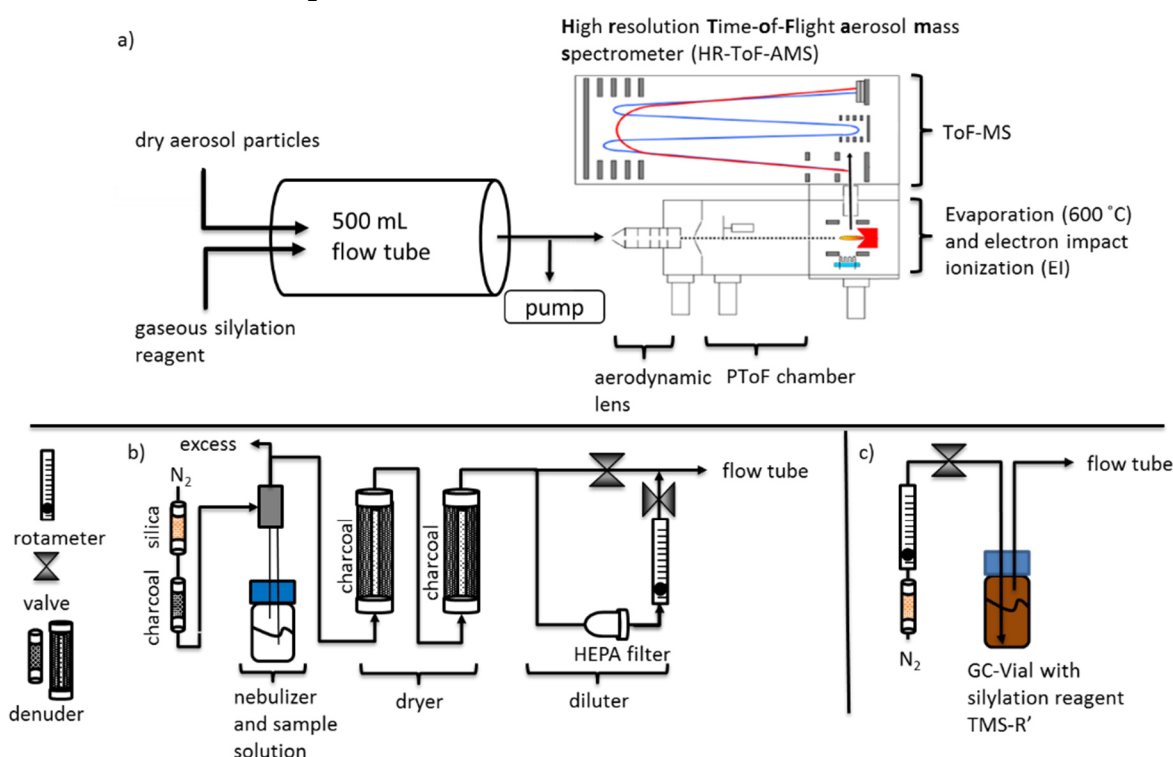


Figure 28: a) Schematic setup for the online silylation: The aerosol particles, removed from gas species and solvents, are mixed with a gaseous silylation agent in a 500 mL flow tube, where the agent condenses on the particles. The particles with the forming silylated compounds are supplied by technical nitrogen as a carrier gas to the AMS. All joints are made of glass or PTFE material. b) Aerosol generator for test compounds: The carrier gas is removed from gas-phase species by silica gel and charcoal containing denuders and supplied to the nebulizer. The particles are generated by pneumatic atomization of the respective sample solution. They are dried by flowing through charcoal and the particle concentration can be varied by a diluter. c) Transfer of the silylation agent into the flow tube by supplying dried nitrogen through the liquid agent in a GC-vial modified from Isaacman et al. (2014).

In this study, a new method for the quantitative real-time determination of hydroxyl and carboxylic groups by *in-situ* silylation is developed. To this end, particles containing alcohols or carboxylic acids are mixed with a gaseous silylation agent in a flow tube reactor, where the agent condenses on the particles and reacts to the corresponding trimethylsilyl (TMS) compounds, which are detected by an aerosol mass spectrometer (AMS) of Aerodyne Research Inc., Billerica with EI source (Figure

Online silylation

28a). Since there is no separated detection of the single aerosol components using the AMS a common response factor for all TMS compounds to determine the concentration of functional groups, had to be found. For that an offline method (Urbach, 2012) is applied to get standard solutions of which aerosols are generated containing only the respective TMS compound. Hereby, the trimethylsilyl cation (TMS^+ , $[\text{C}_3\text{H}_9\text{Si}]^+$, m/z 73) is expected to be formed for all compounds.

4.2.1 Method

Chemicals

All test compounds were purchased either from Alfa Aesar, Sigma Aldrich, Fluka, Roth, Acros Organics, Fisher Chemicals, Dr. Ehrendorfer GmbH and Supelco. Details can be found in the supporting information (section 7.4, Table 8).

Test aerosol source

The setup in Figure 28b) was used to generate the test aerosols for offline and online measurements. The aerosol was produced using a pneumatic atomizer (Modell 3076, TSI, Shoreview, MN, USA) from a solution of the respective compound. The excess air was vented before removing solvents and gas-phase species by charcoal filled denuders (inner tube: diameter = 2 cm, length 40 cm, outer tube: diameter 13.5 cm, length 40 cm) and before the setting of the aerosol concentration by a lab-built diluter.

Offline analysis

The respective alcohols, acids, and the silylation agent were added into a GC-vial and heated at 80 °C for 20 min in a drying chamber. After cooling down to room temperature, the content of the GC-vials was added to a solvent in a 100 mL screw lid glass. Different silylation agents, amounts of MSTFA in excess, solvents and concentration in solution were tested for *n*-octadecanol. The ratio of MSTFA to alcohol/carboxylic groups was about 10 mol/mol for the alcohols and 50-60 mol/mol for the carboxylic acids. The concentrations of the solutions were about 0.1 to 0.3 g/L respective to the TMS compound. The content of the vial was divided into different solvents for the carboxylic acids. The test aerosol, generated as described above, were supplied directly to the AMS with a sampling rate of 75 mL/min supported by a pump with a sampling rate of 650 mL/min. The AMS was running at the V and W mode for 2 min per data point. The mass spectra acquisition was performed in the positive ion mode (m/z range 12–546).

Details to the respective experiment can be found in Table 9-Table 10 in the supplementary information (section 7.4).

MSTFA and hexamethyldisiloxane

MSTFA was supplied by a dried nitrogen flow from a GC-Vial (Figure 28c) to a Y-piece where another nitrogen stream was added to set an appropriated concentration. The cap of the GC-Vial was sealed with PTFE and paraffin tape. The same setup was used for hexamethyldisiloxane.

Online silylation

The gaseous silylation agent was added to a 500 mL glass flow tube (35 cm length, max. diameter 4.5 cm) by supplying nitrogen through a GC-vial filled with MSTFA

(Figure 28c). The inner diameter of the PTFE tube towards the vial was 2.0 mm and the inner diameter of the tube from the vial to the flow tube was 1.4 mm. The aerosols of the test compounds were generated as described above and introduced into the flow tube. During the development of this method it became clear that the PTFE tube connecting the GC-vials with the flow tube needs to be close to the aerosol inlet inside of the reactor. MSTFA and the aerosol flow were between 70 to 100 mL/min and 500 to 700 mL/min, respectively (flow rate ratios were 0.14 to 0.17).

Data processing

The AMS data were processed by the Igor Version Pro 6.37 based programs "SQUIRREL 1.57 G" (unit mass resolution) and "PIKA 1.16H" (high resolution) according to the available online analysis guides (Field Data Analysis Guide; High Resolution ToF-AMS Analysis Guide). The raw mass spectra were analyzed for the V- and W-mode to check the yield of the reaction, the presence of hexamethyldisiloxane (silylation product of water), residual silylation agent and the by-product of the reaction and to check isobaric interference for the characteristic fragments. Missed ions and their isotopes were added to the ion list according to reasonable fragmentation patterns (successive elimination of CH₂ from the alkyl chain, available literature or reference spectra taken from the Nist or SDBS database). In the higher mass region > 200 Th, the baseline was corrected. Since only organic species were analyzed it was assumed that the organic concentration corresponds to the total aerosol concentration $c_m(\text{total})$. More than one ion with the same nominal mass of $m/z = 73$ appeared commonly so that the high-resolution signal $I(\text{TMS}^+)$ of the TMS cation was used. Note, that the signal $I(i)$ of a single ion i was converted to a nitrate equivalent signal $I_{\text{NO}_3}(i)$.

4.2.2 Results

Response factor



According Eq. 40, TMS derivatives (TMS-OR) with different residual R (alkyl, carbonyl,...) are formed by the reaction between the test compound RO-H with a silylation agent TMS-R'. It was necessary to prove the linearity between the intensity of the TMS⁺-signal $I(\text{TMS}^+, s)$ and the concentration of hydroxyl and carboxyl group $c_v(s)$ of the TMS derivative s , independent from the residual R.

According to Jimenez et al. (2003), using the EI ionization, it can be generally assumed that the fraction $\chi(i,s)$ of the signal $I(i,s)$ of ion i of species s to the total signal of all ions of that species $\sum_{\text{all } i} I(i,s)$ is constant.

$$\chi(i,s) = \frac{I(i,s)}{\sum_{\text{all } i,s} I(i,s)} \quad \text{Eq. 41}$$

According to Canagaratna et al. (2007), the signal $I(i,s)$ can be transformed to a nitrate equivalent signal $I_{\text{NO}_3}(i,s)$ and $\sum_{\text{all } i,s} I(i,s)$ to the mass concentration $c_m(s)$ of species s . The mass concentration $c_m(s)$ is related to the concentration of functional group $c_v(s)$ by:

$$c_v(s) = \frac{c_m(s) \cdot \nu(s)}{MW(s)}, \quad \text{Eq. 42}$$

where $MW(s)$ the molecular weight and $\nu(s)$ the number of hydroxyl and carboxyl groups of species s . Therefore, $\chi(i,s)$ can be expressed as conversion or response factor $\chi^*(i,s)$:

$$\chi^*(i,s) = \frac{I_{NO_3}(i,s)}{c_v(s)} = \frac{I_{NO_3}(i,s) \cdot MW(s)}{c_m(s) \cdot \nu(s)} \quad \text{Eq. 43}$$

To calculate $\chi^*(i,s)$ it was necessary to measure aerosol particles which contain only one species so that the measured total aerosol mass concentration $c_m(\text{total})$ is equal to $c_m(s)$ and that $I_{NO_3}(i, \text{total})$ equal to $I_{NO_3}(i,s)$. Those particles were generated as described in section 4.2.1 (Offline analysis). The analysis was focused on the TMS^+ ion and therefore on the determination of $\chi^*(TMS^+, s)$ with $s = TMS$ derivative ($TMS-OR$) of the respective test compound (ROH).

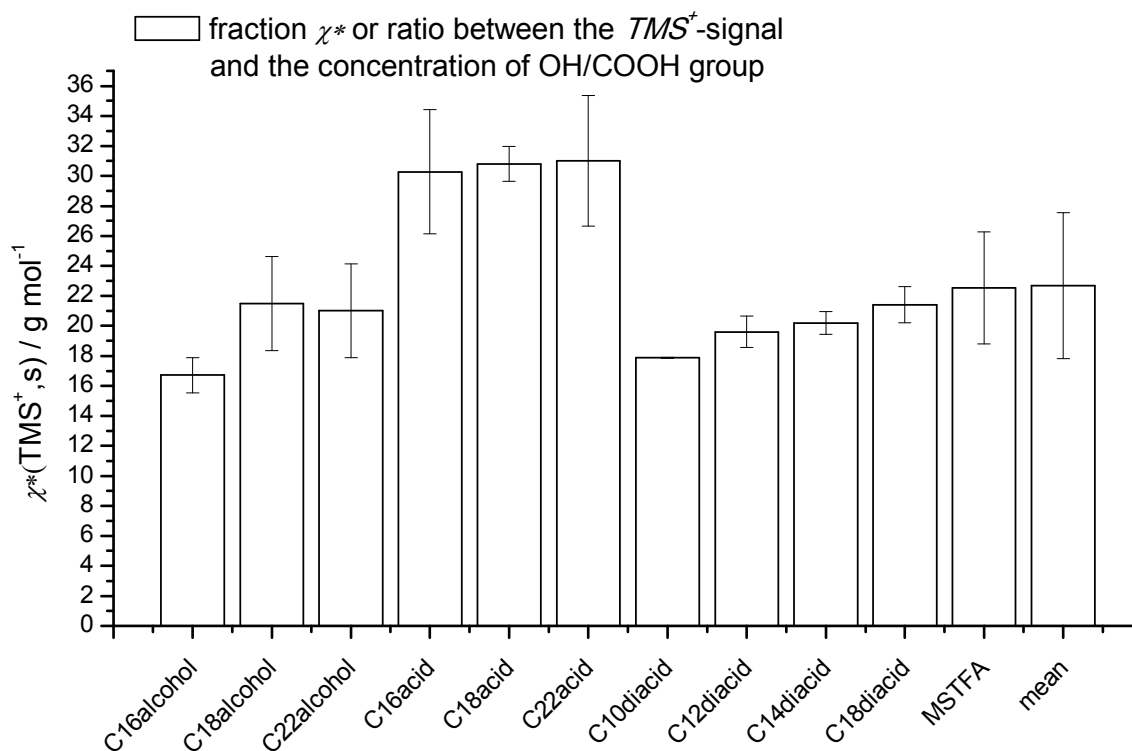


Figure 29: Response factor $\chi^*(TMS^+, s)$ of TMS-derivatives s .

For the validation of the method the transformation of *n*-octadecanol to the TMS-octadecyl ether was tested with different excesses of MSTFA, other silylation agents, different concentrations in solution, different solvents, and both ToF-MS modes (see Table 9 in section 7.4). Since no significant differences were observed ($\chi^*(TMS^+, TMS\text{-octadecyl ether}) = 21 (+/- 3) g/mol$) a complete conversion of the alcohol to the TMS ether was assumed. Only different solvents and ToF-MS modes were tested for other compounds to determine a common mean response factor $\chi^*(TMS^+)$ as presented for the individual test compounds in Figure 29. The mean value of $\chi^*(TMS^+)$ for all test

Online silylation

compounds is 23 (+/- 5) g/mol but a trend for a higher value of 31 g/mol is observed for monocarboxylic acids.

The determination of further response factors $\chi^*(i, s)$ of other characteristic fragment ions i , known from literature, was investigated and is presented in Table 2. Characteristic for every compound is the molecular peak M^+ with a methyl abstraction $[M-CH_3]^+$ (Flores and Doskey, 2015). Compounds with more than one hydroxyl or carboxyl group form the $[C_5H_{15}OSi_2]^+$ -ion at m/z 147 (Halket and Zaikin, 2003). It is also the basic peak for hexamethyldisiloxane which is the silylation product of water (Orasche et al., 2011). The ion $[C_4H_9O_2Si]^+$ at m/z 117 is detected at TMS derivatives of fatty acids (Halket and Zaikin, 2003).

Since the TMS^+ ion was detected at the measurement of pure MSTFA and since a large excess of MSTFA had to be added at the online silylation, a characteristic ion of MSTFA had to be identified. The $[M-CH_3]^+$ ion with $\chi^*([M-CH_3]^+, MSTFA) = 3.5 (+/- 0.6)$ g/mol was found to be appropriate. Furthermore, $\chi^*(TMS^+, MSTFA) = 23 (+/- 4)$ g/mol fits to the mean value of $\chi^*(TMS^+)$.

Table 2: Conversion factors $\chi^*(i, s)$ of other characteristic ions

species s Ion i	alcohols	mono acids $\chi^*(i,s) / g mol^{-1}$	diacids
$[M-CH_3]^+$	5 (+/-1)	2 (+/-1)	0.9 (+/-0.3)
$[C_5H_{15}OSi_2]^+$	0	0	1.3 (+/-0.3)
$[C_4H_9O_2Si]^+$	0	13 (+/-3)	3.0 (+/-0.3)

Online silylation of tetradecanedioic acid

To determine the yield of the online silylation reaction, the concentration of the product $c_m(\text{product})$ was compared with the concentration of the product $c_m(\text{product, cal})$ calculated from the signal of the trimethylsilyl ion $I_{NO_3}(TMS^+)$ using the common response factor $\chi^*(TMS^+)$ of 23 g/mol.

In Figure 30a)-c), the online silylation of tetradecanedioic acid demonstrates the yield determination from the measured data. For the first 20 min, the aerosol source was connected directly with the AMS. Then it was supplied through the reactor and MSTFA was added (grey background). The concentration of tetradecanedioic acid was further increased after 30 min.

The temporal course of the measured concentration of the total aerosol $c_m(\text{total})$ (black), the measured signals $I_{NO_3}([M-CH_3]^+, MSTFA)$ of MSTFA (red) and $I_{NO_3}(TMS^+, \text{total})$ of the TMS^+ ion (blue) are presented in Figure 30a). The detection of the marker ion $[M-CH_3]^+$ demonstrates the excess of MSTFA to the diacid during the silylation. The signal of the marker ion did not change due to the higher aerosol concentration after 30 min.

To obtain $c_m(\text{product})$ (black) and $I_{NO_3}(TMS^+, \text{product})$ (blue, Figure 30b) the respective parts of MSTFA were subtracted from $c_m(\text{total})$ and $I_{NO_3}(TMS^+, \text{total})$, respectively, using Eq. 44-Eq. 47. The calculated concentration of the product

Online silylation

$c_m(\text{product, calculated})$ was determined by Eq. 48 using $\chi^*(\text{TMS}^+)$ and plotted versus $c_m(\text{product})$ in Figure 30c). The 1:1 line indicates a complete transformation of the diacid to its respective bis-TMS-derivative.

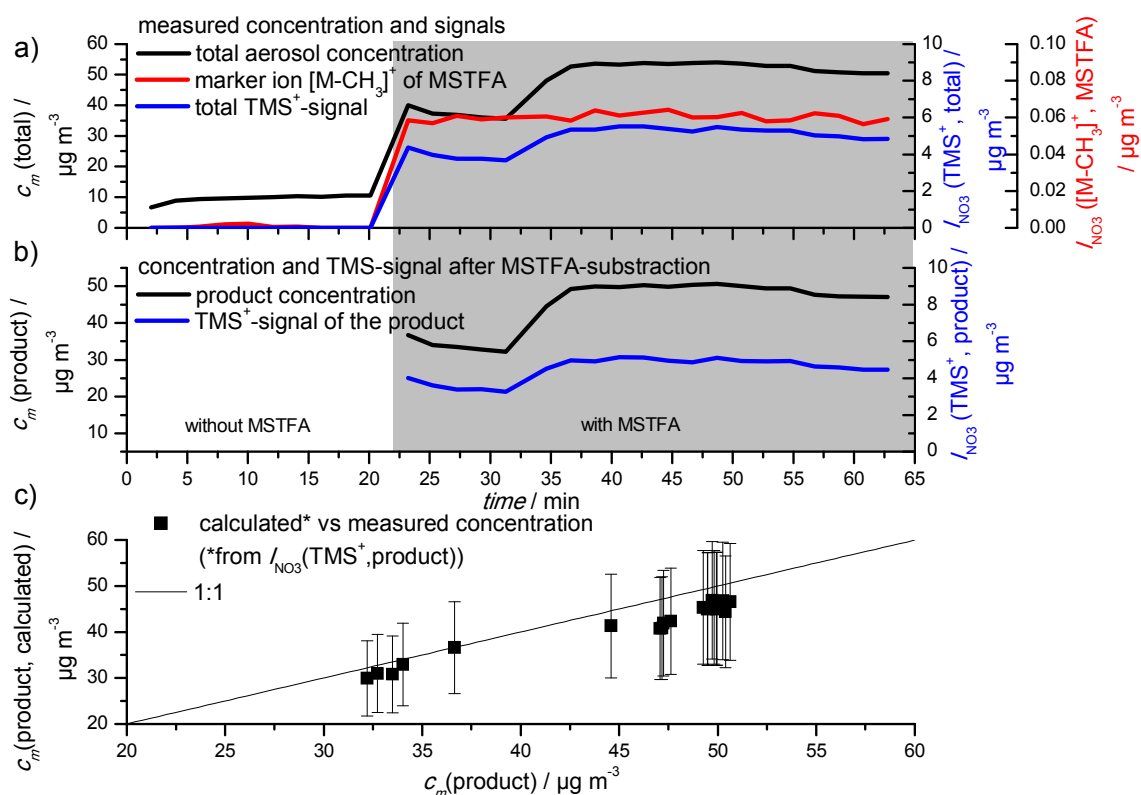


Figure 30: Determination of the yield of the online silylation of tetradecanedioic acid. The courses of a) the measured concentration of the total aerosol (black) and measured signals of the marker ion $[\text{M}-\text{CH}_3]^+$ of MSTFA (red) and the TMS ion (blue), b) the course of the part of the product on the total aerosol (black) and the TMS⁺ ion (blue) after subtracting the respective parts of MSTFA (Eq. 44-47). The grey background marks the period when MSTFA was added. c) Comparison of the concentration of the product, calculated by Eq. 48, to the concentration of the product in b).

$$c_m(\text{product}) = c_m(\text{total}) - c_m(\text{MSTFA}) \quad \text{Eq. 44}$$

$$I_{\text{NO}_3}(\text{TMS}^+, \text{product}) = I_{\text{NO}_3}(\text{TMS}^+, \text{total}) - I_{\text{NO}_3}(\text{TMS}^+, \text{MSTFA}) \quad \text{Eq. 45}$$

$$c_m(\text{MSTFA}) = \frac{I_{\text{NO}_3}([\text{M}-\text{CH}_3]^+, \text{MSTFA}) \cdot MW(\text{MSTFA})}{3.5 \frac{\text{g}}{\text{mol}}} \quad \text{Eq. 46}$$

$$I_{\text{NO}_3}(\text{TMS}^+, \text{MSTFA}) = I_{\text{NO}_3}([\text{M}-\text{CH}_3]^+, \text{MSTFA}) \cdot \frac{23}{3.5} \quad \text{Eq. 47}$$

$$c_m(\text{product, calculated}) = \frac{I_{\text{NO}_3}(\text{TMS}^+, \text{product}) \cdot MW(\text{product})}{\chi^*(\text{TMS}^+) \cdot \nu(\text{product})}, \quad \text{Eq. 48}$$

where the response factors $\chi^*([\text{M}-\text{CH}_3]^+, \text{MSTFA}) = 3.5$ (+/- 0.6) g/mol and $\chi^*(\text{TMS}^+, \text{MSTFA}) = 23$ (+/- 4) g/mol were used.

Online silylation of other test compounds

The online silylation of other long-chain alcohols and carboxylic mono- and di-acids was tested in the same manner as described for tetradecanedioic acid. In Figure 31, the calculated concentration of the respective products is plotted versus their measured concentration. Yields of about 100% were reached in general but the concentration for mono acids (dots) had a trend to be overcalculated. On the other hand, $\chi^*(\text{TMS}^+, \text{s})$ of 31 g/mol was found for mono acids during the offline measurement. Applying this factor, the ratio of $c_m(\text{product, calculated})$ to $c_m(\text{product})$ is 0.998 for *n*-octadecanoic acid and 0.988 for *n*-docosanoic acid.

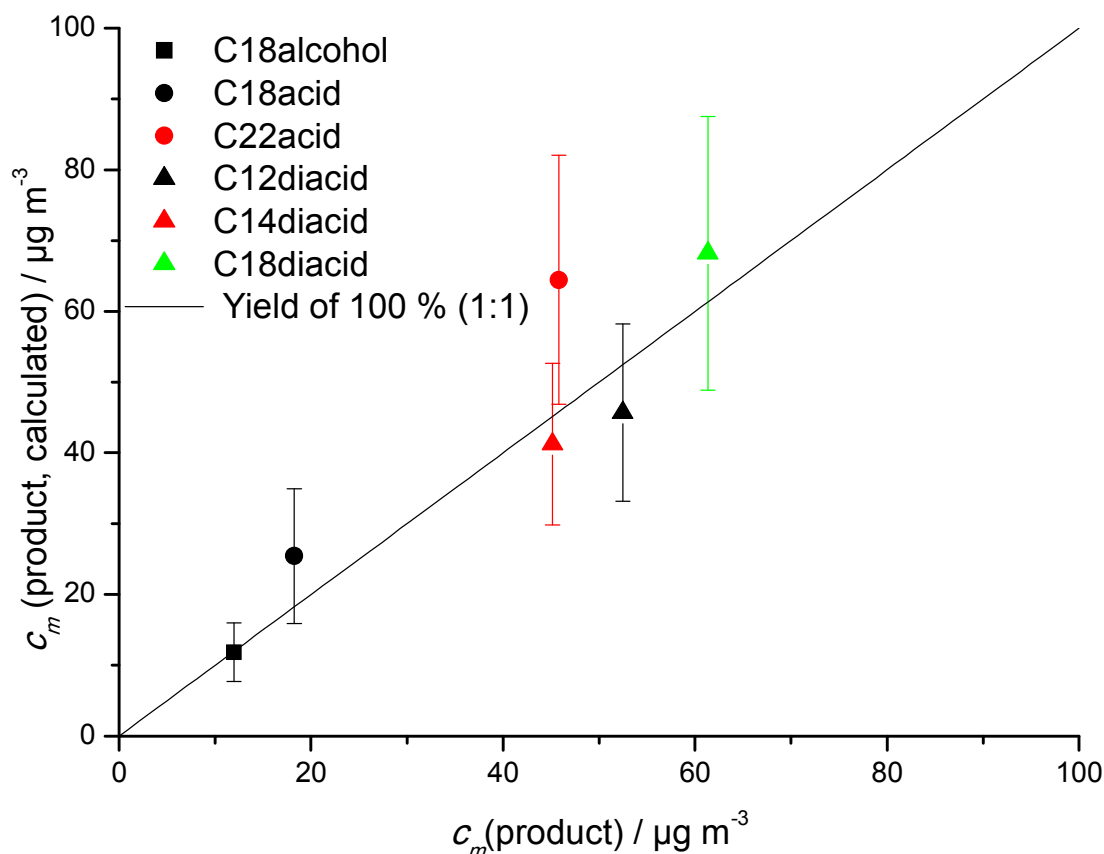


Figure 31: The calculated total mass concentration vs the measured mass concentration of the TMS derivatives of *n*-octadecanol (black square), *n*-octadecanoic acid (black dots), *n*-docosanoic acid (red dots), 1, 12 dodecanedioic acid (black triangle), 1, 14 tetradecanedioic acid (red triangle) and 1,18 octadecanedioic acid (green triangle). The calculated concentration was determined from the TMS^+ signal $I_{\text{NO}_3}(\text{TMS}^+, \text{product})$ by applying $\chi^*(\text{TMS}^+)$ in Eq. 48.

Effects on the particle and compound properties

The concentration of some of the mono and diacids (= starting material), introduced into the flow tube during the silylation reaction, was estimated from the period before the aerosol was supplied into the flow tube when $c_m(\text{total}) = c_m(\text{starting material})$ and it was calculated from $c_m(\text{product})$ by:

$$c_m(\text{starting material}) = c_m(\text{product}) \cdot \frac{MW(\text{starting material})}{MW(\text{product}) \cdot \omega}, \quad \text{Eq. 49}$$

where ω is the dilution factor, determined using the ratio between the flow rates of the aerosol with and without the MSTFA source. The comparison between the periods

before and during the silylation shows an overestimation of octadecanoic acid, dodecanedioic acid and tetradecanedioic acid by a factor of 1.26 (+/- 0.06), 1.39 (+/- 0.49) and 2.14 (+/- 0.11), respectively.

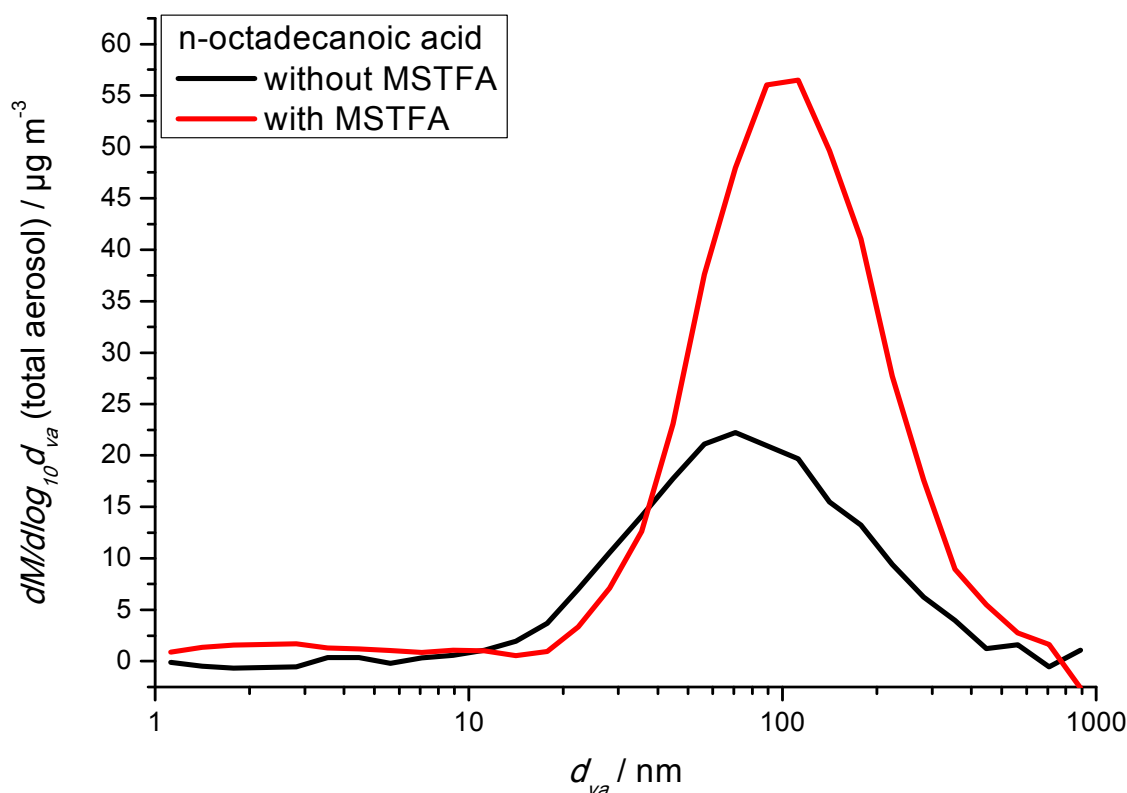


Figure 32: Size distribution of the total aerosol when supplying *n*-octadecanoic acid directly (black) and through the reactor (red) to the AMS.

Following these results, the influence of the silylation reaction on the particle size was investigated. Generally, an increase of the mean vacuum-aerodynamic diameter d_{va} was observed from $d_{va} = 76$ to $d_{va} = 104$ nm (lognormal distribution) as illustrated for the silylation of *n*-octadecanoic acid in Figure 32. The width of the distributions decreases from 1.16 to 0.89, explained by a change from an original aspherical solid to a liquid spherical particle (Zelenyuk et al., 2008). The liquefaction is expected as MSTFA is liquid and added in excess to the aerosol. Besides, MSTFA is a good solvent for TMS derivatives (Urbach, 2012). The particles containing only the starting material are measured with a lower sensitivity since aspherical and solid particles have a higher loss due to bouncing off the vaporizer of the AMS. Therefore, the liquefaction by silylation can lead to increased sensitivity (Matthew et al., 2008; Middlebrook et al., 2012) explaining the overestimation. Besides, the transmission efficiency of particles with diameters below 70 nm and above 500 nm in the aerodynamic lens of the AMS is less than 100% (Canagaratna et al., 2007; Jayne et al., 2000). Therefore, the growth of the particles due to condensation of MSTFA can lead to a higher transmission efficiency. Thus, a higher amount of the product would be detected by the AMS than expected when measuring without MSTFA. Alternatively, the ionization efficiency of trimethylsilyl compounds could be larger than the one of the starting materials because of the higher thermal stability. That also leads to higher

$\chi^*(\text{TMS}^+, s)$ and therefore to an overestimation, also discussed by Murphy (2015). However, in this study, the same ionization efficiency for the carboxylic acids, alcohols, and their TMS derivatives was applied.

Finally, the overestimation can be explained by a larger collection efficiency due to the change from solid to liquid particles, by a higher transmission efficiency due to condensation of MSTFA and an increase of the particle size or to a higher ionization efficiency of thermally stable and volatile TMS derivatives compared to their starting materials.

Silylation of short-chain alcohols and carboxylic acids

A limitation of the online silylation reaction was found concerning the molecular weight of the silylated compounds. During the silylation of alcohols with chain lengths below 18 carbon atoms, as for monoacid below 16 carbon atoms, and for diacids below 12 carbon atoms the total aerosol concentration decreased strongly when MSTFA was added. This indicates the evaporation of the particles. The silylation of adipic acid can be seen as an example in Figure 33.

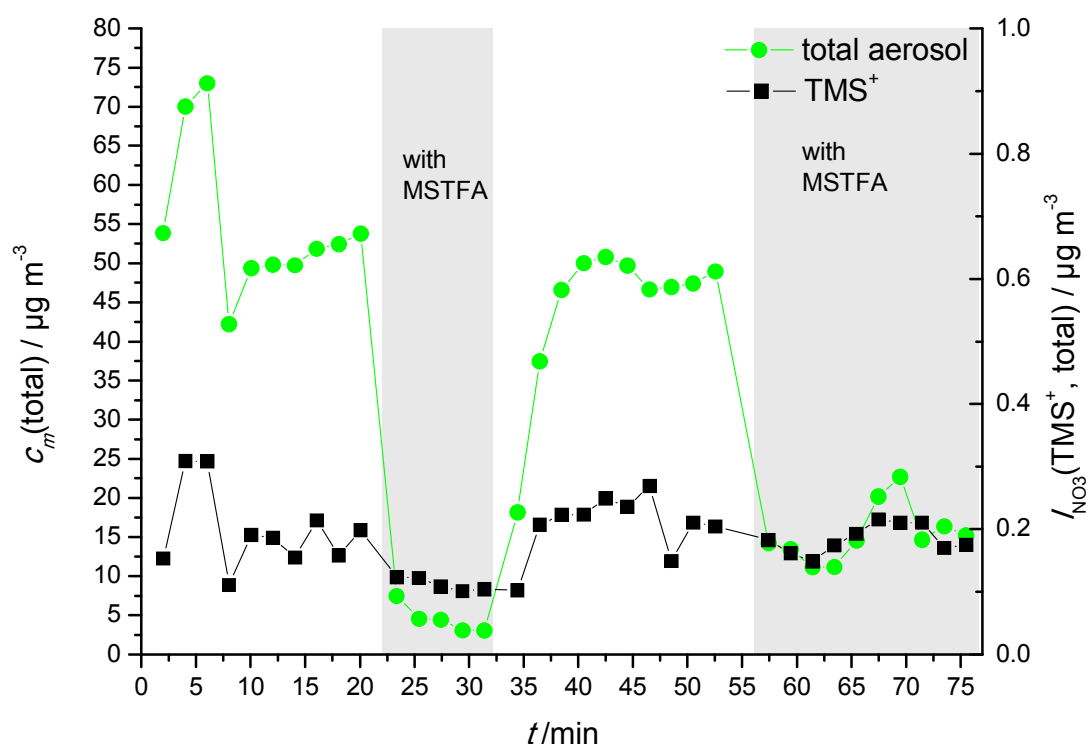


Figure 33: Vaporization of the silyl-ester of adipic acid when MSTFA is added (grey marked).

An estimation of vapor pressures is presented in Table 3 using the program EPIWeb4.11. It shows that the vapor pressure has to be below 0.02 Pa (25 °C) for monosilylated alcohols and acids and below 0.07 Pa (25 °C) for diacids. The vapor pressure of the tris-trimethylsilyl ether of levoglucosan, a biomass burning marker, is low enough but derivatives of pinonic and pinic acid, products of the ozonolysis of monoterpenes, would be not detected. Silylation agents with tributylsilyl (TBS) groups could be a useful alternative (Halket and Zaikin, 2003) to those with trimethylsilyl groups. Here, a chain length of 8 C-atoms for monosilylated compounds

Online silylation

is expected to be sufficient and that even the derivative of oxalic acid (C2 dioic acid) is detectable. On the other hand, a larger silyl group could decrease the yield of the reaction because of steric effects (Poole, 2013).

Table 3: Estimated vapor pressure of trimethylsilyl- and tributylsilyl derivatives.

	Vapore pressure (25 °C) / Pa, (chain length)	
	evaporation expected	detectable
<i>mono alcohols</i>		
TMS derivative	$1.5 \cdot 10^{-2}$ (C16)	$2.8 \cdot 10^{-3}$ (C18)
TBS derivative	$3.8 \cdot 10^{-2}$ (C06)	$6.4 \cdot 10^{-3}$ (C08)
<i>mono acids</i>		
TMS derivative	$1.4 \cdot 10^{-2}$ (C14)	$2.4 \cdot 10^{-3}$ (C16)
TBS derivative	$1.1 \cdot 10^{-2}$ (C06)	$2.1 \cdot 10^{-3}$ (C08)
<i>dioic acids</i>		
TMS derivative	$7.3 \cdot 10^{-2}$ (C10)	$1.9 \cdot 10^{-2}$ (C12)
TBS derivative		$1.1 \cdot 10^{-4}$ (C02)
<i>further compounds</i>	TMS derivative	TBS derivative
Pinonic acid	$6.6 \cdot 10^{-1}$	$8.6 \cdot 10^{-5}$
Pinic acid	$2.9 \cdot 10^{-1}$	$4.5 \cdot 10^{-5}$
Levogluconan	$4.6 \cdot 10^{-5}$	$1.3 \cdot 10^{-12}$

4.3 Online silylation at ambient aerosols

4.3.1 Method

The online silylation (section 4.2) was tested for ambient air in front of the window of our laboratory in Mainz on 18/08/2017 from 10 a.m. to 3 p.m. The aerosol was partly supplied directly or via the reactor (Figure 28a)) to the AMS. Meteorological data were measured and provided by the Institute of Physics.

Hexamethyldisiloxane was measured using the setup as for MSTFA (Figure 28c), described in section 4.2.1.

4.3.2 Results

In Figure 34), the time series of the organic aerosol concentration with the ambient air supplied directly to the AMS (white background) is shown. Figure 34b) illustrates the time series of the residual organic aerosol after the subtraction of the concentration of MSTFA and hexamethyldisiloxane (HMDSO) at the addition of MSTFA (grey background) using Eq. 50. Figure 34c) shows the respective TMS⁺-signals (calculated using Eq. 51) during the addition of MSTFA to the particles. The signal of the ion $[C_5H_{15}OSi_2]^+ I_{NO_3}([C_5H_{15}OSi_2]^+)$ was used to calculate the HMDSO concentration $c_m(\text{HMDSO})$ and its TMS⁺-signal $I_{NO_3}(\text{TMS}^+, \text{HMDSO})$ using Eq. 52 and Eq. 53. $MW(\text{HMDSO})$ is the molecular weight of HMDSO. The parts of MSTFA were subtracted as described using Eq. 44-47.

$$c_m(\text{organic}) = c_m(\text{total}) - c_m(\text{MSTFA}) - c_m(\text{HMDSO}) \quad \text{Eq. 50}$$

$$\begin{aligned} I_{NO_3}(\text{TMS}^+, \text{organic}) & \quad \text{Eq. 51} \\ &= I_{NO_3}(\text{TMS}^+, \text{total}) - I_{NO_3}(\text{TMS}^+, \text{MSTFA}) \\ & \quad - I_{NO_3}(\text{TMS}^+, \text{HMDSO}) \end{aligned}$$

$$c_m(\text{HMDSO}) = \frac{I_{NO_3}([C_5H_{15}OSi_2]^+) \cdot MW(\text{HMDSO})}{1.03 \frac{g}{mol}} \quad \text{Eq. 52}$$

$$I_{NO_3}(\text{TMS}^+, \text{HMDSO}) = I_{NO_3}([C_5H_{15}OSi_2]^+) \cdot \frac{0.21}{1.03} \quad \text{Eq. 53}$$

Online silylation

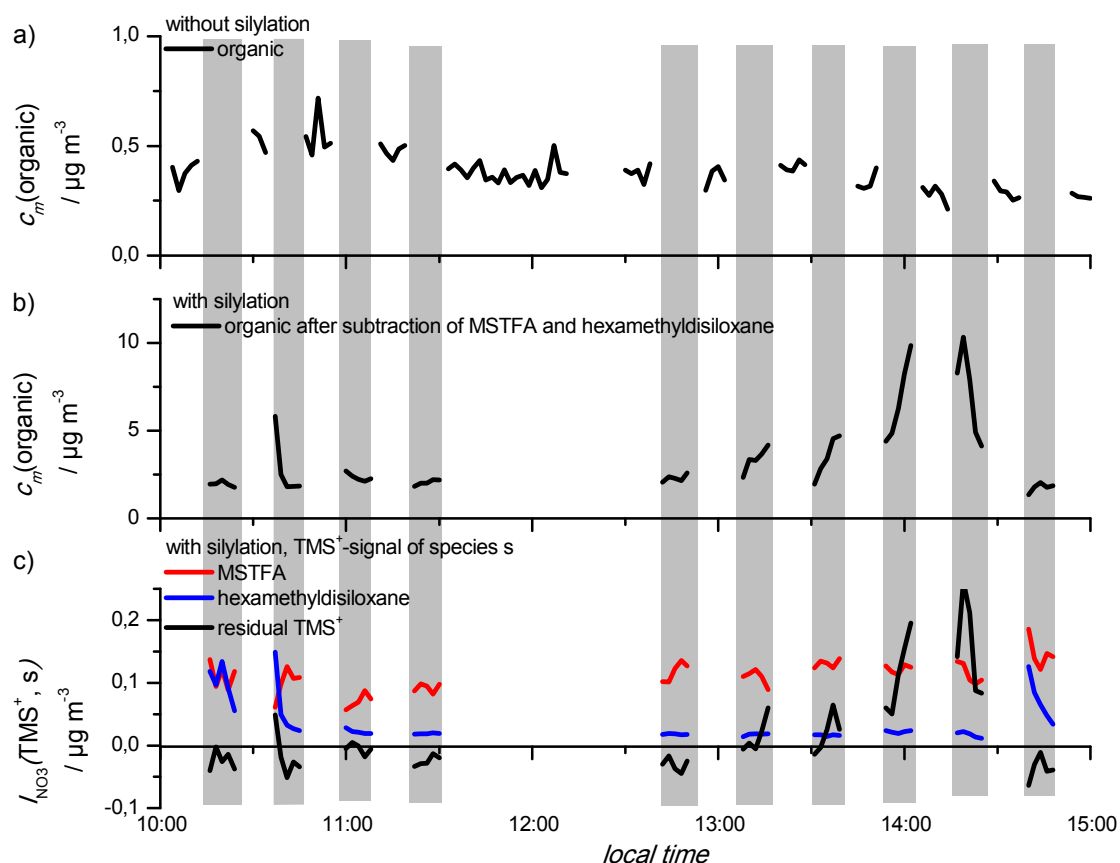


Figure 34: Ambient air measurement on 18/08/2017. a) Measured organic aerosol. b) The concentration of the residual organic aerosol when MSTFA was added. c) TMS⁺-signal of MSTFA (red), hexamethyldisiloxane (blue), and the residual organic aerosol (back) when MSTFA was added. The periods with silylation are highlighted in grey, the periods without silylation in white.

As illustrated in Figure 34a), the organic concentration of the original particles did not change strongly during the day. The residual TMS⁺ signal corresponding to aerosol components increased between 1:04 p.m. and 2:30 p.m. to values above zero (Figure 34c). The same course is obtained in Figure 34b). For the rest of the measurement time, however, the measured TMS⁺ signal corresponds mainly to the TMS⁺ signals of hexamethyldisiloxane and MSTFA.

Silylation of water

In Figure 37b), the time series of water and the relative humidity RH are illustrated. The water concentration $c_m(\text{H}_2\text{O})$ is calculated from the concentration of HMDSO (Eq. 54), assuming that HMDSO is mainly produced by the silylation of water.

$$c_m(\text{H}_2\text{O}) = c_m(\text{HMDSO}) \cdot \frac{MW(\text{H}_2\text{O})}{MW(\text{HMDSO})}, \quad \text{Eq. 54}$$

where $MW(\text{H}_2\text{O})$ is the molecular weight of water.

Losses of HMDSO by evaporation in the reactor, during the transmission from the inlet to the vaporizer of the AMS and by the adsorption of water on the silica denuder are not included. While RH started to increase strongly between 2:00 p.m. and 2:30 p.m., it also started to rain (0 to 2.3 mm). There is a decrease in the water concentration

and the relative humidity during the morning, but in the afternoon, the concentration of water had increased after *RH* reached already 100%.

According to Ovadnevaite et al. (2011), organic surfactants inhibit the water uptake under subsaturating conditions, but they increase it at supersaturation, observed at marine aerosols enriched with organic matter. In the period between 2:00 p.m. and 2:30 p.m., when the temperature was decreasing and *RH* was increasing, there is also an increased residual TMS⁺-signal (Figure 34c), indicating an increased concentration of organic compounds. These organic compounds might have inhibited the water uptake before *RH* reached 100%. Therefore, the measured water concentration would reflect rather the amount of water in the particles than the total water content in the particle and gas phase. Besides, if gaseous water had contributed significantly to the measured HMDSO concentration its course would have been more similar to *RH*. If the losses of HMDSO during the transmission from the reactor to the vaporizer of the AMS are estimated a quantification of particle water will be possible.

Silanols in atmospheric aerosols?

The mass spectra in Figure 35a) shows enhanced intensities of signals at $m/z \geq 200$ when MSTFA was added in contrast to the measurements of the original aerosol (Figure 35b) without MSTFA. According to Yu et al. (2009), the signals at m/z 207-209, 281-283, 221-223, and 295-297 originate from siloxanes and their respective isotopes with chemical formulas $[(\text{SiOC}_2\text{H}_6)_n\text{Si}(\text{CH}_3)_3]$ and $[(\text{SiOC}_2\text{H}_6)_n\text{SiOCH}_3]$, respectively, which was confirmed by peak analysis at these masses during the data processing (supplement, section 7.5). The masses 239 and 255 are not known to originate from silanols or siloxanes. These signals should originate from other types of compounds.

Yu et al. (2009) and Timko et al. (2009) found silicone tubes as possible sources for siloxanes but only the cap of GC vial is known as silicone-containing material. Signals of the type of the ions $[(\text{SiOC}_2\text{H}_6)_n\text{Si}(\text{CH}_3)_3]$ were also found in the background mode of the AMS indicating a siloxane material in there.

However, according to Latimer et al. (1998), Chandramouli and Kamens (2001), Wu and Johnston (2016), Coggon et al. (2018), and McDonald et al. (2018) volatile methyl siloxanes originate from solvents, lubricants, penetrating oils, and various personal care products, found in outdoor and indoor air. As the offices of some research groups were very close to the measurement site, they might be local sources. Siloxanes are oxidized mainly by OH-radicals to silanols and are absorbed on aerosol particles afterwards. The concentration depends on the chemical composition of the particles, temperature, and relative humidity. For example, stronger gas-particle partitioning was found for 1-hydroxynonamethyl-cyclopentasiloxane (D₄TOH) on Diesel soot and especially on mineral dust than on wood and coal soot (Latimer et al., 1998). D₄TOH is the oxidation product of decamethyl cyclopentasiloxane D₅ (0.174 mm Hg at 25 °C). The partitioning rate decreases generally at increased temperatures. Furthermore, there is an increase at lower *RH* on dust particles, explained by higher surface-to-volume ratio for solid particles respective to liquid particles, and an increase on coal and wood combustion particles.

Online silylation

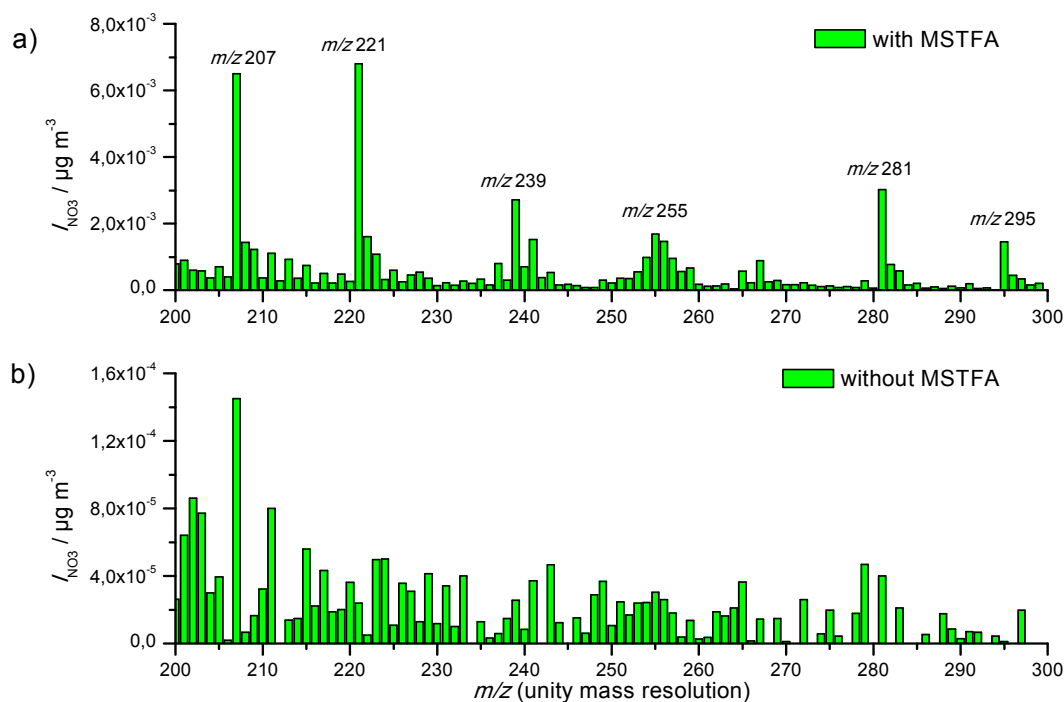


Figure 35: Mass spectra (unit mass resolution) of measured organic bulk aerosol in the range of m/z 200 -300, a) with b) without the addition of MSTFA.

The reaction of silanols with MSTFA yields siloxanes which will be called TMS-silanol ethers here to distinguish them from the precursor of the silanols (Figure 36). It should be noted that the TMS-silanol ethers ($D_{n-1}TO-TMS$) are isomers of the respective cyclic siloxane precursor (D_n) with an additional $SiOC_2H_6$ group (Figure 36a). Silanols ($MD_{n+1}OH$) from the oxidation of linear polymethylsiloxanes (MD_nOM) react with MSTFA to TMS silanol ethers ($MD_{n+1}O-TMS$), the same compound as $MD_{n+1}OM$ (Figure 36b). As illustrated in Table 4, the signals of the nominal masses 207, 281, 355, 429, and 503 correspond to silylated silanols from cyclic polymethylsiloxane precursors and the signals of the nominal masses of 221, 295, and 369 to silylated silanols from linear polymethylsiloxane precursors.

Online silylation

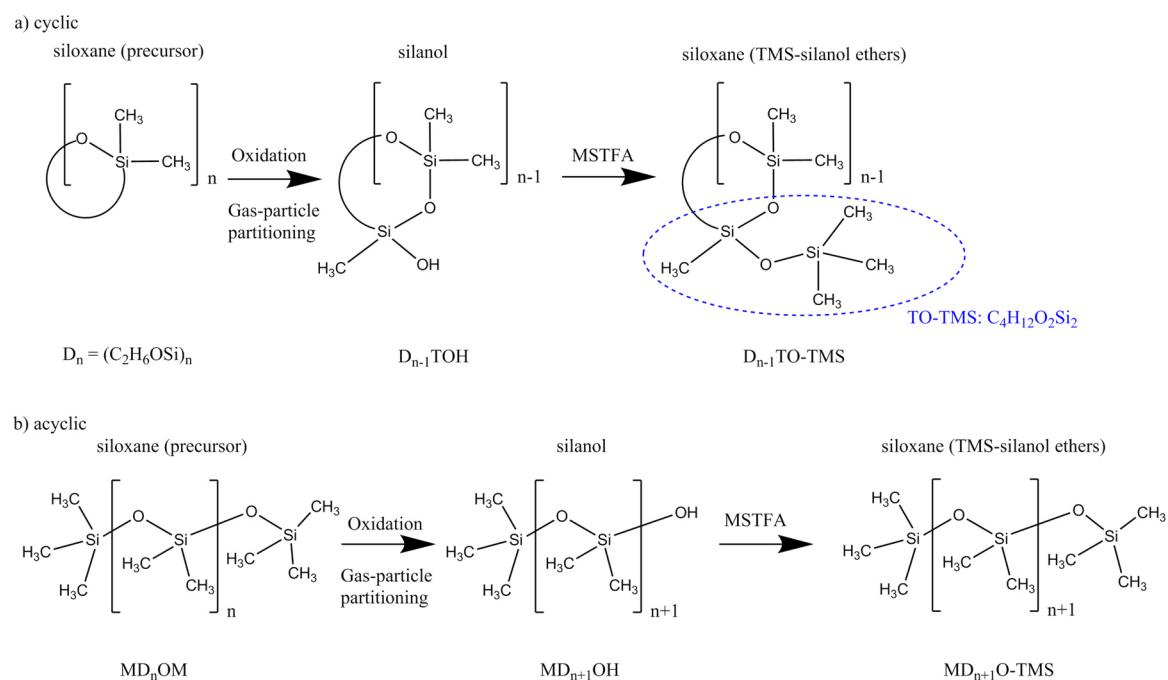


Figure 36: Oxidation of a) cyclic and b) acyclic polymethylsiloxanes to silanols and their silylation to siloxanes (TMS-silanol ethers).

Table 4: Relation between the cyclic and acyclic polymethylsiloxane precursor, the silanols as their oxidation product, the TMS-silanol ether and the nominal mass of the $[M-CH_3]^+$ of TMS-silanol-ethers.

Polymethylsiloxane - precursor	Silanol	TMS-silanol ether	$m/z [M-CH_3]^+$
D_n (n: 2 – 6)	$D_{n-1}TOH$	$D_{n-1}TO-TMS$	207, 281, 355, 429, 503
MD_nOM (n: 0 – 2)	$MD_{n+1}OH$	$MD_{n+1}O-TMS$	221, 295, 369

The time series of the masses 207 and 221 in Figure 37a) show an increased signal between 12:40 p.m. and 2:30 p.m. highlighted as silanol event followed by a strong decrease afterwards. The other highlighted masses in Figure 35a) have similar time courses as those of m/z 207 and 221. As indicated by the decrease of the water concentration and RH (Figure 37b) during the morning, the particles were dry and solid in the afternoon. These conditions would facilitate the condensation of silanols on the particles as confirmed by the increased TMS-silanol related signals. The temperature-drop between 2:00 p.m. and 2:30 p.m. enhanced this effect. The strong decrease of these signals between 2:30 p.m. and 3:00 p.m. coincides with an increase of water at this time.

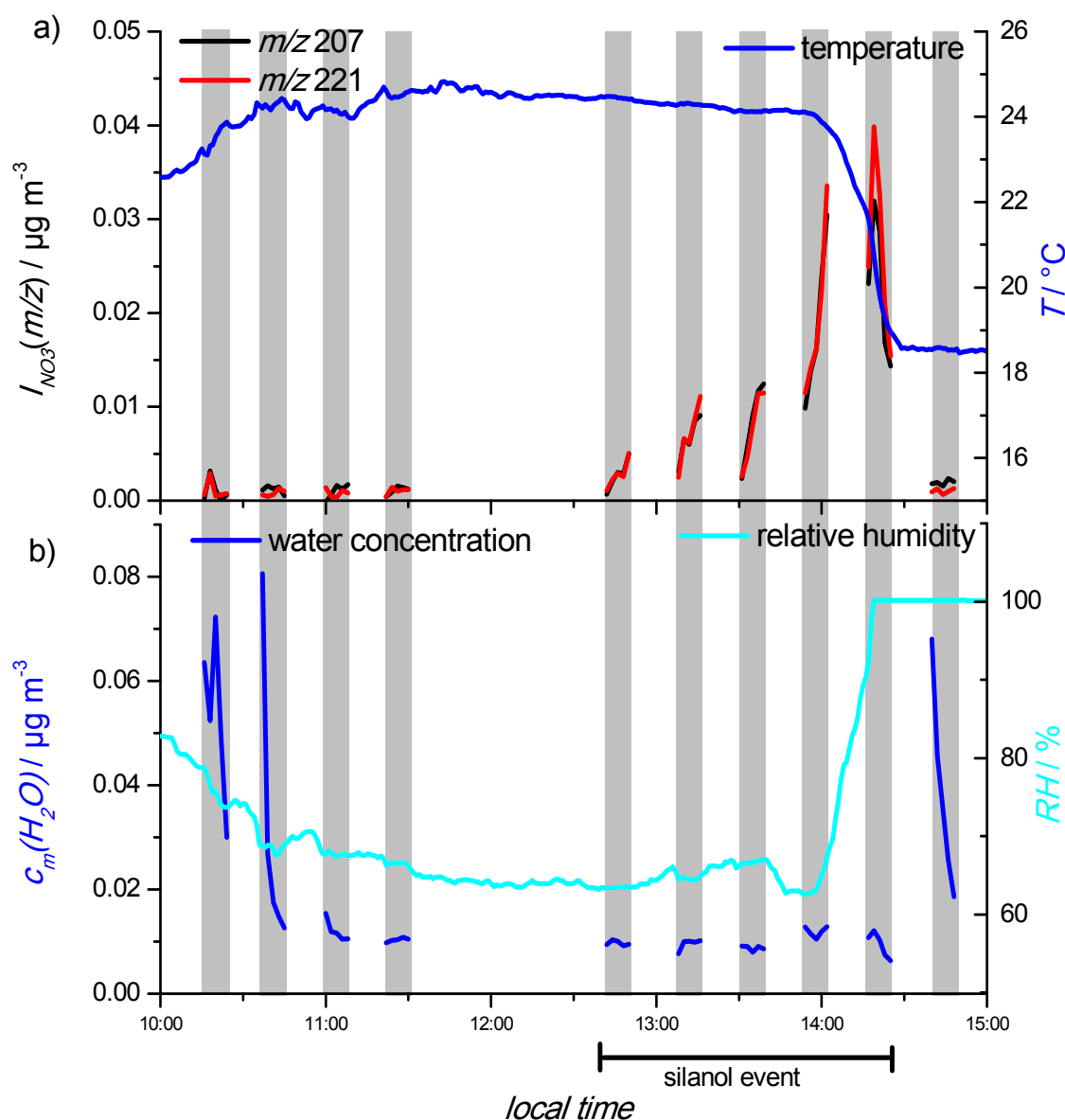


Figure 37: Time series of a) the signals at m/z 207 and m/z 221, and of the temperature (blue) b) the water concentration (blue) and the relative humidity (cyan). The period with increased siloxane-related signals was called silanol event.

The time series of the masses 207 and 221 in Figure 37a) show an increased signal between 12:40 p.m. and 2:30 p.m. highlighted as silanol event followed by a strong decrease afterwards. The other highlighted masses in Figure 35a) have similar time courses as those of m/z 207 and 221. As indicated by the decrease of the water concentration and RH (Figure 37b) during the morning, the particles were dry and solid in the afternoon. These conditions would facilitate the condensation of silanols on the particles as confirmed by the increased TMS-silanol related signals. The temperature-drop between 2:00 p.m. and 2:30 p.m. enhanced this effect. The strong decrease of these signals between 2:30 p.m. and 3:00 p.m. coincides with an increase of water at this time.

Online silylation

The size distributions of sulfate and the siloxane-related signal at m/z 221 for the silanol event (red) and the residual time (black) are illustrated in Figure 38. The silanol-TMS-related signals were found only during the silanol-event. One mode is with a 350 nm mean diameter in the same area as the sulfate distribution with a 400 nm mean diameter. Additionally, a larger peak is found for particles with 1300 nm mean diameter indicating the condensation of silanols on mineral dust, typically found in larger particles (Kolb and Worsnop, 2012; Pandis, 2004). These findings confirm the results of Latimer et al. (1998), where a preference was observed for the condensation of D₄TOH on dust particles respective to diesel, coal and wood soot.

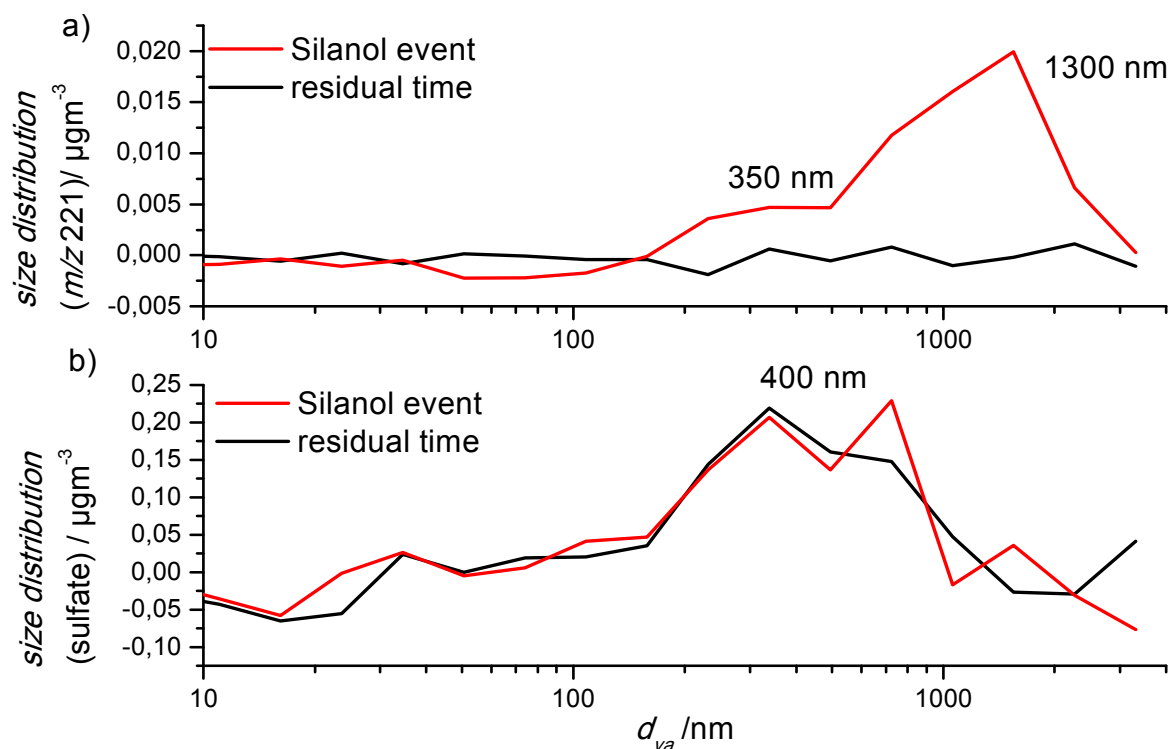


Figure 38: Size distribution of a) the TMS-silanol-ether related signal at m/z 221 and b) sulfate. It is distinguished between the periods during the silanol event (red) and of the residual time (black) when MSTFA was added to the aerosol.

However, since the TMS-silanol ether-related signals were also found in the offline and online measurements of test compounds they might be artifacts from the setup, e.g. the silicone cap of the GC vial. They would not be distinguishable from the silylated silanols as they showed similar condensation behavior. In future investigations, the oxidation of silanols and the condensation of the resulting silanols can be simulated in chamber experiments to elaborate if silanols can be detected using online silylation.

Finally, the online silylation of outdoor aerosols showed the opportunity to identify individual species as water and silanols. As similar compounds are detected with similar sensitivity, post-calibration with standard compounds having similar fragmentation patterns would enable the quantification of the individual species.

4.4 **Conclusion**

In this study it was shown that long-chained alcohols and carboxylic acids can be transformed quantitatively into the corresponding TMS-derivatives and be monitored using the AMS. A common response factor enables the determination of the concentration of hydroxyl and carboxylic groups of this kind of compounds. Further investigation of the derivatization of multifunctional compounds has to be done in order to reveal electronic or steric influences on the response factor and if other characteristic fragments can be used for the quantitative structure analysis.

A limitation of the presented method is the evaporation of trimethylsilyl derivatives with carbon chain lengths below 18 carbon atoms for alcohols, 16 carbon atoms for monoacids, and 12 carbon atoms for diacids. The silylation with tributylsilyl agents could potentially compensate for this effect. Furthermore, it is known that aldehydes and ketones form adducts with the silylation agent showing characteristic fragments as well.

Finally, the online silylation reaction was tested on outdoor aerosol. Although almost no organic species were present in the aerosol, trimethylsilyl derivatives of silanols were identified using the AMS. Their source might be solvents, lubricants, penetrating oils, and various personal care products found in outdoor and indoor air. However, positive artifacts from the setup cannot be excluded completely. Nevertheless, the identification of these silanols shows the possibility to obtain qualitative information about the single components in the aerosol. Furthermore, online silylation can be an approach to measure the particle water content.

5 Summary and Outlook

During this Ph.D. thesis, two methods were developed to quantify organic functional groups in aerosol particles. The achieved goals are summarized in Table 5.

Table 5: Achieved goals at ORD-AMS for peroxide analysis (chapter 3) and the online silylation (chapter 4). \checkmark = goal achieved, (\checkmark) = goal achieved under certain circumstances, ? = not investigated.

Goals	ORD-AMS	Online silylation
1. Derivatization product / agent	TPPO/TPP	TMS-OR / MSTFA
- identified by a specific marker ion	\checkmark	(\checkmark)
- quantifiable using AMS	\checkmark	(\checkmark)
- sensitive to	(?)	hydrolysis
2. Development of the agent source	\checkmark	\checkmark
3. Condensation of the agent onto the particles	\checkmark	\checkmark
4. The quantitative yield of the reaction	(\checkmark)	\checkmark
- product remaining in the particle phase	\checkmark	(\checkmark)
- aggregate state	(\checkmark)	\checkmark
- matrix effects	?	?
- electronic and steric effects	?	?
5. Application at outdoor aerosols	\checkmark	(\checkmark)

For the analysis of peroxides (chapter 3), triphenylphosphine (TPP) was identified as a derivatization agent. It was oxidized to triphenylphosphine oxide (TPPO) in a redox reaction with peroxides. Both compounds showed specific marker ions due to the low fragmentation of the aromatic structures. TPP and TPPO were quantified from these marker ions using the aerosol mass spectrometer (AMS). For the application as an online technique TPP was enriched in the carrier gas nitrogen using a modified Sinclair-La Mer generator. The mixing of TPP with aerosol particles led to a strong condensation of TPP on the particles. These particles were further supplied to the AMS.

Secondary organic aerosol (SOA) species containing peroxide groups were produced as test aerosols in the ozonolysis of monoterpenes with and without the presence of seed particles. Only a small amount of background TPPO was detected upon the addition of TPP to the pure seed particles containing non-reactive ammonium sulfate. A strong increase of the peroxide amount was observed after mixing the seed particles with SOA species and at the particle new formation and growth of pure SOA. The yields of peroxide reacting to SOA, as found in the final stage of the experiments, were in good agreement with the yields found in literature. Furthermore, size-dependent information about the peroxide and SOA was obtained using the AMS showing further evidence of the reaction of TPP with peroxides. Finally, the new online redox derivatization (ORD)-AMS method was applied in outdoor measurements. The technique was sensitive enough to observe the increase in peroxide concentration during daytime on working days.

Summary and Outlook

However, background TPPO was observed during the condensation of TPP on ammonium sulfate seed and pure TPP particles. The origin of this background might be the reaction of TPP with oxygen during storing or with peroxides in the gas-phase or in the applied solvent. Nevertheless, a background correction was applied because the amount of background TPPO was depended on the detected TPP concentration. In future studies, the number of possible oxidants in the gas-phase could be reduced using denuders coated with a film of reactants.

Furthermore, the particle's aggregation state, the particle-matrix, electronic and steric groups of the peroxides might affect the yield of the reaction of TPP with the peroxide and need to be further investigated. However, the SOA and SOA-seed experiments were conducted at room temperature and relative humidities above 50% which favor the liquid state. Therefore, a complete mixing of TPP with the particle species is assumed. The yields of peroxide reacting to SOA were also close to the literature values, which supports the assumption of a quantitative reaction of TPP with the peroxides. Further validation of this method could be achieved by applying filter sampling and iodometric detection simultaneously to the ORD-AMS measurement. As this offline method is affected by artifacts due to the reactive nature of the peroxides, filter sampling of the aerosol could also be applied after the addition of TPP. In doing so, the peroxide information in the aerosol would be conserved in the resulting TPPO which can be analyzed using offline techniques.

Besides the method development, information about the fate of peroxide in SOA was obtained in the ozonolysis of monoterpenes. Surprisingly, the yield of peroxide to SOA showed a maximum in the early stage of the experiment instead of a continuous decrease as expected from literature. The decrease was explained by an increase of reactions on the particle surface and in the bulk which is also supported by previous reference studies. However, filter sampling and iodometric detection were applied in the reference studies. The detection of a maximum was not observed there due to a lower time resolution. Finally, an increasing contribution of less reactive peroxide dimers and peroxyhemiacetals relative to the contribution of highly reactive polyperoxides has been proposed as one explanation for the increase in peroxide yield. Alternatively, dimers and peroxyhemiacetals are formed as chained molecules in secondary reactions compared to first generation products. As long as the amount of oxidation products increases, more dimers and peroxyhemiacetals are formed than continue to react in the particles with loss of peroxide function. This would also increase the peroxide yield.

A further possible extension of this technique is a combination of the ORD setup with mass spectrometers with soft ionization sources. The mass spectra of the aerosol supplied through the ORD setup then needs to be compared to the mass spectra of the aerosol supplied directly to the mass spectrometer. Mainly quasi-molecular ions are detected using soft ionization sources and thus single compounds can be identified. As only peroxides react with TPP a reduction of the signals of m/z s, corresponding to the peroxide when the aerosol is supplied through the ORD setup, is expected. In contrast, an increase in the signals of m/z s corresponding to the compounds which are formed by the reaction is expected as well. Therefore, the combination of the ORD

Summary and Outlook

setup with soft ionization mass spectrometry will result in qualitative information of peroxides in the aerosol.

In conclusion, a new ORD method for the analysis of peroxide was successfully developed. It is applicable to outdoor aerosol and gives detailed information about the time course of the peroxide content in SOA. Further studies can investigate the influence of the aggregation state, the particle-matrix, electronic, and steric groups of the peroxide on the yield of the reaction. Further extensions of the method can be ORD filter sampling or ORD soft ionization mass spectrometry to validate the method and to get qualitative information about peroxide in aerosols, respectively.

For the online silylation (chapter 4), *N*-Methyl-*N*-trimethylsilyl trifluoroacetamide (MSTFA) was identified as a derivatization agent. It reacts with alcohols and carboxylic acids yielding trimethylsilyl (TMS) ethers and esters (TMS-OR). In contrast to the ORD-AMS method for the peroxide analysis, the derivatization products differ from the organic rest R of the respective alcohol and acid. Therefore, the development of the method was divided into two parts.

At first, trimethylsilyl derivatives were formed by reference methods and detected using the AMS (offline silylation). The trimethylsilyl derivatives of long-chained mono alcohols, organic mono-, and diacids produced the trimethylsilyl cation (TMS⁺) as common ion in the electron impact ionization source of the AMS. The cation was identified by the isotope pattern due to the Si atom although several ions were found at the same nominal mass. The signal intensity of TMS⁺ was linear to the amount of hydroxyl and carboxylic groups independent on the organic rest. A common response factor was determined to convert the intensity of the TMS⁺ signal to an amount of hydroxyl and carboxylic groups. Further characteristic fragment ions were found which can be used for structural analysis of the aerosol components.

Secondly, a test gas source for MSTFA was developed for the online silylation. For this purpose, the carrier gas nitrogen was saturated with MSTFA by supplying nitrogen through a vial filled with MSTFA and mixed with aerosol particles. The silylation reagent condensed in a sufficient amount on the particles leading to the reaction with the respective test components. The same response factor as in the offline silylation was found for long-chained mono-alcohols, mono-, and diacids showing a quantitative conversion of these compounds to their TMS derivatives. A conversion into liquid particles was assumed as the liquid MSTFA was added in excess which, according to literature, is also a good solvent for TMS derivatives. However, like in the ORD-AMS method the effect of the structure and other functional groups of the test compounds on the yield of the reaction and the common response factor requires further investigation.

The presence of water and residual MSTFA presented a challenge. Water reacts with TMS derivatives yielding hexamethyldisiloxane (HMDSO), the non-silylated alcohol, and carboxylic acid. As water is present in a high amount in the atmosphere, MSTFA had to be added in a large excess to the aerosol in order to avoid hydrolysis of the TMS derivatives. As HMDSO and MSTFA both produced the [TMS]⁺ ion during the ionization, specific marker ions for these compounds were used to subtract their part

Summary and Outlook

on the TMS⁺ signal. According to literature, other functional groups such as amines, aldehydes, and ketones, react with silylation agents as well. In future studies, a further correction procedure has to be developed for their derivatives.

The online silylation was tested for alcohols and acids with shorter carbon chains as well. Here, the aerosol concentration strongly decreased when MSTFA was added indicating the vaporization of the TMS derivatives. Therefore, the method is selective for compounds whose derivatives are low volatile and remain in the particle phase. Alternatively, the method could be adapted to the use of a silylation agent with the tributylsilyl group. Their derivatives are expected to be less volatile due to the higher mass compared to the corresponding TMS derivatives and extend the method to a larger number of aerosol compounds.

In the online silylation of some long-chained test compounds, an increase of the median particle diameter and a decrease of the standard deviation were found when MSTFA was added to the aerosol. The smaller standard deviation indicates a liquefaction of the aerosol including an increased collection efficiency in the AMS. Besides, a higher concentration of TMS derivatives was obtained compared to the concentration of the respective starting materials. This overestimation is explained by the increased collection, transmission or ionization efficiency due to a change of the properties of aggregate state, particle size and volatility.

The new method was also tested for ambient aerosols. Quantitative results of organic alcohols and acids were not obtained due to the low concentration of organic species. However, the temporal course of HMDSO in comparison to the course of the relative humidity indicates that HMDSO was probably formed by the silylation of water in the particles. This water can usually not be detected by the AMS. If the loss of the volatile HMDSO between the flow tube and the ionization source of the AMS can be estimated, water content in the particles will be quantified. Besides the detection of HMDSO, signals of polydimethylsiloxanes were detected during a short period in the outdoor measurement. They are TMS derivatives of silanols which are oxidation products of polydimethylsiloxanes. The possible sources of the latter are solvents, lubricants, penetrating oils, and various personal care products which potentially occur in outdoor and indoor air. In conclusion, despite the lack of organic aerosol components, qualitative information about ambient aerosols was achieved using online silylation.

Finally, as a proof-of-principle study, the results of the online silylation showed that a complete conversion of alcohols and carboxylic acids to the respective TMS derivatives is possible. Further studies should certainly include the use of silylation agents with larger trialkylsilyl groups to avoid the evaporation of the derivatization product from the particle phase. Besides the quantification of the amount of hydroxyl and carboxylic groups, the silylation reaction provides a high capability for structural analysis of the aerosol species due to the characteristic fragmentation pattern.

Summary and Outlook

6 References

- Abramson, E., Imre, D., Beránek, J., Wilson, J., and Zelenyuk, A.: Experimental determination of chemical diffusion within secondary organic aerosol particles, *Physical chemistry chemical physics PCCP*, 15, 2983–2991, doi:10.1039/c2cp44013j, 2013.
- Ahn, K.-H. and Liu, B. Y.H.: Particle activation and droplet growth processes in condensation nucleus counter—I. Theoretical background, *J. Aerosol Sci*, 21, 249–261, doi:10.1016/0021-8502(90)90008-L, 1990.
- Aiken, A. C., DeCarlo, P. F., Kroll, J. H., Worsnop, D. R., Huffman, J. A., Docherty, K. S., Ulbrich, I. M., Mohr, C., Kimmel, J. R., Sueper, D., Sun, Y., Zhang, Q., Trimborn, A., Northway, M., Ziemann, P. J., Canagaratna, M. R., Onasch, T. B., Alfarra, M. R., Prevot, A. S. H., Dommen, J., Duplissy, J., Metzger, A., Baltensperger, U., and Jimenez, J. L.: O/C and OM/OC Ratios of Primary, Secondary, and Ambient Organic Aerosols with High-Resolution Time-of-Flight Aerosol Mass Spectrometry, *Environ. Sci. Technol.*, 42, 4478–4485, doi:10.1021/es703009q, 2008.
- Albrecht, B. A.: *Cloud Microphysics, and Fractional Cloudiness*, Science (New York, N.Y.), 1227–1230, 1989.
- Allan, J. D., Delia, A. E., Coe, H., Bower, K. N., Alfarra, M.R., Jimenez, J. L., Middlebrook, A. M., Drewnick, F., Onasch, T. B., Canagaratna, M. R., Jayne, J. T., and Worsnop, D. R.: A generalised method for the extraction of chemically resolved mass spectra from Aerodyne aerosol mass spectrometer data, *Journal of Aerosol Science*, 35, 909–922, doi:10.1016/j.jaerosci.2004.02.007, 2004.
- Allan, J. D., Jimenez, J. L., Williams, P. I., Alfarra, M. R., Bower, K. N., Jayne, J. T., Coe, H., and Worsnop, D. R.: Quantitative sampling using an Aerodyne aerosol mass spectrometer 1. Techniques of data interpretation and error analysis, *J. Geophys. Res.*, 108, n/a-n/a, doi:10.1029/2002JD002358, 2003.
- Angell, C. A.: *Formation of glasses from liquids and biopolymers*, 1995.
- Atkins, P. and de Paula, J.: *The rates of chemical reactions: Atkins' Physical chemistry*, 8th ed, Freeman, W. H., 791-823, 2006.
- Atkinson, R.: Atmospheric chemistry of VOCs and NO_x, *Atmospheric Environment*, 34, 2063–2101, doi:10.1016/S1352-2310(99)00460-4, 2000.
- Ayres, F. D. and Heather, R. W.: LCQ Deca XP-Plus: Hardware Manual: https://conquerscientific.com/wp-content/ad_images/2014/04/finnigan-lcq-deca-hardware-manual.pdf, last access: 14 February 2020.
- Banerjee, D. K. and Budke, C. C.: Spectrophotometric Determination of Traces of Peroxides in Organic Solvents., *Anal. Chem.*, 36, 792-796, 1964.
- Brinkhorst, J., Nara, S. J., and Pratt, D. A.: Hock cleavage of cholesterol 5 α -hydroperoxide: an ozone-free pathway to the cholesterol ozonolysis products identified in arterial plaque and brain tissue, *Journal of the American Chemical Society*, 130, 12224–12225, doi:10.1021/ja804162d, 2008.
- Brüggemann, M.: *Development, Characterization, and Application of Flowing Atmospheric-Pressure Afterglow Ionization for Mass Spectrometric Analysis of Ambient Organic Aerosols: Dissertation*, Johannes Gutenberg Universität Mainz, 171 pp., 2015.

References

- Brüggemann, M., Karu, E., and Hoffmann, T.: Critical assessment of ionization patterns and applications of ambient desorption/ionization mass spectrometry using FAPA-MS, *Journal of mass spectrometry JMS*, 51, 141–149, doi:10.1002/jms.3733, 2016.
- Brüggemann, M., Karu, E., Stelzer, T., and Hoffmann, T.: Real-Time Analysis of Ambient Organic Aerosols Using Aerosol Flowing Atmospheric-Pressure Afterglow Mass Spectrometry (AeroFAPA-MS), *Environmental science & technology*, 49, 5571–5578, doi:10.1021/es506186c, 2015.
- Canagaratna, M. R., Jayne, J. T., Jimenez, J. L., Allan, J. D., Alfarra, M. R., Zhang, Q., Onasch, T. B., Drewnick, F., Coe, H., Middlebrook, A., Delia, A., Williams, L. R., Trimborn, A. M., Northway, M. J., DeCarlo, P. F., Kolb, C. E., Davidovits, P., and Worsnop, D. R.: Chemical and microphysical characterization of ambient aerosols with the aerodyne aerosol mass spectrometer, *Mass spectrometry reviews*, 26, 185–222, doi:10.1002/mas.20115, 2007.
- Canagaratna, M. R., Jimenez, J. L., Kroll, J. H., Chen, Q., Kessler, S. H., Massoli, P., Hildebrandt Ruiz, L., Fortner, E., Williams, L. R., Wilson, K. R., Surratt, J. D., Donahue, N. M., Jayne, J. T., and Worsnop, D. R.: Elemental ratio measurements of organic compounds using aerosol mass spectrometry: Characterization, improved calibration, and implications, *Atmos. Chem. Phys.*, 15, 253–272, doi:10.5194/acp-15-253-2015, 2015.
- Carroll, D. I., Dzidic, I., Stillwell, R. N., Haegele, K. D., and Horning, E. C.: Atmospheric pressure ionization mass spectrometry. Corona discharge ion source for use in a liquid chromatograph-mass spectrometer-computer analytical system, *Analytical chemistry*, 47, 2369–2373, 1975.
- Chandramouli, B. and Kamens, R. M.: The photochemical formation and gas-particle partitioning of oxidation products of decamethyl cyclopentasiloxane and decamethyl tetrasiloxane in the atmosphere, *Atmospheric Environment*, 35, 87–95, doi:10.1016/S1352-2310(00)00289-2, 2001.
- Chapleski, R. C., Zhang, Y., Troya, D., and Morris, J. R.: Heterogeneous chemistry and reaction dynamics of the atmospheric oxidants, O₃, NO₃, and OH, on organic surfaces, *Chemical Society reviews*, 45, 3731–3746, doi:10.1039/c5cs00375j, 2016.
- Chellamani, A. and Suresh, R.: Kinetics and mechanism of oxidation of triphenylphosphine by hydrogen peroxide, *React. Kinet. Catal. Lett.*, 37, 501–505, 1988.
- Claflin, M. S., Krechmer, J. E., Hu, W., Jimenez, J. L., and Ziemann, P. J.: Functional Group Composition of Secondary Organic Aerosol Formed from Ozonolysis of α -Pinene Under High VOC and Autoxidation Conditions, *ACS Earth Space Chem.*, 2, 1196–1210, doi:10.1021/acsearthspacechem.8b00117, 2018.
- Cocker, D. R., Flagan, R. C., and Seinfeld, J. H.: State-of-the-Art Chamber Facility for Studying Atmospheric Aerosol Chemistry, *Environ. Sci. Technol.*, 35, 2594–2601, doi:10.1021/es0019169, 2001.
- Coggon, M. M., McDonald, B. C., Vlasenko, A., Veres, P. R., Bernard, F., Koss, A. R., Yuan, B., Gilman, J. B., Peischl, J., Aikin, K. C., DuRant, J., Warneke, C., Li, S.-M., and Gouw, J. A. de: Diurnal Variability and Emission Pattern of Decamethylcyclopentasiloxane

References

- (D5) from the Application of Personal Care Products in Two North American Cities, *Environ. Sci. Technol.*, 52, 5610–5618, doi:10.1021/acs.est.8b00506, 2018.
- Crump, J. G. and Seinfeld, J. H.: Turbulent deposition and gravitational sedimentation of an aerosol in a vessel of arbitrary shape, *Journal of Aerosol Science*, 12, 405–415, doi:10.1016/0021-8502(81)90036-7, 1981.
- Czoschke, N.: Effect of acidic seed on biogenic secondary organic aerosol growth, *Atmospheric Environment*, 37, 4287–4299, doi:10.1016/S1352-2310(03)00511-9, 2003.
- Davies, A. G. and Feld, R.: 934. Organic peroxides. Part IX. A stereochemical study of the formation of alkyl hydroperoxides from hydrogen peroxide, *J. Chem. Soc., (Journal of the Chemical Society)*, 4637–4643, 1958.
- de Hoffmann, E. and Stroobant, V.: *Mass Spectrometry Principles and Applications*, 3rd ed., John Wiley & Sons Ltd, Chichester, West Sussex PO19 8SQ, England, 502 pp., 2007.
- Debenedetti, P. G. and Stillinger, F. H.: Supercooled liquids and the glass transition, *Nature*, 410, 259–267, doi:10.1038/35065704, 2001.
- DeCarlo, P. F., Kimmel, J. R., Trimborn, A., Northway, M. J., Jayne, J. T., Aiken, A. C., Gonin, M., Fuhrer, K., Horvath, T., Docherty, K. S., Worsnop, D. R., and Jimenez, J. L.: Field-deployable, high-resolution, time-of-flight aerosol mass spectrometer, *Analytical chemistry*, 78, 8281–8289, doi:10.1021/ac061249n, 2006.
- DeCarlo, P. F., Slowik, J. G., Worsnop, D. R., Davidovits, P., and Jimenez, J. L.: Particle Morphology and Density Characterization by Combined Mobility and Aerodynamic Diameter Measurements. Part 1: Theory, *Aerosol Science and Technology*, 38, 1185–1205, doi:10.1080/027868290903907, 2004.
- Denjean, C., Formenti, P., Picquet-Varrault, B., Pangui, E., Zapf, P., Katrib, Y., Giorio, C., Tapparo, A., Monod, A., Temime-Roussel, B., Decorse, P., Mangeney, C., and Doussin, J. F.: Relating hygroscopicity and optical properties to chemical composition and structure of secondary organic aerosol particles generated from the ozonolysis of α -pinene, *Atmos. Chem. Phys.*, 15, 3339–3358, doi:10.5194/acp-15-3339-2015, 2015.
- Docherty, K. S., Kumboonlert, K., Lee, I. J., and Ziemann, P. J.: Gas chromatography of trimethylsilyl derivatives of α -methoxyalkyl hydroperoxides formed in alkene–O₃ reactions, *Journal of Chromatography A*, 1029, 205–215, doi:10.1016/j.chroma.2003.12.014, 2004.
- Docherty, K. S., Wu, W., Lim, Y. B., and Ziemann, P. J.: Contributions of Organic Peroxides to Secondary Aerosol Formed from Reactions of Monoterpenes with O₃, *Environ. Sci. Technol.*, 39, 4049–4059, doi:10.1021/es050228s, 2005.
- Dockery, D. W., Pope, C. A., Xu, X., Spengler, J. D., Ware, J. H., Fay, M. E., Ferris, B. G. J., and Speizer, F. E.: An Association between Air Pollution and Mortality in Six U.S. Cities, *The new England Journal of Medicine*, 1753–1759, 1993.
- Donahue, N. M., Kroll, J. H., Pandis, S. N., and Robinson, A. L.: A two-dimensional volatility basis set – Part 2: Diagnostics of organic-aerosol evolution, *Atmos. Chem. Phys.*, 12, 615–634, doi:10.5194/acp-12-615-2012, 2012.
- Donahue, N. M., Trump, E. R., Pierce, J. R., and Riipinen, I.: Theoretical constraints on pure vapor-pressure driven condensation of organics to ultrafine particles, *Geophys. Res. Lett.*, 38, n/a-n/a, doi:10.1029/2011GL048115, 2011.

References

- Drewnick, F., Hings, S. S., DeCarlo, P., Jayne, J. T., Gonin, M., Fuhrer, K., Weimer, S., Jimenez, J. L., Demerjian, K. L., Borrmann, S., and Worsnop, D. R.: A New Time-of-Flight Aerosol Mass Spectrometer (TOF-AMS)—Instrument Description and First Field Deployment, *Aerosol Science and Technology*, 39, 637–658, doi:10.1080/02786820500182040, 2005.
- Ehn, M., Kleist, E., Junninen, H., Petäjä, T., Lönn, G., Schobesberger, S., Dal Maso, M., Trimborn, A., Kulmala, M., Worsnop, D. R., Wahner, A., Wildt, J., and Mentel, T. F.: Gas phase formation of extremely oxidized pinene reaction products in chamber and ambient air, *Atmos. Chem. Phys.*, 12, 5113–5127, doi:10.5194/acp-12-5113-2012, 2012.
- Epstein, S. A., Blair, S. L., and Nizkorodov, S. A.: Direct photolysis of α -pinene ozonolysis secondary organic aerosol: Effect on particle mass and peroxide content, *Environmental science & technology*, 48, 11251–11258, doi:10.1021/es502350u, 2014.
- Facchini, M. C., Decesari, S., Mircea, M., Fuzzi, S., and Loglio, G.: Surface tension of atmospheric wet aerosol and cloud/fog droplets in relation to their organic carbon content and chemical composition, *Atmospheric Environment*, 34, 4853–4857, doi:10.1016/S1352-2310(00)00237-5, 2000.
- Faust, B. C., Anastasio, C., Allen, J. M., and Arakaki, T.: Aqueous-phase photochemical formation of peroxides in authentic cloud and fog waters, *Science (New York, N.Y.)*, 73–75, 1993.
- Field Data Analysis Guide: http://cires1.colorado.edu/jimenez-group/wiki/index.php/Field_Data_Analysis_Guide, last access: 7 May 2019.
- Field ToF-AMS Operation: http://cires1.colorado.edu/jimenez-group/wiki/index.php/Field_ToF-AMS_Operation, last access: 27 May 2019.
- Flores, R. M. and Doskey, P. V.: Evaluation of multistep derivatization methods for identification and quantification of oxygenated species in organic aerosol, *J. Chromatogr. A*, 1418, 1–11, doi:10.1016/j.chroma.2015.09.041, 2015.
- Forman, H. J. and Finch, C. E.: A critical review of assays for hazardous components of air pollution, *Free radical biology & medicine*, 117, 202–217, doi:10.1016/j.freeradbiomed.2018.01.030, 2018.
- Franze, T., Weller, M. G., Niessner, R., and Pöschl, U.: Protein Nitration by Polluted Air, *Environ. Sci. Technol.*, 39, 1673–1678, doi:10.1021/es0488737, 2005.
- Freutel, F.: Einzelpartikel- und Ensemblemessungen mit dem Aerosolmassenspektrometer (AMS): Untersuchungen zu Quellen und chemischer Zusammensetzung von Aerosolpartikeln im Submikrometerbereich, doctoral thesis, Johannes Gutenberg-Universität, Mainz, 2012.
- Gong, Y., Chen, Z., and Li, H.: The oxidation regime and SOA composition in limonene ozonolysis: roles of different double bonds, radicals, and water, *Atmos. Chem. Phys.*, 18, 15105–15123, doi:10.5194/acp-18-15105-2018, 2018.
- Gotoh, N., Miyake, S., Takei, H., Sasaki, K., Okuda, S., Ishinaga, M., and Wada, S.: Simple Method for Measuring the Peroxide Value in a Colored Lipid, *Food Anal. Methods*, 4, 525–530, doi:10.1007/s12161-011-9193-5, 2011.
- Guo, J., Tilgner, A., Yeung, C., Wang, Z., Louie, P. K. K., Luk, C. W. Y., Xu, Z., Yuan, C., Gao, Y., Poon, S., Herrmann, H., Lee, S., Lam, K. S., and Wang, T.: Atmospheric peroxides in a polluted subtropical environment: Seasonal variation, sources and sinks, and

References

- importance of heterogeneous processes, *Environmental science & technology*, 48, 1443–1450, doi:10.1021/es403229x, 2014.
- Halket, J. M. and Zaikin, V. G.: Derivatization in mass spectrometry--1. Silylation, *Eur. J. Mass Spectrom.*, 9, 1–21, doi:10.1255/ejms.527, 2003.
- Hall, W. A. and Johnston, M. V.: Oligomer formation pathways in secondary organic aerosol from MS and MS/MS measurements with high mass accuracy and resolving power, *Journal of the American Society for Mass Spectrometry*, 23, 1097–1108, doi:10.1007/s13361-012-0362-6, 2012.
- Hallquist, M., Wenger, J. C., George, C., Goldstein, A. H., Hamilton, J. F., Herrmann, H., Hoffmann, T., Iinuma, Y., Jang, M., Jenkin, M. E., Jimenez, J. L., Kiendler-Scharr, A., Maenhaut, W., McFiggans, G., Mentel, T. F., Monod, A., Prévôt, A. S. H., Seinfeld, J. H., Surratt, J. D., Szmigielski, R., and Wildt, J.: The formation, properties and impact of secondary organic aerosol: current and emerging issues, *Atmos. Chem. Phys.*, 9, 5155–5236, 2009.
- Heim, M., Kasper, G., Reischl, G. P., and Gerhart, C.: Performance of a New Commercial Electrical Mobility Spectrometer, *Aerosol Sci Technol.*, 38, 3–14, doi:10.1080/02786820490519252, 2004.
- High Resolution ToF-AMS Analysis Guide: http://cires1.colorado.edu/jimenez-group/wiki/index.php/High_Resolution_ToF-AMS_Analysis_Guide, last access: 7 May 2019.
- Hinds, W. C.: *Properties, Behavior, and Measurement of airborne particles*, 1999.
- Hings, S. S.: *Characterisation and Field Deployment of a Novel Quantitative Time-of-Flight Aerosol Mass Spectrometer (ToF-AMS)*, doctoral thesis, Johannes Gutenberg-Universität, Mainz, 149 pp., 2006.
- Hoffmann, T., Bandur, R., Marggraf, U., and Linscheid, M.: Molecular composition of organic aerosols formed in the α -pinene/O₃ reaction: Implications for new particle formation processes, *J. Geophys. Res.*, 103, 25569–25578, doi:10.1029/98JD01816, 1998.
- Hoffmann, T., Zetzsch, C., and Rossi, M. J.: *Chemie von Aerosolen*, *Chem. Unserer Zeit*, 41, 232–246, doi:10.1002/ciuz.200700417, 2007.
- Horning, E. C., Horning, M. G., Carroll, D. I., Dzidic, I., and Stillwell, R. N.: New picogram detection system based on a mass spectrometer with an external ionization source at atmospheric pressure, *Anal. Chem.*, 45, 936–943, doi:10.1021/ac60328a035, 1973.
- Hua, W., Chen, Z. M., Jie, C. Y., Kondo, Y., Hofzumahaus, A., Takegawa, N., Lu, K. D., Miyazaki, Y., Kita, K., Wang, H. L., Zhang, Y. H., and Hu, M.: Atmospheric hydrogen peroxide and organic hydroperoxides during PRIDE-PRD'06, China: their concentration, formation mechanism and contribution to secondary aerosols, *Atmos. Chem. Phys. Discuss.*, 8, 10481–10530, doi:10.5194/acpd-8-10481-2008, 2008.
- Huang, D. D., Zhang, X., Dalleska, N. F., Lignell, H., Coggon, M. M., Chan, C.-M., Flagan, R. C., Seinfeld, J. H., and Chan, C. K.: A note on the effects of inorganic seed aerosol on the oxidation state of secondary organic aerosol- α -Pinene ozonolysis, *J. Geophys. Res. Atmos.*, 121, 12,476–12,483, doi:10.1002/2016JD025999, 2016.
- Huffman, J. A., Jayne, J. T., Drewnick, F., Aiken, A. C., Onasch, T., Worsnop, D. R., and Jimenez, J. L.: Design, Modeling, Optimization, and Experimental Tests of a Particle

References

- Beam Width Probe for the Aerodyne Aerosol Mass Spectrometer, *Aerosol Science and Technology*, 39, 1143–1163, doi:10.1080/02786820500423782, 2005.
- Isaacman, G., Kreisberg, N. M., Yee, L. D., Worton, D. R., Chan, A. W. H., Moss, J. A., Hering, S. V., and Goldstein, A. H.: Online derivatization for hourly measurements of gas- and particle-phase semi-volatile oxygenated organic compounds by thermal desorption aerosol gas chromatography (SV-TAG), *Atmos. Meas. Tech.*, 7, 4417–4429, doi:10.5194/amt-7-4417-2014, 2014.
- IUPAC: IUPAC Gold Book, 2014.
- Jackson, A. V. and Hewitt, C. N.: Atmosphere Hydrogen Peroxide and Organic Hydroperoxides: A Review, *Critical Reviews in Environmental Science and Technology*, 175-128, 1999.
- Jaoui, M., Kleindienst, T. E., Lewandowski, M., Offenberg, J. H., and Edney, E. O.: Identification and Quantification of Aerosol Polar Oxygenated Compounds Bearing Carboxylic or Hydroxyl Groups. 2. Organic Tracer Compounds from Monoterpenes, *Environ. Sci. Technol.*, 39, 5661–5673, doi:10.1021/es048111b, 2005.
- Jarvie, A. W.P., Moore, C. G., and Skelton, D.: Reactions of some organic peroxides with triphenylphosphine and sodium dialkyl phosphites, *Journal of Polymer Science: Part A-1*, 9, 3105–3114, 1971.
- Jayanthi, S. and Koshore, K.: Reaction of polyperoxides with triphenylphosphine, *J. Polym. Sci. Pol. Phys (Journal of Polymer Science A: Polymer Chemistry)*, 35, 1167–1172, 1997.
- Jayne, J. T., Leard, D. C., Zhang, X., Davidovits, P., Smith, K. A., Kolb, C. E., and Worsnop, D. R.: Development of an Aerosol Mass Spectrometer for Size and Composition Analysis of Submicron Particles, *Aerosol Science and Technology*, 33, 49–70, doi:10.1080/027868200410840, 2000.
- Jimenez, J. L., Jayne, J. T., Shi, Q., Kolb, C. E., Worsnop, D. R., Yourshaw, I., Seinfeld, J. H., Flagan, R. C., Zhang, X. Z., Smith, K. A., Morris, J. W., and Davidovits, P.: Ambient aerosol sampling using the Aerodyne Aerosol Mass Spectrometer, *J. Geophys. Res.*, 108, 8425–8438, doi:10.1029/2001JD001213, 2003.
- Kanakidou, M., Seinfeld, J. H., Pandis, S. N., Barnes, I., Dentener, F. J., Facchini, M. C., Van Dingenen, R., Ervens, B., Nenes, A., Nielsen, C. J., Swietlicki, E., Putaud, J. P., Balkanski, Y., Fuzzi, S., Horth, J., Moortgat, G. K., Winterhalter, R., Myhre, C. E. L., Tsigaridis, K., Vignati, E., Stephanou, E. G., and Wilson, J.: Organic aerosol and global climate modelling: a review, *Atmos. Chem. Phys.*, 5, 1053–1123, doi:10.5194/acp-51053-2005, 2005.
- Kavouras, I. G.: Particle size distribution of organic primary and secondary aerosol constituents in urban, background marine, and forest atmosphere, *J. Geophys. Res.*, 107, 135, doi:10.1029/2000JD000278, 2002.
- Khan, M.A.H., Cooke, M. C., Utembe, S. R., Xiao, P., Morris, W. C., DERWENT, R. G., Archibald, A. T., Jenkin, M. E., Percival, C. J., and Shallcross, D. E.: The global budgets of organic hydroperoxides for present and pre-industrial scenarios, *Atmospheric Environment*, 110, 65–74, doi:10.1016/j.atmosenv.2015.03.045, 2015.
- Kleeman, M. J., Schauer, J. J., and Cass, G. R.: Size and Composition Distribution of Fine Particulate Matter Emitted from Wood Burning, Meat Charbroiling, and Cigarettes, *Environ. Sci. Technol.*, 33, 3516–3523, doi:10.1021/es981277q, 1999.

References

- Kleindienst, T. E., Shepson, P. B., Hodges, D. N., Nero, C. M., Arnts, R. R., Dasgupta, P. K., Hwang, H., Kok, G. L., Lind, J. A., Lazrus, A. L., Mackay, G. I., Mayne, L. K., and Schiff, H. I.: Comparison of techniques for measurement of ambient levels of hydrogen peroxide, *Environmental science & technology*, 22, 53–61, doi:10.1021/es00166a005, 1988.
- Koch, C. W., Eargle, D. H., and Kenyon, G. L.: Electron impact induced fragmentations and rearrangements of some phenyl substituted phosphine oxides, *Org. Mass Spectrom.*, 12, 624–627, doi:10.1002/oms.1210121005, 1977.
- Köckritz, A. and Martin, A.: Oxidation of unsaturated fatty acid derivatives and vegetable oils, *Eur. J. Lipid Sci. Technol.*, 110, 812–824, doi:10.1002/ejlt.200800042, 2008.
- Köhler, H.: *The nucleus in and the growth of hygroscopic droplets*, 1936.
- Kolb, C. E. and Worsnop, D. R.: Chemistry and composition of atmospheric aerosol particles, *Annual review of physical chemistry*, 63, 471–491, doi:10.1146/annurev-physchem-032511-143706, 2012.
- Koop, T., Bookhold, J., Shiraiwa, M., and Pöschl, U.: Glass transition and phase state of organic compounds: Dependency on molecular properties and implications for secondary organic aerosols in the atmosphere, *Physical chemistry chemical physics PCCP*, 13, 19238–19255, doi:10.1039/c1cp22617g, 2011.
- Krapf, M., El Haddad, I., Bruns, E. A., Molteni, U., Daellenbach, K. R., Prévôt, A. S.H., Baltensperger, U., and Dommen, J.: Labile Peroxides in Secondary Organic Aerosol, *Chem*, 1, 603–616, doi:10.1016/j.chempr.2016.09.007, 2016.
- Kulmala, M.: How Particles Nucleate and Grow, *Science (New York, N.Y.)*, 1000–1001, doi:10.1029/2002JD002180, 2003.
- Kulmala, M., Petäjä, T., Ehn, M., Thornton, J., Sipilä, M., Worsnop, D. R., and Kerminen, V.-M.: Chemistry of atmospheric nucleation: On the recent advances on precursor characterization and atmospheric cluster composition in connection with atmospheric new particle formation, *Annual review of physical chemistry*, 65, 21–37, doi:10.1146/annurev-physchem-040412-110014, 2014.
- Kuwata, M., Zorn, S. R., and Martin, S. T.: Using elemental ratios to predict the density of organic material composed of carbon, hydrogen, and oxygen, *Environ. Sci. Technol.*, 46, 787–794, doi:10.1021/es202525q, 2012.
- Lakey, P. S. J., Berkemeier, T., Tong, H., Arangio, A. M., Lucas, K., Pöschl, U., and Shiraiwa, M.: Chemical exposure-response relationship between air pollutants and reactive oxygen species in the human respiratory tract, *Scientific reports*, 6, 32916, doi:10.1038/srep32916, 2016.
- Lang-Yona, N., Shuster-Meiseles, T., Mazar, Y., Yarden, O., and Rudich, Y.: Impact of urban air pollution on the allergenicity of *Aspergillus fumigatus* conidia: Outdoor exposure study supported by laboratory experiments, *The Science of the total environment*, 541, 365–371, doi:10.1016/j.scitotenv.2015.09.058, 2016.
- Laskin, J., Laskin, A., and Nizkorodov, S. A.: Mass Spectrometry Analysis in Atmospheric Chemistry, *Analytical chemistry*, 90, 166–189, doi:10.1021/acs.analchem.7b04249, 2018.
- Latimer, H. K., Kamens, R. M., and Chandra, G.: The atmospheric partitioning of decamethylcyclopentasiloxane(D5) and 1-hydroxynonamethylcyclopentasiloxane(D4TOH) on different types of

References

- atmospheric particles, *Chemosphere*, 36, 2401–2414, doi:10.1016/S0045-6535(97)10209-0, 1998.
- Lee, H. J. J., Aiona, P. K., Laskin, A., Laskin, J., and Nizkorodov, S. A.: Effect of solar radiation on the optical properties and molecular composition of laboratory proxies of atmospheric brown carbon, *Environmental science & technology*, 48, 10217–10226, doi:10.1021/es502515r, 2014.
- Lercker, G., Bortolomeazzi, R., and Pizzale, L.: Thermal degradation of single methyl oleate hydroperoxides obtained by Photosensitized oxidation, *J Amer Oil Chem Soc*, 75, 1115–1120, doi:10.1007/s11746-998-0299-x, 1998.
- Li, H., Chen, Z., Huang, L., and Huang, D.: Organic peroxides' gas-particle partitioning and rapid heterogeneous decomposition on secondary organic aerosol, *Atmos. Chem. Phys.*, 16, 1837–1848, doi:10.5194/acp-16-1837-2016, 2016a.
- Li, Y.-R., Feng, L.-T., Chen, B.-Y., Kim, H., Yi, S.-M., Guo, Y. L., and Wu, C.-F.: Association of urban particle numbers and sources with lung function among children with asthma or allergies, *The Science of the total environment*, 542, 841–844, doi:10.1016/j.scitotenv.2015.10.098, 2016b.
- Liu, F., Lakey, P. S. J., Berkemeier, T., Tong, H., Kunert, A. T., Meusel, H., Cheng, Y., Su, H., Fröhlich-Nowoisky, J., Lai, S., Weller, M. G., Shiraiwa, M., Pöschl, U., and Kampf, C. J.: Atmospheric protein chemistry influenced by anthropogenic air pollutants: Nitration and oligomerization upon exposure to ozone and nitrogen dioxide, *Faraday discussions*, 200, 413–427, doi:10.1039/c7fd00005g, 2017.
- Liu, P., Ziemann, P. J., Kittelson, D. B., and McMurry, P. H.: Generating Particle Beams of Controlled Dimensions and Divergence: I. Theory of Particle Motion in Aerodynamic Lenses and Nozzle Expansions, *Aerosol Science and Technology*, 22, 293–313, doi:10.1080/02786829408959748, 1995a.
- Liu, P., Ziemann, P. J., Kittelson, D. B., and McMurry, P. H.: Generating Particle Beams of Controlled Dimensions and Divergence: II. Experimental Evaluation of Particle Motion in Aerodynamic Lenses and Nozzle Expansions, *Aerosol Science and Technology*, 22, 314–324, doi:10.1080/02786829408959749, 1995b.
- Martin, S. T.: Phase Transitions of Aqueous Atmospheric Particles, *Chem. Rev.*, 100, 3403–3454, doi:10.1021/cr990034t, 2000.
- Matthew, B. M., Middlebrook, A. M., and Onasch, T. B.: Collection Efficiencies in an Aerodyne Aerosol Mass Spectrometer as a Function of Particle Phase for Laboratory Generated Aerosols, *Aerosol Science and Technology*, 42, 884–898, doi:10.1080/02786820802356797, 2008.
- McDonald, B. C., de Gouw, J. A., Gilman, J. B., Jathar, S. H., Akherati, A., Cappa, C. D., Jiminez, J. J., Lee-Taylor, J., Hayes, P. L., McKeen, S. A., Cui, Y. Y., Kim, S.-W., Gentner, D. R., Isaacman-Van Wertz, G., Goldstein, A. H., Harley, R. A., Frost, G. J., Roberts, J. M., Rynerson, T. B., and Trainer, M.: Volatile chemical products emerging as largest petrochemical source of urban organic emissions, *Science*, 359, 760–764, doi:10.1126/science.aaq0524, 2018.
- McDonald, J. D., Zielinska, B., Fujita, E. M., Sagebiel, J. C., Chow, J. C., and Watson, J. G.: Emissions from Charbroiling and Grilling of Chicken and Beef, *Journal of the Air & Waste Management Association*, 53, 185–194, doi:10.1080/10473289.2003.10466141, 2012.

References

- McNeill, V. F.: Atmospheric Aerosols: Clouds, Chemistry, and Climate, Annual review of chemical and biomolecular engineering, 8, 427–444, doi:10.1146/annurev-chembioeng-060816-101538, 2017.
- Mentel, T. F., Springer, M., Ehn, M., Kleist, E., Pullinen, I., Kurtén, T., Rissanen, M., Wahner, A., and Wildt, J.: Formation of highly oxidized multifunctional compounds: autoxidation of peroxy radicals formed in the ozonolysis of alkenes – deduced from structure–product relationships, Atmos. Chem. Phys., 15, 6745–6765, doi:10.5194/acp-15-6745-2015, 2015.
- Mertes, P., Pfaffenberger, L., Dommen, J., Kalberer, M., and Baltensperger, U.: Development of a sensitive long path absorption photometer to quantify peroxides in aerosol particles (Peroxide-LOPAP), Atmos. Meas. Tech., 5, 2339–2348, doi:10.5194/amt-5-2339-2012, 2012.
- Middlebrook, A. M., Bahreini, R., Jimenez, J. L., and Canagaratna, M. R.: Evaluation of Composition-Dependent Collection Efficiencies for the Aerodyne Aerosol Mass Spectrometer using Field Data, Aerosol Science and Technology, 46, 258–271, doi:10.1080/02786826.2011.620041, 2012.
- Mitchum, R. K. and Korfmacher, W. A.: Atmospheric Pressure Ionization Mass Spectrometry, Anal. Chem., 55, 1485–1499, 1983.
- Mochida, Y. and Nakamura, S.: Determination of Total Hydroperoxides in Oxidized Vegetable Oils Based on Triphenylphosphine Oxidation Using Electron Ionization Mass Spectrometry, J. Mass Spectrom. Soc. Jpn., 54, 235–242, doi:10.5702/masspec.54.235, 2006.
- Murphy, D. M.: The effects of molecular weight and thermal decomposition on the sensitivity of a thermal desorption aerosol mass spectrometer, Aerosol Science and Technology, 50, 118–125, doi:10.1080/02786826.2015.1136403, 2015.
- Mutzel, A., Rodigast, M., Iinuma, Y., Böge, O., and Herrmann, H.: An improved method for the quantification of SOA bound peroxides, Atmospheric Environment, 67, 365–369, doi:10.1016/j.atmosenv.2012.11.012, 2013.
- Myhre, G., Shindell, D., Bréon, F. -M., Collins, W., Fuglestedt, J., Huang, J., Koch, D., Lamarque, J. -F., Lee, D., Mendoza, B., Nakajima, T., Robock, A., Stephens, G., Takemura, T., and Zhang, H.: Anthropogenic and Natural Radiative Forcing: The Physical Science Basis. Contribution of Working Group I to the Fifth Assessment Report of the Intergovernmental Panel on Climate Change, Climate Change 2013, 2013.
- Nah, T., McVay, R. C., Zhang, X., Boyd, C. M., Seinfeld, J. H., and Ng, N. L.: Influence of seed aerosol surface area and oxidation rate on vapor wall deposition and SOA mass yields: A case study with α -pinene ozonolysis, Atmos. Chem. Phys., 16, 9361–9379, doi:10.5194/acp-16-9361-2016, 2016.
- Nakamura, T. and Maeda, H.: A simple assay for lipid hydroperoxides based on triphenylphosphine oxidation and high-performance liquid chromatography, Lipids, 26, 765–768, doi:10.1007/BF02535628, 1991.
- Nolte, C. G., Schauer, J. J., Cass, G. R., and Simoneit, B. R. T.: Trimethylsilyl Derivatives of Organic Compounds in Source Samples and in Atmospheric Fine Particulate Matter, Environ. Sci. Technol., 36, 4273–4281, doi:10.1021/es020518y, 2002.
- Orasche, J., Schnelle-Kreis, J., Abbaszade, G., and Zimmermann, R.: Technical Note: In-situ derivatization thermal desorption GC-TOFMS for direct analysis of particle-

References

- bound non-polar and polar organic species, *Atmos. Chem. Phys.*, 11, 8977–8993, doi:10.5194/acp-11-8977-2011, 2011.
- order of reaction, n: <http://goldbook.iupac.org/html/O/O04322.html>, last access: 10 May 2019.
- Ovadnevaite, J., Ceburnis, D., Martucci, G., Bialek, J., Monahan, C., Rinaldi, M., Facchini, M. C., Berresheim, H., Worsnop, D. R., and O'Dowd, C.: Primary marine organic aerosol: A dichotomy of low hygroscopicity and high CCN activity, *Geophys. Res. Lett.*, 38, n/a-n/a, doi:10.1029/2011GL048869, 2011.
- Ovadnevaite, J., Zuend, A., Laaksonen, A., Sanchez, K. J., Roberts, G., Ceburnis, D., Decesari, S., Rinaldi, M., Hodas, N., Facchini, M. C., Seinfeld, J. H., and O' Dowd, C.: Surface tension prevails over solute effect in organic-influenced cloud droplet activation, *Nature*, 546, 637–641, doi:10.1038/nature22806, 2017.
- Pandis, S.: THE LIFE OF AN ATMOSPHERIC PARTICLE: <https://www.narsto.org/sites/narsto-dev.ornl.gov/files/Ch3813KB.pdf>, last access: 12 September 2018.
- Pierce, J. R., Engelhart, G. J., Hildebrandt, L., Weitkamp, E. A., Pathak, R. K., Donahue, N. M., Robinson, A. L., Adams, P. J., and Pandis, S. N.: Constraining Particle Evolution from Wall Losses, Coagulation, and Condensation-Evaporation in Smog-Chamber Experiments: Optimal Estimation Based on Size Distribution Measurements, *Aerosol Science and Technology*, 42, 1001–1015, doi:10.1080/02786820802389251, 2008.
- Poole, C. F.: Alkylsilyl derivatives for gas chromatography, *J. Chromatogr. A*, 1296, 2–14, doi:10.1016/j.chroma.2013.01.097, 2013.
- Porter, N. A., Logan, J., and Kontoyiannidou, V.: Preparation and purification of arachidonic acid hydroperoxides of biological importance, *J.Org.Chem*, 3177–3181, 1979.
- Pöschl, U.: Atmospheric aerosols: Composition, transformation, climate and health effects, *Angewandte Chemie (International ed. in English)*, 44, 7520–7540, doi:10.1002/anie.200501122, 2005.
- Power, R. M., Simpson, S. H., Reid, J. P., and Hudson, A. J.: The transition from liquid to solid-like behaviour in ultrahigh viscosity aerosol particles, *Chem. Sci.*, 4, 2597, doi:10.1039/c3sc50682g, 2013.
- Pratt, K. A. and Prather, K. A.: Mass spectrometry of atmospheric aerosols--recent developments and applications. Part I: Off-line mass spectrometry techniques, *Mass spectrometry reviews*, 31, 1–16, doi:10.1002/mas.20322, 2012a.
- Pratt, K. A. and Prather, K. A.: Mass spectrometry of atmospheric aerosols--recent developments and applications. Part II: On-line mass spectrometry techniques, *Mass spectrometry reviews*, 31, 17–48, doi:10.1002/mas.20330, 2012b.
- R. A. Stein and Vida. Slawson: Spectrophotometric Hydroperoxide Determination by the Use of Triphenylphosphine., *Analytical chemistry*, 1008-1010, 1963.
- Reinmuth-Selzle, K., Ackaert, C., Kampf, C. J., Samonig, M., Shiraiwa, M., Kofler, S., Yang, H., Gadermaier, G., Brandstetter, H., Huber, C. G., Duschl, A., Oostingh, G. J., and Pöschl, U.: Nitration of the birch pollen allergen Bet v 1.0101: Efficiency and site-selectivity of liquid and gaseous nitrating agents, *Journal of proteome research*, 13, 1570–1577, doi:10.1021/pr401078h, 2014.

References

- Reinnig, M.-C., Müller, L., Warnke, J., and Hoffmann, T.: Characterization of selected organic compound classes in secondary organic aerosol from biogenic VOCs by HPLC/MSn, *Analytical and bioanalytical chemistry*, 391, 171–182, doi:10.1007/s00216-008-1964-5, 2008.
- Reinnig, M.-C., Warnke, J., and Hoffmann, T.: Identification of organic hydroperoxides and hydroperoxy acids in secondary organic aerosol formed during the ozonolysis of different monoterpenes and sesquiterpenes by on-line analysis using atmospheric pressure chemical ionization ion trap mass spectrometry, *Rapid communications in mass spectrometry RCM*, 23, 1735–1741, doi:10.1002/rcm.4065, 2009.
- Rissanen, M. P., Kurtén, T., Sipilä, M., Thornton, J. A., Kangasluoma, J., Sarnela, N., Junninen, H., Jørgensen, S., Schallhart, S., Kajos, M. K., Taipale, R., Springer, M., Mentel, T. F., Ruuskanen, T., Petäjä, T., Worsnop, D. R., Kjaergaard, H. G., and Ehn, M.: The formation of highly oxidized multifunctional products in the ozonolysis of cyclohexene, *Journal of the American Chemical Society*, 136, 15596–15606, doi:10.1021/ja507146s, 2014.
- Riva, M.: Multiphase Chemistry of Highly Oxidized Molecules: The Case of Organic Hydroperoxides, *Chem*, 1, 526–528, doi:10.1016/j.chempr.2016.09.015, 2016.
- Riva, M., Budisulistiorini, S. H., Zhang, Z., Gold, A., Thornton, J. A., Turpin, B. J., and Surratt, J. D.: Multiphase reactivity of gaseous hydroperoxide oligomers produced from isoprene ozonolysis in the presence of acidified aerosols, *Atmospheric Environment*, 152, 314–322, doi:10.1016/j.atmosenv.2016.12.040, 2017.
- Rogge, W. F., Hildemann, L. M., Mazurek, M. A., Cass, G. R., and Simoneit, B. R. T.: Sources of fine organic aerosol. 1. Charbroilers and meat cooking operations, *Environ. Sci. Technol.*, 25, 1112–1125, doi:10.1021/es00018a015, 1991.
- Rohling, O. and Neidhart, B.: Application of the denuder technique in filter sampling of airborne chromates at ground level concentrations, *Fresenius J. Anal. Chem.*, 351, 33–40, doi:10.1007/BF00324289, 1995.
- Rontani, J.-F. and Aubert, C.: Trimethylsilyl transfer during electron ionization mass spectral fragmentation of some omega-hydroxycarboxylic and omega-dicarboxylic acid trimethylsilyl derivatives and the effect of chain length, *Rapid Commun. Mass Spectrom.*, 18, 1889–1895, doi:10.1002/rcm.1567, 2004.
- Ruehl, C. R., Chuang, P. Y., Nenes, A., Cappa, C. D., Kolesar, K. R., and Goldstein, A. H.: Strong evidence of surface tension reduction in microscopic aqueous droplets, *Geophys. Res. Lett.*, 39, n/a-n/a, doi:10.1029/2012GL053706, 2012.
- Ruiz, A., Canada, M. J.A., and Lendl, B.: A rapid method for peroxide value determination in edible oils based on flow analysis with Fourier transform infrared spectroscopic detection, *Analyst*, 126, 242–246, doi:10.1039/b008688f, 2001.
- Sadezky, A., Chaimbault, P., Mellouki, A., Römpf, A., Winterhalter, R., Le Bras, G., and Moortgat, G. K.: Formation of secondary organic aerosol and oligomers from the ozonolysis of enol ethers, *Atmos. Chem. Phys. Discuss.*, 6, 5629–5670, doi:10.5194/acpd-6-5629-2006, 2006.
- Sareen, N., Moussa, S. G., and McNeill, V. F.: Photochemical aging of light-absorbing secondary organic aerosol material, *The journal of physical chemistry. A*, 117, 2987–2996, doi:10.1021/jp309413j, 2013.

References

- Schauer, J. J., Kleeman, M. J., Cass, G. R., and Simoneit, B. R. T.: Measurement of Emissions from Air Pollution Sources. 5. C 1 –C 32 Organic Compounds from Gasoline-Powered Motor Vehicles, *Environ. Sci. Technol.*, 36, 1169–1180, doi:10.1021/es0108077, 2002.
- Schroth, T.: New HEPA/ULPA Filters for Clean-Room Technology, *Filtration and Separation*, 33, 245–250, doi:10.1016/S0015-1882(97)84285-1, 1996.
- Schwier, A., Mitroo, D., and McNeill, V. F.: Surface tension depression by low-solubility organic material in aqueous aerosol mimics, *Atmospheric Environment*, 54, 490–495, doi:10.1016/j.atmosenv.2012.02.032, 2012.
- Seinfeld, J. H. and Pandis, S. N.: *Atmospheric chemistry and physics: from air pollution to climate change*, Wiley, New York, 1998.
- Sekimoto, K. and Takayama, M.: Observations of different core water cluster ions Y-(H₂O)_n (Y = O₂, HO_x, NO_x, CO_x) and magic number in atmospheric pressure negative corona discharge mass spectrometry, *Journal of mass spectrometry JMS*, 46, 50–60, doi:10.1002/jms.1870, 2011.
- Shelley, J. T., Wiley, J. S., and Hieftje, G. M.: Ultrasensitive ambient mass spectrometric analysis with a pin-to-capillary flowing atmospheric-pressure afterglow source, *Analytical chemistry*, 83, 5741–5748, doi:10.1021/ac201053q, 2011.
- Shiraiwa, M., Ammann, M., Koop, T., and Pöschl, U.: Gas uptake and chemical aging of semisolid organic aerosol particles, *Proceedings of the National Academy of Sciences of the United States of America*, 108, 11003–11008, doi:10.1073/pnas.1103045108, 2011.
- Sinclair, D. and La Mer, V. K.: Light Scattering as a Measure of Particle Size in Aerosols. The Production of Monodisperse Aerosols., *Chem. Rev.*, 2, 245–267, 1949.
- Skoog, D. A. and Leary, J. J.: *Instrumentelle Analytik: Grundlagen Geräte Anwendungen*, Springer-Verlag Berlin Heidelberg New York, 1996.
- Slowik, J. G., Stainken, K., Davidovits, P., Williams, L. R., Jayne, J. T., Kolb, C. E., Worsnop, D. R., Rudich, Y., DeCarlo, P. F., and Jimenez, J. L.: Particle Morphology and Density Characterization by Combined Mobility and Aerodynamic Diameter Measurements. Part 2: Application to Combustion-Generated Soot Aerosols as a Function of Fuel Equivalence Ratio, *Aerosol Science and Technology*, 38, 1206–1222, doi:10.1080/027868290903916, 2004.
- Smith, M. L., Kuwata, M., and Martin, S. T.: Secondary Organic Material Produced by the Dark Ozonolysis of α -Pinene Minimally Affects the Deliquescence and Efflorescence of Ammonium Sulfate, *Aerosol Science and Technology*, 45, 244–261, doi:10.1080/02786826.2010.532178, 2011.
- Stafford, G. C., Kelley, P. E., Syka, J.E.P., Reynolds, W. E., and Todd, J.F.J.: Recent improvements in and analytical applications of advanced ion trap technology, *International Journal of Mass Spectrometry and Ion Processes*, 60, 85–98, doi:10.1016/0168-1176(84)80077-4, 1984.
- Steiner, G., Attoui, M., Wimmer, D., and Reischl, G. P.: A Medium Flow, High-Resolution Vienna DMA Running in Recirculating Mode, *Aerosol Sci Technol.*, 44, 308–315, doi:10.1080/02786821003636763, 2010.
- Stolzenburg, M. R. and McMurry, P. H.: An Ultrafine Aerosol Condensation Nucleus Counter, *Aerosol Sci Technol.*, 14, 48–65, doi:10.1080/02786829108959470, 1991.

References

- Surratt, J. D., Chan, A. W. H., Eddingsaas, N. C., Chan, M., Loza, C. L., Kwan, A. J., Hersey, S. P., Flagan, R. C., Wennberg, P. O., and Seinfeld, J. H.: Reactive intermediates revealed in secondary organic aerosol formation from isoprene, *Proceedings of the National Academy of Sciences of the United States of America*, 107, 6640–6645, doi:10.1073/pnas.0911114107, 2010.
- Surratt, J. D., Murphy, S. M., Kroll, J. H., Ng, N. L., Hildebrandt, L., Sorooshian, A., Szmigielski, R., Vermeylen, R., Maenhaut, W., Claeys, M., Flagan, R. C., and Seinfeld, J. H.: Chemical composition of secondary organic aerosol formed from the photooxidation of isoprene, *The journal of physical chemistry. A*, 110, 9665–9690, doi:10.1021/jp061734m, 2006.
- Szymanski, W. W.: Aerosol concentration measurement with multiple light scattering system and laser aerosol spectrometer, *Atmos. Res.*, 62, 255–265, doi:10.1016/S0169-8095(02)00013-3, 2002.
- Thorenz, U. R., Kundel, M., Müller, L., and Hoffmann, T.: Generation of standard gas mixtures of halogenated, aliphatic, and aromatic compounds and prediction of the individual output rates based on molecular formula and boiling point, *Analytical and bioanalytical chemistry*, 404, 2177–2183, doi:10.1007/s00216-012-6202-5, 2012.
- Timko, M. T., Yu, Z., Kroll, J., Jayne, J. T., Worsnop, D. R., Miake-Lye, R. C., Onasch, T. B., Liscinsky, D., Kirchstetter, T. W., Destailats, H., Holder, A. L., Smith, J. D., and Wilson, K. R.: Sampling Artifacts from Conductive Silicone Tubing, *Aerosol Science and Technology*, 43, 855–865, doi:10.1080/02786820902984811, 2009.
- Tinoco, I., Sauer, K., and Wang, J. C.: *Physical chemistry: Principles and applications in biological sciences*, 3rd edition, Prentice-Hall, Upper Saddle River, xi761, 1995.
- Tomaz, S., Jaffrezo, J.-L., Favez, O., Perraudin, E., Villenave, E., and Albinet, A.: Sources and atmospheric chemistry of oxy- and nitro-PAHs in the ambient air of Grenoble (France), *Atmospheric Environment*, 161, 144–154, doi:10.1016/j.atmosenv.2017.04.042, 2017.
- Tong, H., Arangio, A. M., Lakey, P. S. J., Berkemeier, T., Liu, F., Kampf, C. J., Brune, W. H., Pöschl, U., and Shiraiwa, M.: Hydroxyl radicals from secondary organic aerosol decomposition in water, *Atmos. Chem. Phys.*, 16, 1761–1771, doi:10.5194/acp-16-1761-2016, 2016.
- Tong, H., Lakey, P. S. J., Arangio, A. M., Socorro, J., Kampf, C. J., Berkemeier, T., Brune, W. H., Pöschl, U., and Shiraiwa, M.: Reactive oxygen species formed in aqueous mixtures of secondary organic aerosols and mineral dust influencing cloud chemistry and public health in the Anthropocene, *Faraday discussions*, 200, 251–270, doi:10.1039/c7fd00023e, 2017.
- TSI: Model 3076 Constant Output Atomizer: <http://www.wmo-gaw-wcc-aerosol-physics.org/files/Atomizer-TSI-3076.pdf>, last access: 29 November 2018.
- Tu, P., Hall, W. A., and Johnston, M. V.: Characterization of Highly Oxidized Molecules in Fresh and Aged Biogenic Secondary Organic Aerosol, *Analytical chemistry*, 88, 4495–4501, doi:10.1021/acs.analchem.6b00378, 2016.
- Twomey, S.: The influence of pollution on the shortwave albedo of clouds, *J. Atmospheric Sci. (Journal of Atmospheric Sciences)*, 1977.

References

- Urbach, D.: MSTFA und MSTFA-D9 – unverzichtbare Werkzeuge für die massenspektrometrische Strukturaufklärung, *Toxichem. Krimtech.*, 79, 137-146, 2012.
- Varutbangkul, V., Brechtel, F. J., Bahreini, R., Ng, N. L., Keywood, M. D., Kroll, J. H., Flagan, R. C., Seinfeld, J. H., Lee, A., and Goldstein, A. H.: Hygroscopicity of secondary organic aerosols formed by oxidation of cycloalkenes, monoterpenes, sesquiterpenes, and related compounds, *Atmos. Chem. Phys. Discuss.*, 6, 1121–1177, doi:10.5194/acpd-6-1121-2006, 2006.
- Virtanen, A., Joutsensaari, J., Koop, T., Kannosto, J., Yli-Pirilä, P., Leskinen, J., Mäkelä, J. M., Holopainen, J. K., Pöschl, U., Kulmala, M., Worsnop, D. R., and Laaksonen, A.: An amorphous solid state of biogenic secondary organic aerosol particles, *Nature*, 467, 824–827, doi:10.1038/nature09455, 2010.
- Vogel, A.: Complementary mass spectrometric techniques for the characterization of the organic fraction in atmospheric aerosols, doctoral thesis, Johannes Gutenberg Universität Mainz, Mainz, 161 pp., 2014.
- Wang, N., Ma, T., Yu, X., Xu, L., and Zhang, R.: Determination of Peroxide Values of Edible Oils by Ultraviolet Spectrometric Method, *Food Anal. Methods*, 9, 1412–1417, doi:10.1007/s12161-015-0322-4, 2016.
- Warscheid, B. and Hoffmann, T.: Structural elucidation of monoterpene oxidation products by ion trap fragmentation using on-line atmospheric pressure chemical ionisation mass spectrometry in the negative ion mode, *Rapid communications in mass spectrometry RCM*, 15, 2259–2272, doi:10.1002/rcm.504, 2001.
- Washenfelder, R. A., Roehl, C. M., McKinney, K. A., Julian, R. R., and Wennberg, P. O.: A compact, lightweight gas standards generator for permeation tubes, *Review of Scientific Instruments*, 74, 3151–3154, doi:10.1063/1.1570949, 2003.
- Williams, D. H., Ward, R. S., and Cooks, R. G.: Mass spectrometry. XXIV. A study of the reactions induced in triphenylphosphine, triphenylphosphine oxide, and related substances upon electron impact, *J. Am. Chem. Soc.*, 90, 966–972, doi:10.1021/ja01006a021, 1968.
- Winkler, P. M., Ortega, J., Karl, T., Cappellin, L., Friedli, H. R., Barsanti, K., McMurry, P. H., and Smith, J. N.: Identification of the biogenic compounds responsible for size-dependent nanoparticle growth, *Geophys. Res. Lett.*, 39, 863, doi:10.1029/2012GL053253, 2012.
- Wu, Y. and Johnston, M. V.: Molecular Characterization of Secondary Aerosol from Oxidation of Cyclic Methylsiloxanes, *J. Am. Soc. Mass Spectrom.*, 27, 402–409, doi:10.1007/s13361-015-1300-1, 2016.
- Yaremenko, I. A., Vil', V. A., Demchuk, D. V., and Terent'ev, A. O.: Rearrangements of organic peroxides and related processes, *Beilstein journal of organic chemistry*, 12, 1647–1748, doi:10.3762/bjoc.12.162, 2016.
- Ye, J., Abbatt, J. P. D., and Chan, A. W. H.: Novel pathway of SO₂ oxidation in the atmosphere: Reactions with monoterpene ozonolysis intermediates and secondary organic aerosol, *Atmos. Chem. Phys.*, 18, 5549–5565, doi:10.5194/acp-18-5549-2018, 2018.
- Yoshinari, K.: Theoretical and numerical analysis of the behavior of ions injected into a quadrupole ion trap mass spectrometer, *Rapid Commun. Mass Spectrom.*, 14,

References

- 215–223, doi:10.1002/(SICI)1097-0231(20000229)14:4<215:AID-RCM867>3.0.CO;2-T, 2000.
- Yu, Y., Liz Alexander, M., Perraud, V., Bruns, E. A., Johnson, S. N., Ezell, M. J., and Finlayson-Pitts, B. J.: Contamination from electrically conductive silicone tubing during aerosol chemical analysis, *Atmospheric Environment*, 43, 2836–2839, doi:10.1016/j.atmosenv.2009.02.014, 2009.
- Zelenyuk, A., Cai, Y., and Imre, D.: From Agglomerates of Spheres to Irregularly Shaped Particles: Determination of Dynamic Shape Factors from Measurements of Mobility and Vacuum Aerodynamic Diameters, *Aerosol Science and Technology*, 40, 197–217, doi:10.1080/02786820500529406, 2006.
- Zelenyuk, A., Imre, D., Beránek, J., Abramson, E., Wilson, J., and Shrivastava, M.: Synergy between secondary organic aerosols and long-range transport of polycyclic aromatic hydrocarbons, *Environmental science & technology*, 46, 12459–12466, doi:10.1021/es302743z, 2012.
- Zelenyuk, A., Yang, J., Song, C., Zaveri, R. A., and Imre, D.: A New Real-Time Method for Determining Particles' Sphericity and Density: Application to Secondary Organic Aerosol Formed by Ozonolysis of α -Pinene, *Environ. Sci. Technol.*, 42, 8033–8038, doi:10.1021/es8013562, 2008.
- Zhang, Q., Alfarra, M. R., Worsnop, D. R., Allan, J. D., Coe, H., Canagaratna, M. R., and Jimenez, J. L.: Deconvolution and quantification of hydrocarbon-like and oxygenated organic aerosols based on aerosol mass spectrometry, *Environmental science & technology*, 39, 4938–4952, doi:10.1021/es048568l, 2005.
- Zhang, X., Lambe, A. T., Upshur, M. A., Brooks, W. A., Gray Bé, A., Thomson, R. J., Geiger, F. M., Surratt, J. D., Zhang, Z., Gold, A., Graf, S., Cubison, M. J., Groessl, M., Jayne, J. T., Worsnop, D. R., and Canagaratna, M. R.: Highly Oxygenated Multifunctional Compounds in α -Pinene Secondary Organic Aerosol, *Environmental science & technology*, 51, 5932–5940, doi:10.1021/acs.est.6b06588, 2017.
- Zhang, X., Schwantes, R. H., McVay, R. C., Lignell, H., Coggon, M. M., Flagan, R. C., and Seinfeld, J. H.: Vapor wall deposition in Teflon chambers, *Atmos. Chem. Phys.*, 15, 4197–4214, doi:10.5194/acp-15-4197-2015, 2015.
- Zhang, X., Smith, K. A., Worsnop, D. R., Jimenez, J. L., Jayne, J. T., Kolb, C. E., Morris, J., and Davidovits, P.: Numerical Characterization of Particle Beam Collimation: Part II Integrated Aerodynamic-Lens–Nozzle System, *Aerosol Science and Technology*, 38, 619–638, doi:10.1080/02786820490479833, 2004.
- Zhang, X., Smith, K. A., Worsnop, D. R., Jimenez, J., Jayne, J. T., and Kolb, C. E.: A Numerical Characterization of Particle Beam Collimation by an Aerodynamic Lens–Nozzle System: Part I. An Individual Lens or Nozzle, *Aerosol Science and Technology*, 36, 617–631, 2002.
- Zhao, J., Ortega, J., Chen, M., McMurry, P. H., and Smith, J. N.: Dependence of particle nucleation and growth on high-molecular-weight gas-phase products during ozonolysis of α -pinene, *Atmos. Chem. Phys.*, 13, 7631–7644, doi:10.5194/acp-13-7631-2013, 2013a.
- Zhao, R., Kenseth, C. M., Huang, Y., Dalleska, N. F., and Seinfeld, J. H.: Iodometry-Assisted Liquid Chromatography Electrospray Ionization Mass Spectrometry for Analysis of Organic Peroxides: An Application to Atmospheric Secondary Organic

References

- Aerosol, Environmental science & technology, 52, 2108–2117, doi:10.1021/acs.est.7b04863, 2018.
- Zhao, R., Lee, A. K. Y., Soong, R., Simpson, A. J., and Abbatt, J. P. D.: Formation of aqueous-phase α -hydroxyhydroperoxides (α -HHP): Potential atmospheric impacts, Atmos. Chem. Phys., 13, 5857–5872, doi:10.5194/acp-13-5857-2013, 2013b.
- Zhao, R., Lee, A. K.Y., Huang, L., Li, X., Yang, F., and Abbatt, J. P.D.: Photochemical processing of aqueous atmospheric brown carbon, Atmos. Chem. Phys., 6087–6100, 2015.
- Zheng, M., Zhao, X., Cheng, Y., Yan, C., Shi, W., Zhang, X., Weber, R. J., Schauer, J. J., Wang, X., and Edgerton, E. S.: Sources of primary and secondary organic aerosol and their diurnal variations, Journal of hazardous materials, 264, 536–544, doi:10.1016/j.jhazmat.2013.10.047, 2014.
- Zhou, S., Rivera-Rios, J. C., Keutsch, F. N., and Abbatt, J. P. D.: Identification of organic hydroperoxides and peroxy acids using atmospheric pressure chemical ionization–tandem mass spectrometry (APCI-MS/MS): Application to secondary organic aerosol, Atmos. Meas. Tech., 11, 3081–3089, doi:10.5194/amt-11-3081-2018, 2018.
- Ziemann, P. J.: Formation of Alkoxyhydroperoxy Aldehydes and Cyclic Peroxyhemiacetals from Reactions of Cyclic Alkenes with O₃ in the Presence of Alcohols, J. Phys. Chem. A, 107, 2048–2060, doi:10.1021/jp022114y, 2003.

References

7 Appendix

7.1 Supplement to section 3.2.

7.1.1 Calibration setup

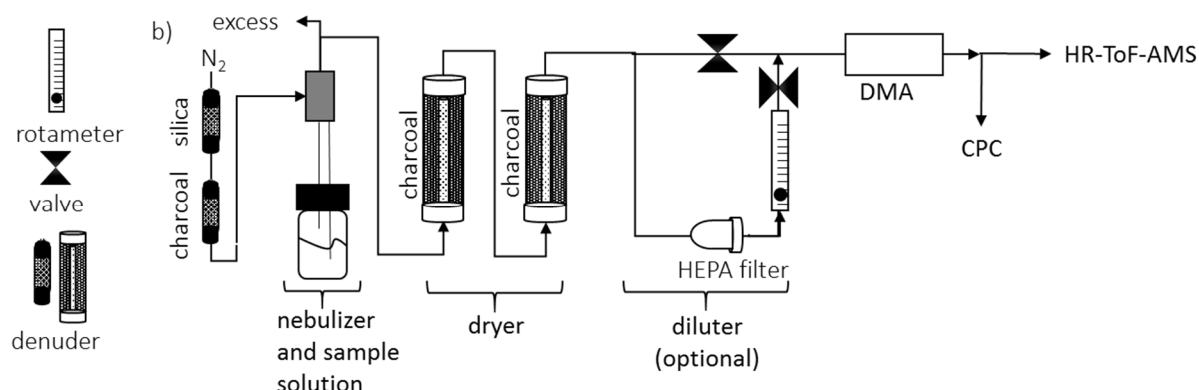


Figure 39: Schematic setup for the calibration of the AMS.

Figure 39 illustrates the typical setup for the calibration of the AMS for a compound using tandem DMA-AMS/CPC (Slowik et al., 2004). A binary solution of the compounds is nebulized (Modell 3076, TSI, Shoreview, MN, USA) to a polydisperse aerosol. The solvent is removed by charcoal denuders (inner tube: diameter = 2 cm, length 40 cm, outer tube: diameter 13.5 cm, length 40 cm) and the aerosol concentration is set using a lab-built diluter. A monodisperse aerosol is obtained by selecting mobility diameter using the DMA and supplied to the HR-ToF-AMS and CPC.

7.1.2 Calibration method

The mass concentration c_m of a single compound is calculated by the AMS according to Canagaratna et al. (2007):

$$c_m(\text{compound}) = \frac{10^{12} \cdot MW(\text{compound})}{IE(\text{compound}) \cdot Q \cdot N_A} \cdot \sum_{\text{all}, i} I(\text{compound}, i), \quad \text{Eq. 55}$$

where MW and IE are the molar weight and the ionization efficiency of a compound, respectively. The ionization efficiency is defined as the total ion rate of all detected ions per vaporized and ionized molecules of one compound. Q is the AMS flow rate, N_A Avogadro's number and 10^{12} a conversion factor to $\mu\text{g}/\text{m}^3$. $I(\text{compound}, i)$ is the ion rate of an ion i formed at the ionization and fragmentation of a compound. Since the fragmentation pattern can be assumed to be robust, it is possible to use the ion yield of a single ion to calculate the concentration. The concentration of TPPO can be calculated as:

$$c_n(\text{detected TPPO}) = \frac{10^{12}}{\frac{IE}{AB} \left(\text{TPPO}, \frac{m}{z} 277 \right) \cdot AB \cdot Q \cdot N_A} \cdot I\left(\frac{m}{z} 277\right) \quad \text{Eq. 56}$$

IE is calculated using Eq. 57:

$$IE = \frac{IPP}{MPP} \quad \text{Eq. 57}$$

IPP is the number of detected ions per particle and MPP the number of molecules per particle. To obtain IPP , it is important to adjust the particle concentration, measured by the AMS below 500 particles/cm³ to be sure that only ions of single particles are detected in the BFSP mode of the AMS. MPP is calculated using Eq. 58.

$$MPP = \frac{S \cdot \rho_p \cdot \frac{4}{3} \cdot \pi \cdot \left(\frac{d_m}{2}\right)^3}{MW} \quad \text{Eq. 58}$$

S is the Jayne shape factor which corrects the deviation from a sphere volume, ρ_p is the particle density which is identical to the material density ρ_m for a full sphere, d_m is the electrical mobility diameter which can be set by the DMA. MW is the molecular weight. S can be obtained using Eq. 59:

$$S = \frac{\rho_m \cdot d_{va}}{\rho_0 \cdot d_m} \quad \text{Eq. 59}$$

ρ_0 is the standard density of spherical particles of 1 g/cm³ and d_{va} the vacuum aerodynamic diameter, obtained by the PToF mode of the AMS. (DeCarlo et al., 2004)

Alternatively, IE can be determined by the MS/CPC method. Here, the particle concentration measured by the CPC has to be included. For the IE determination, the detected particles must contain only the compound to be calibrated.

7.1.3 Result of the calibration

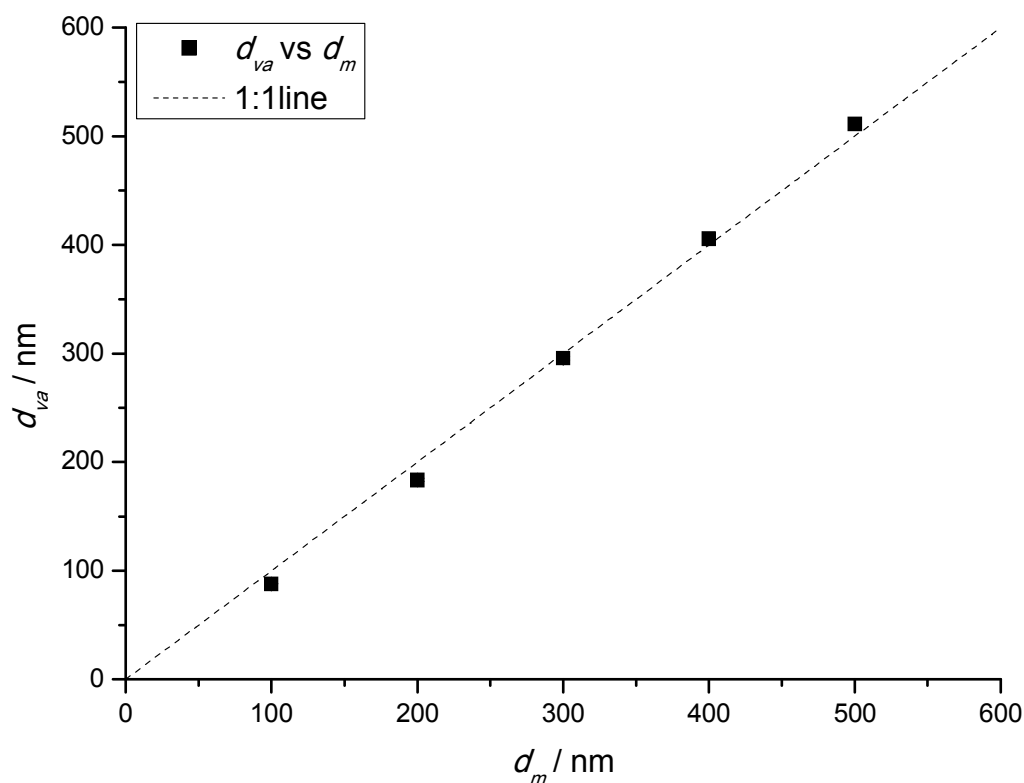


Figure 40: Determination of Jayne shape factor S for TPP0.

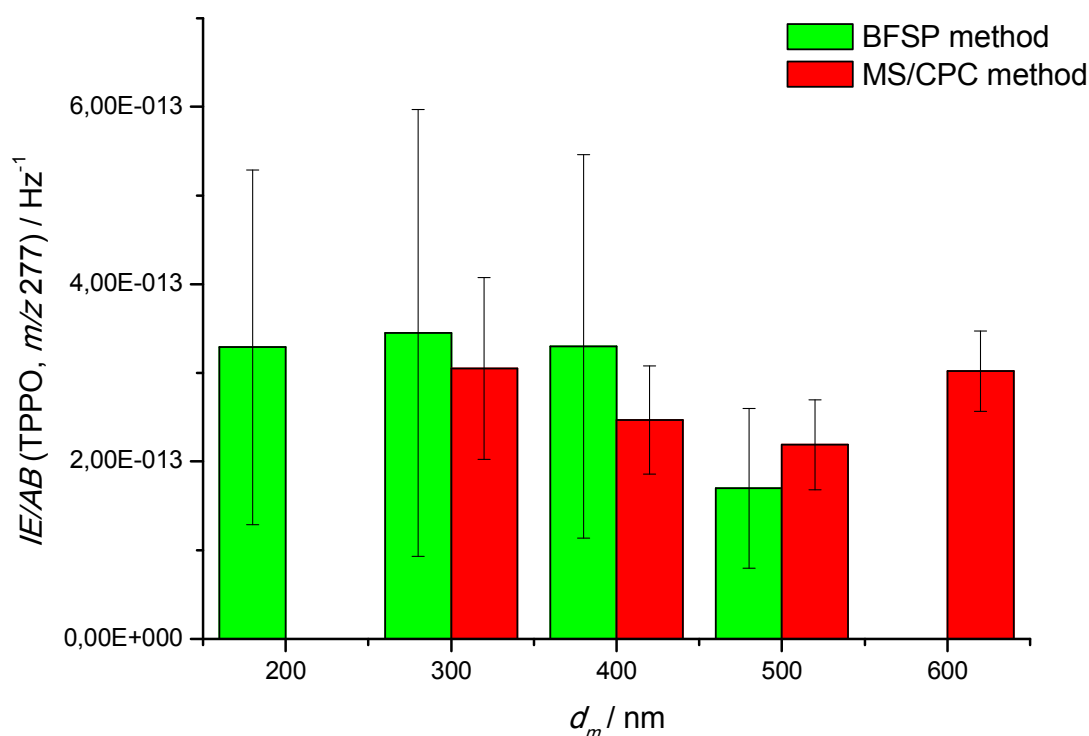


Figure 41: Results from the IE calibration of TPPO using the BFSP method (green) and MS/CPC method (red).

In Figure 40, the vacuum aerodynamic diameter d_{va} is plotted against the electrical mobility diameter d_m . The nearly 1:1 relation of the two diameters indicates spherical particle shape. Using a material density ρ_m of 1.2 g/mL in Eq. 59, the Jayne shape factor S is 0.80 (+/- 0.05).

Figure 41 illustrates the results from the IE calibration of TPPO using the BFSP and the MS/CPC method. The average ionization efficiency IE , normalized to the airbeam AB at the calibration, of the ion rate at m/z 277 of TPPO is IE/AB (TPPO, m/z 277) = $2.61 \cdot 10^{-13} \text{ Hz}^{-1}$. At the calibration of TPP, the Jayne shape factor is $S = 0.72$ and the AB normalized IE at m/z 262 is IE/AB (TPP, m/z 262) = $2.01 \cdot 10^{-13} \text{ Hz}^{-1}$.

7.1.4 TPPO background

Table 6: Background contribution of TPPO on detected TPP, obtained at several SOA-seed aerosol experiments.

Experiment	Background value BV /%	
	$BV = c(\text{detected TPPO})/c(\text{detected TPP})$	
	Average	Standard deviation
1	1.307	0.121
2	1.076	0.071
3	1.124	0.012
4	1.269	0.094
5	1.337	0.036
Average	1.222	
Standard deviation	0.103	
Detection limit	1.530	
Quantification limit	2.250	

Table 6 shows the TPPO background per detected TPP from several SOA seed experiments. Therefore, ammonium sulfate (AS) seed particles were introduced into the chamber and further supplied to the ORD-AMS setup, where TPP condensed on the AS particles. The ratio of the TPPO background concentration to the detected TPP concentration was determined for the periods before the ozonolysis had been started, when either the terpene or ozone was added to the chamber. An average value and standard deviation were obtained from the results of several experiments and used for background correction. Limits of detection and quantification were obtained from this average value.

7.1.5 Calculation of the SOA concentration

Since the mass concentration of SOA $c_m(\text{SOA})$ cannot be measured in the ORD-AMS mode, it was calculated from the particle mass concentration $c_m(\text{particle, SMPS})$, given by the SMPS, and the ammonium sulfate mass concentration using the following equation:

$$c_m(\text{SOA}) = c_m(\text{particle, SMPS}) - c_m(\text{NH}_4\text{SO}_4, \text{AMS}) \quad \text{Eq. 60}$$

As the AMS measured at a time resolution of 120 s and the SMPS a resolution of 200 s, the data points were averaged to a resolution of 600 s (10 min).

Principally, the density ρ of the aerosol is needed to determine the particle mass concentration, given by the SMPS. The density was determined as follow:

The ozonolysis experiments can be divided into two periods. In the first one, only seed particles of ammonium sulfate and one of the reactants (terpene or ozone) were supplied into the chamber. Therefore, only ammonium sulfate particles were introduced into the ORD-setup, which why a density of 1.77 g/cm^3 (material density of ammonium sulfate) was assumed for this period.

The second period started with the addition of the second reactant and the SOA formation. Here, a mixture of ammonium sulfate and SOA were expected and the density ρ was calculated using the parameterization from O/C and H/C ratios according to (Kuwata et al., 2012).

$$\rho = \left[12 + 1 \cdot \frac{H}{C} + 16 \cdot \frac{O}{C} \right] / \left[7.0 + 5.0 \cdot \frac{H}{C} + 4.15 \cdot \frac{O}{C} \right] \quad \text{Eq. 61}$$

The H/C and O/C ratios were calculated in the AMS mode at the end of the respective experiment. The results are given in Table 7. The resulting densities was applied for the whole period after the start of the ozonolysis.

Table 7: Obtained H/C, O/C according to Kuwata et al. (2012) and resulting density for the period during the ozonolysis

Terpene	H/C	O/C	$\rho / \text{g cm}^{-3}$
α -pinene	1.64	0.41	1.19
β -pinene	1.47	0.40	1.24

Appendix

In the end, the molar SOA concentration $c_n(\text{SOA})$ was calculated assuming a molar mass of 250 g/mol using:

$$c_n(\text{SOA}) = \frac{c_m(\text{SOA})}{250 \text{ g/mol}} \quad \text{Eq. 62}$$

7.1.6 Size distribution at SOA experiments

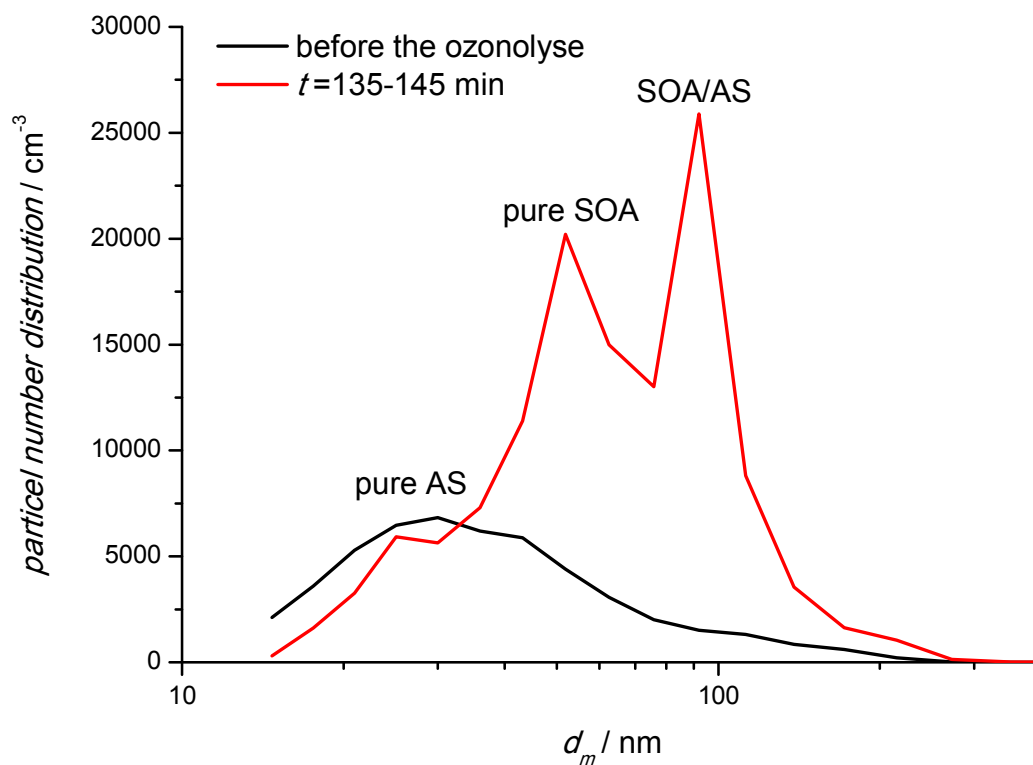


Figure 42: Size distribution of the number concentration before the ozonolysis (black) and in the first 10 min ($t = 135-145$ min) of the ozonolysis (red) measured by the SMPS. AS = ammonium sulfate.

Appendix

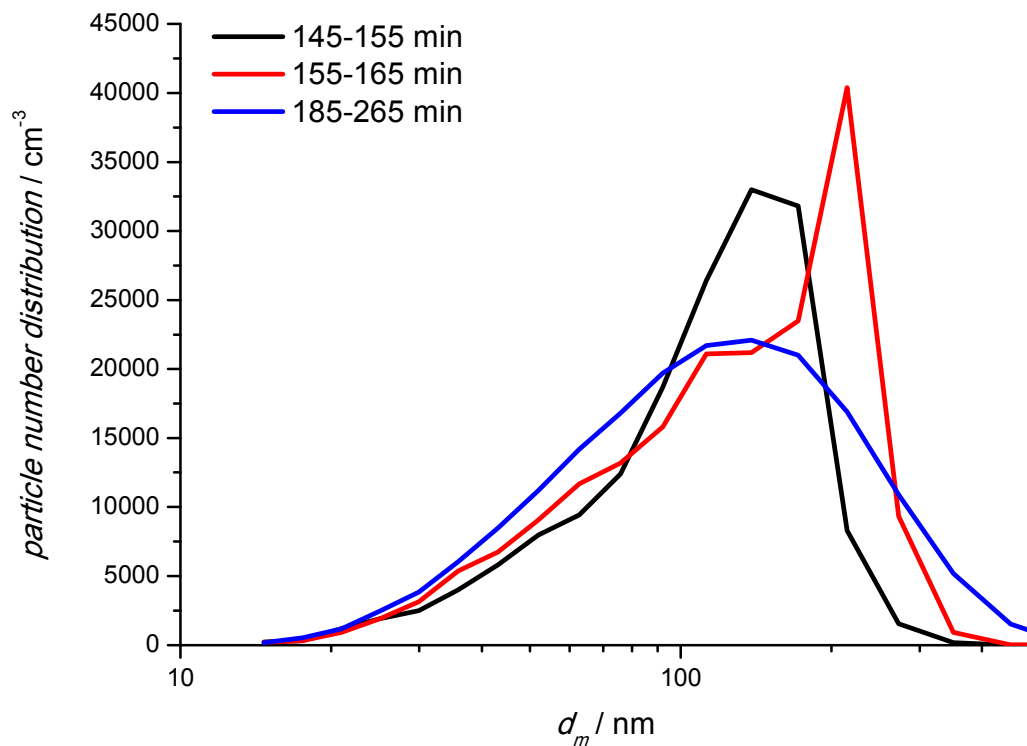


Figure 43: Size distribution of the number concentration after 20 min (145-155 min, black), 30 min (155-165 min, red) and during the last 70 min (185-265 min, blue) of the ozonolysis.

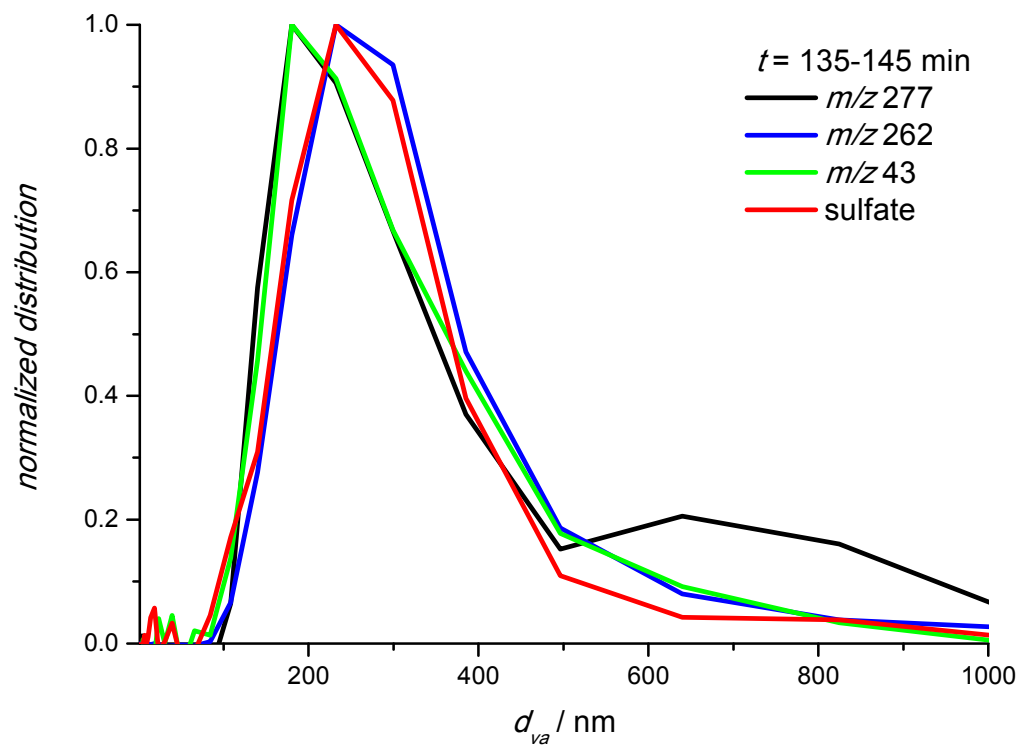


Figure 44: Size distribution of m/z 277 (black, TPP0), m/z 262 (blue, TPP), m/z 43 (green, SOA) and of sulfate (red) during the first 10 min (135-145 min) of the ozonolysis.

Appendix

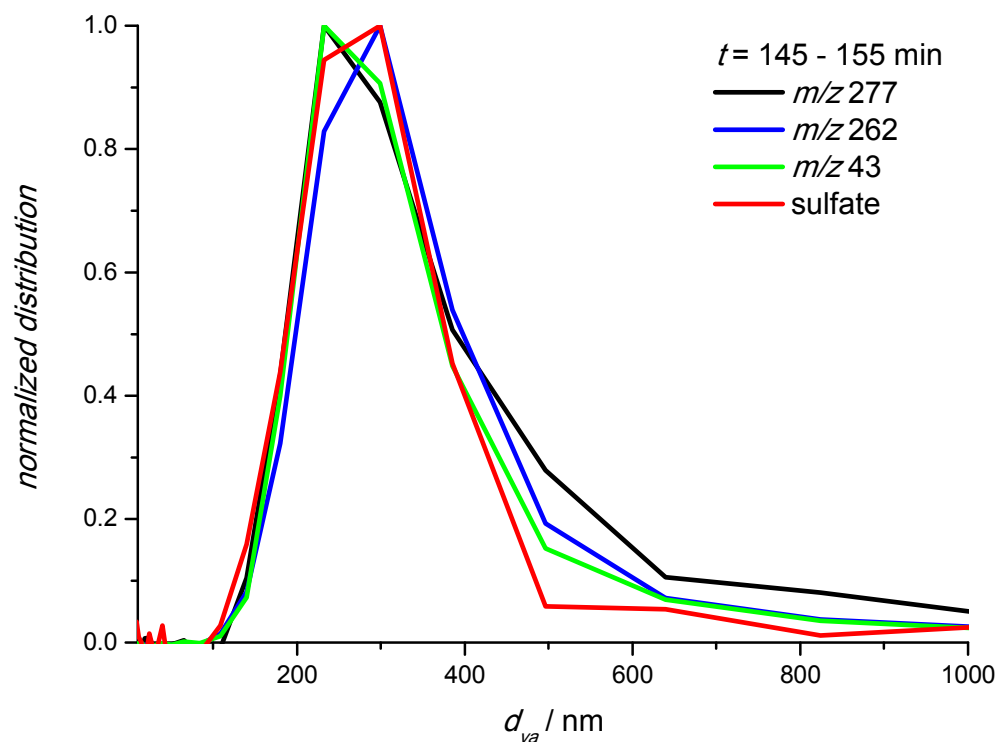


Figure 45: Size distribution of m/z 277 (black, TPPO), m/z 262 (blue, TPP), m/z 43 (green, SOA) and of sulfate (red) between 10 and 20 min (145-155 min) of the ozonolysis.

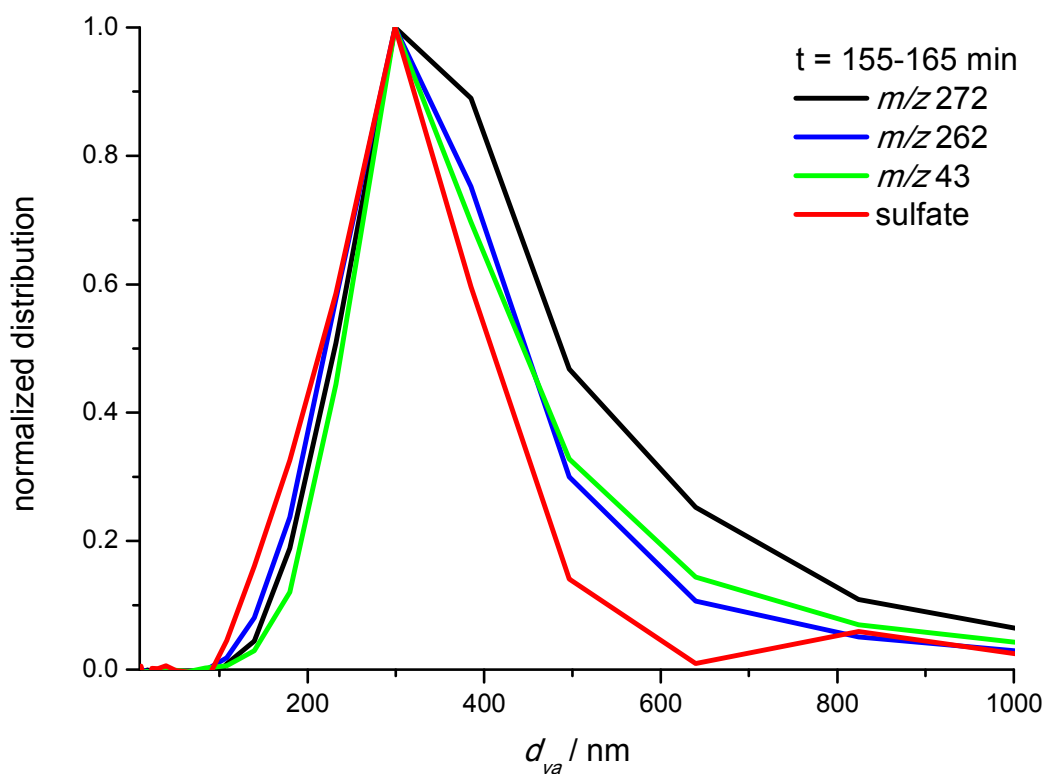
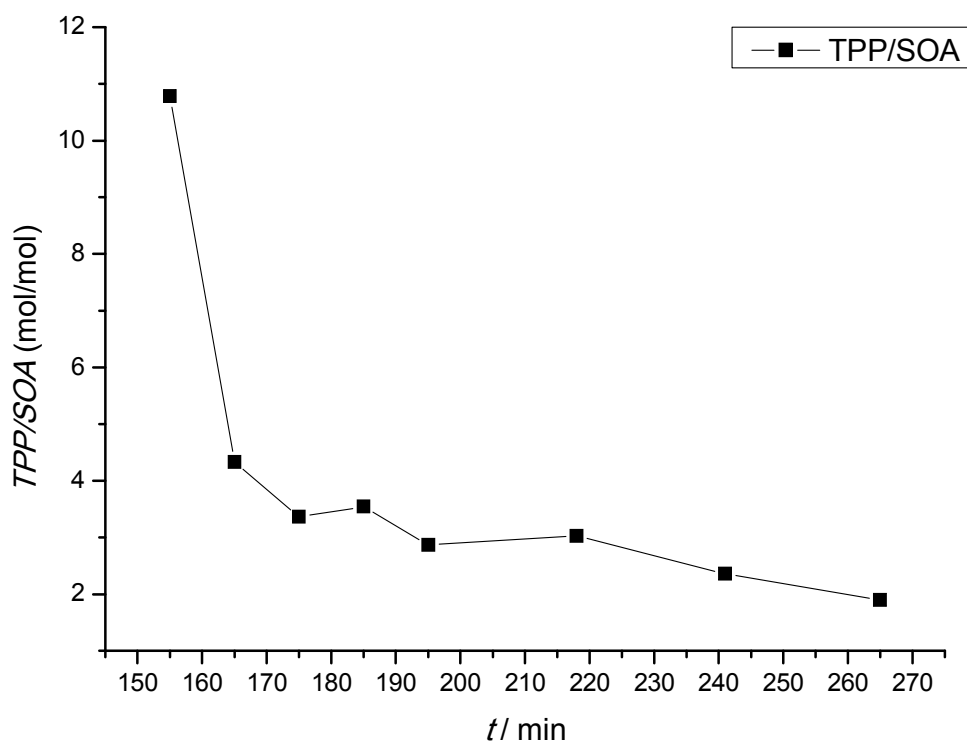
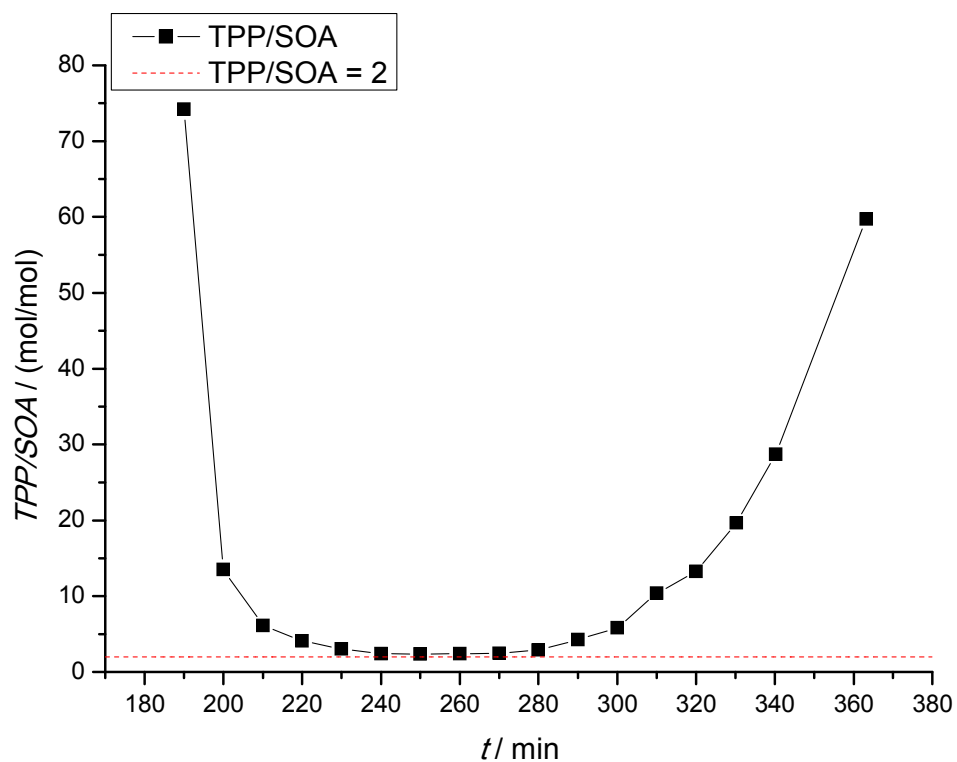


Figure 46: Size distribution of m/z 277 (black, TPPO), m/z 262 (blue, TPP), m/z 43 (green, SOA) and of sulfate (red) between 20 and 30 min (155-165 min) of the ozonolysis.

7.1.7 TPP excess to SOA

Figure 47: Ratio of TPP (= detected TPP + detected TPPO) to SOA amount at the ozonolysis of α -pinene.Figure 48: Ratio of TPP (= detected TPP + detected TPPO) to SOA amount at the ozonolysis of β -pinene.

7.2 Supplement to section 3.3

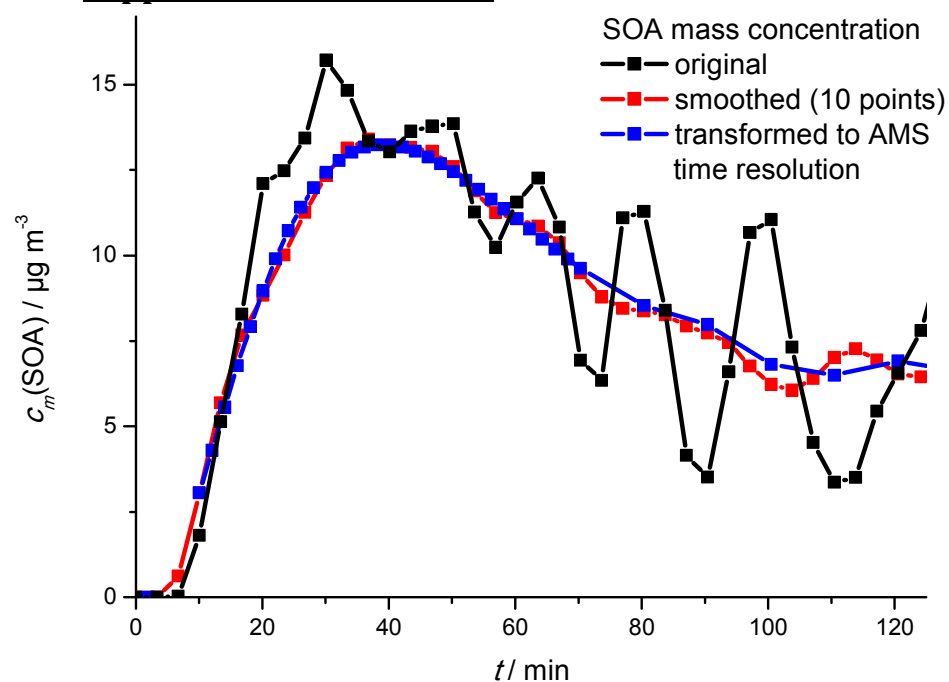


Figure 49: Smoothing (Moving average of 10 points, red) of time series of the SOA mass concentration (black), measured at the ozonolysis of α -pinene, and its transformation (blue) to the resolution of 2 min. The transformed SOA mass for the first 70 min was calculated by: $c_m(\text{SOA, transformed})/\mu\text{m}^2 \text{cm}^{-3} = -0.28 \cdot 10^{-2} - 2.48 \cdot 10^{-1} \text{min}^{-1} \cdot t + 8.99 \cdot 10^{-2} \text{min}^{-1} \cdot t^2 - 4.24 \cdot 10^{-3} \text{min}^{-1} \cdot t^3 + 9.63 \cdot 10^{-5} \text{min}^{-1} \cdot t^4 - 1.28 \cdot 10^{-6} \text{min}^{-1} \cdot t^5 + 1.05 \cdot 10^{-8} \text{min}^{-1} \cdot t^6 - 5.20 \cdot 10^{-11} \text{min}^{-1} \cdot t^7 + 1.43 \cdot 10^{-13} \text{min}^{-1} \cdot t^8 - 1.66 \cdot 10^{-16} \text{min}^{-1} \cdot t^9$. t is the measuring time after the start of the ozone generator. After 70 min, a time resolution of 10 min was applied by averaging the original values.

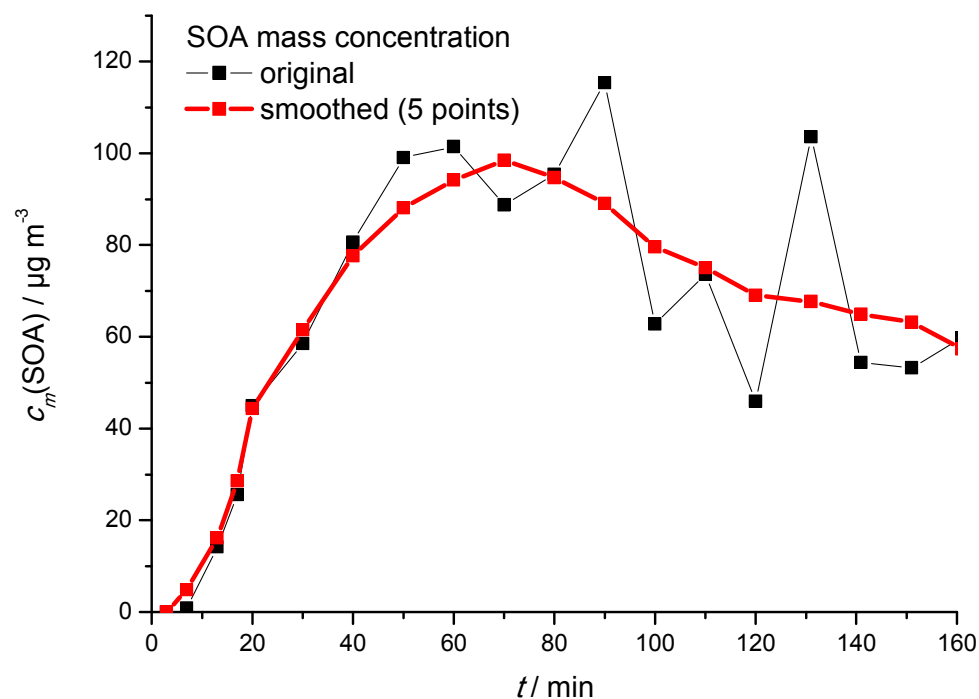


Figure 50. Smoothing (Moving average of 5 points, red) of time series of the SOA mass concentration (black), measured at the ozonolysis of β -pinene.

Appendix

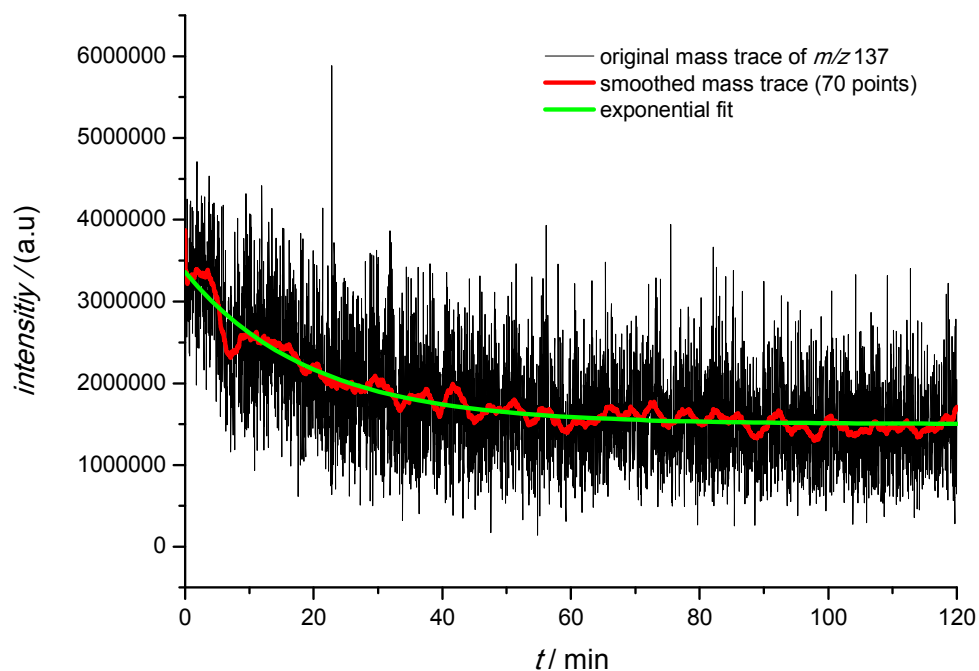


Figure 51. Original time series (black) of m/z 137 at the α -pinene ozonolysis, measured by FAPA-IT-MS. The exponential fit (green) was done from the smoothed time series (Moving average of 70 points, red). The time series of m/z 137 is calculated using: $intensity = I_0 + A \cdot e^{k \cdot t}$, whereby $I_0 = 1.50 \cdot 10^6$ a.u., $A = 1.86 \cdot 10^6$ a.u., $k = -0.05116 \text{ min}^{-1}$ and $t =$ measurement time. The intensity at $t = 0$ was $3.36 \cdot 10^6$ corresponding to the α -pinene concentration of $2.37 \mu\text{mol}/\text{m}^3$. A factor of $2.37 / (3.36 \cdot 10^6) \mu\text{mol}/\text{m}^3$ a.u. was used to convert the calculated intensity to a concentration of α -pinene.

7.3 Supplement to section 3.4

NOAA HYSPLIT MODEL
Backward trajectories ending at 0000 UTC 10 May 18
GDAS Meteorological Data

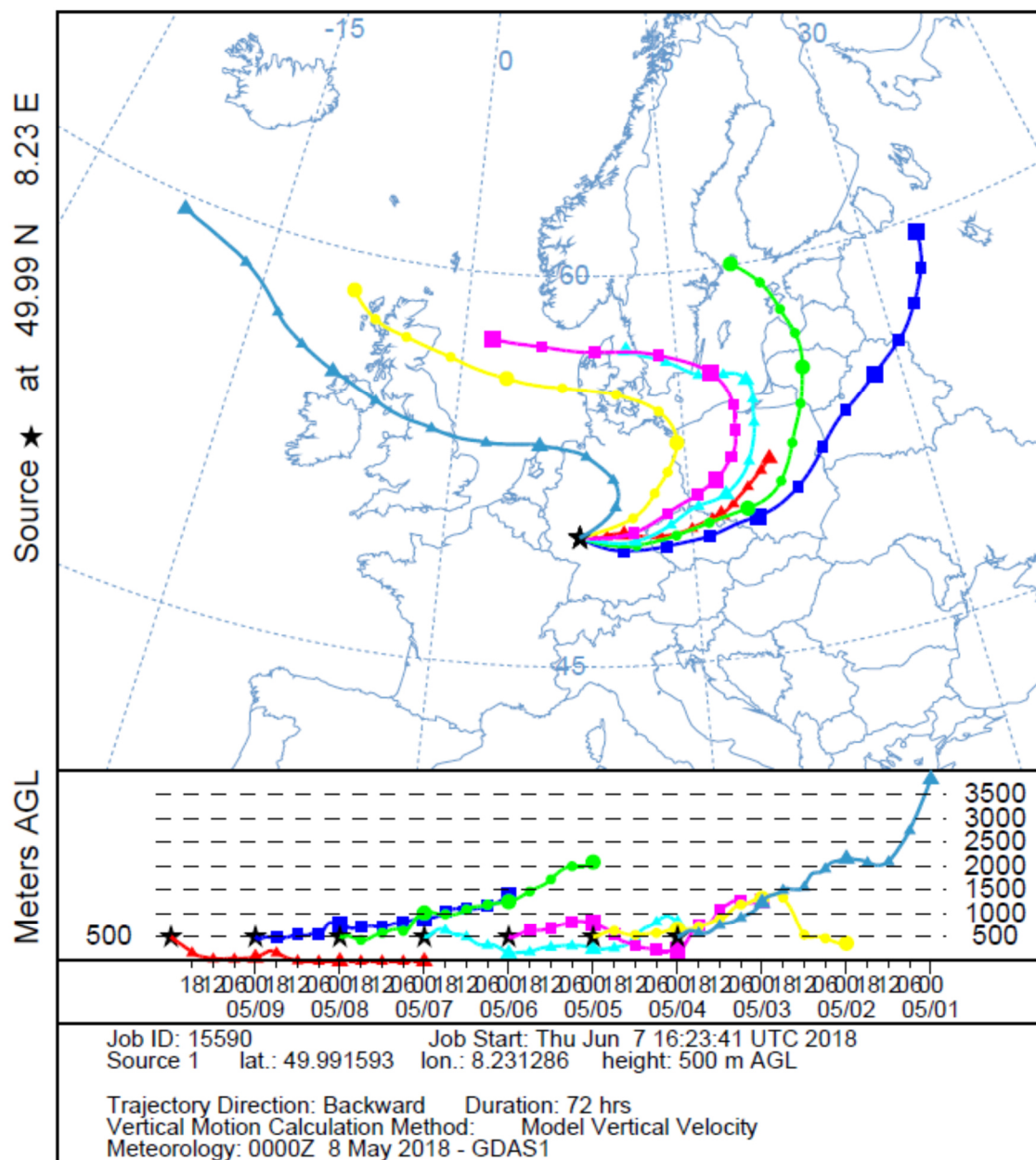


Figure 52: 72h backward trajectories from May 3rd to May 10th, 2018 every 24 hours.

7.4 Supplement to section 4.2

7.4.1 Chemicals

Table 8: Used chemicals. ν = number of alcoholic and acidic group, MSTFA = N-methyl-n-trimethylsilyl-trifluoroacetamide, BSTFA = Bis-N-trimethylsilyl-trifluoroacetamide, TMS-Im = trimethylsilyl imidazole.

compound	company	purity / %	ν^*
MSTFA*	Alfa Aesar	> 97	
BSTFA*	Supelco		
TMS-Im*	Aldrich	98	
Hexamethyldisiloxane	Alfa Aersar	97	
n-octadecanol	Sigma Aldrich	99	1
n-hexadecanol	Sigma Aldrich	99	1
n-docosanol	Acros Organics	98 %	1
n-tetradecanoic acid	Fluka	Analytical standard	1
n-hexadecanoic acid	Sigma	> 99 %	1
n-octadecanoic acid	Fluka	98 %	1
n-docosanoic acid	Fluka	Analytical standard	1
Adipic acid	Sigma Aldrich	> 99.5	1
1.10 decandioic acid			
1.12 docosandioic acid	Fluka	Analytical standard	2
1.14 tetradecandioic acid	Sigma Aldrich	98	2
1.18 octadecandioic acid	Dr. Ehrendorfer GmbH	97	2
Methanol (MeOH)	Fisher Chemicals	Optima LC/MS grade	
n-hexane	Fluka	≥ 99	
n-heptane	Roth	≥ 99	
Ethyl acetate (EtAc)	Sigma Aldrich	≥ 99.5	

7.4.2 Conditions for the determination of the calibration factor

Table 9: The applied amount of octadecanol, MSTFA and solvent.

Experiment	Mass / mg <i>n</i> - Octadecanol	Volume MSTFA/ μ L	Volume /mL and solvent
1	10.0	400	100 mL MeOH
2	6.0	240	100 mL EtAc
3	9.0	288	100 mL MeOH
4	8.5	1300	100 mL MeOH
5	4.5	144	100 mL MeOH
6	4.8	153	100 mL heptane
7	5.3	189	100 mL EtAc
8	5.1	34.2	100 mL MeOH
9	8.3	51.3	100 mL MeOH
10	10.2	68.5	100 mL MeOH
11	5.1	171	100 mL MeOH
12	8.2	257	100 mL MeOH
13	9.9	343	100 mL MeOH
		Volume and silylation agent	
14	11.4	279 μ L BSTFA	100 mL EtAc
15	13.4	367 μ L TMS-Im	100 mL EtAc

Appendix

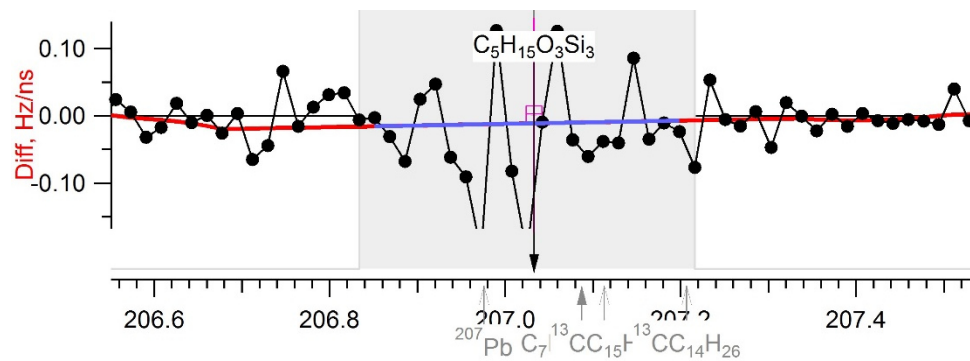
Table 10. The applied amount of the starting material, MSTFA and solvent.

Experiment	Mass and compound	Volume MSTFA	Volume solvent	and
16	20 mg n-hexadecanol	176 μ L	100 mL hexane	
17	20 mg n-docosanol	131 mL	100 mL hexane	
18	6.0 mg n-docosanol	34 μ L	100 mL EtAc	
19	5.8 mg n-docosanol	33 μ L	100 mL MeOH	
20	5.6 mg n-docosanol	32 μ L	100 mL heptane	
21	22.3 mg hexadecanoic acid	1014 μ L	50 mL EtAc	
22			50 mL Hexane	
23			50 mL Heptane	
24	22.1 mg octadecanoic acid	753 μ L	50 mL EtAc	
25			50 mL Hexane	
26			50 mL Heptane	
27	21.8 mg docosanoic acid	686 μ L	50 mL EtAc	
28			50 mL Hexane	
29			50 mL Heptane	
30	11.7 mg decandioic acid	1228 μ L	50 mL EtAc	
31	7.6 mg dodecandioic acid	707 μ L	50 mL EtAc	
32	0.3 mg tetradecandioic acid	498 μ L	50 mL EtAc	
33	10 mg octadecandioic acid	681 μ L	50 mL EtAc	
34			50 mL heptane	

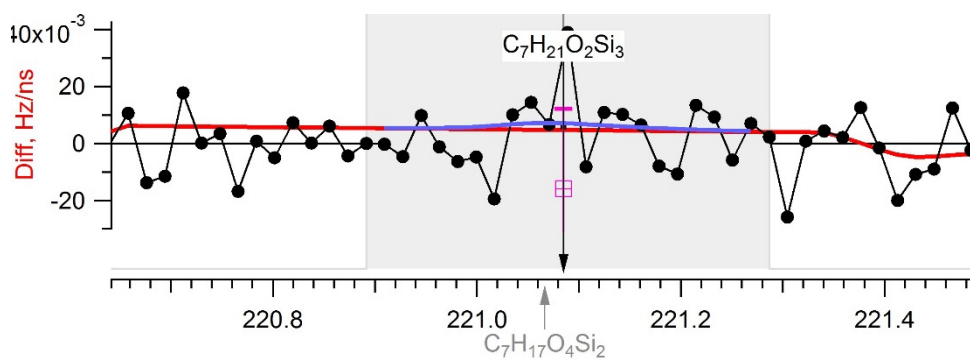
7.5 Supplement to section 4.3

Peak analysis of m/z 207, 221, 239, 255, 281 and 295 between 14:02 and 14:14 when MSTFA was not added.

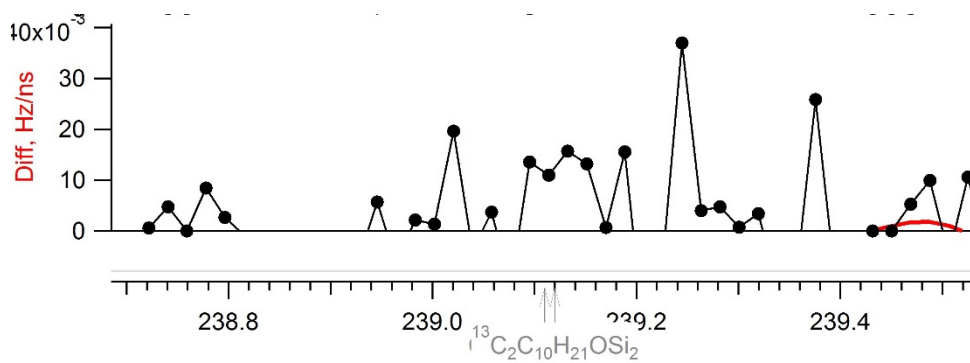
a)



b)

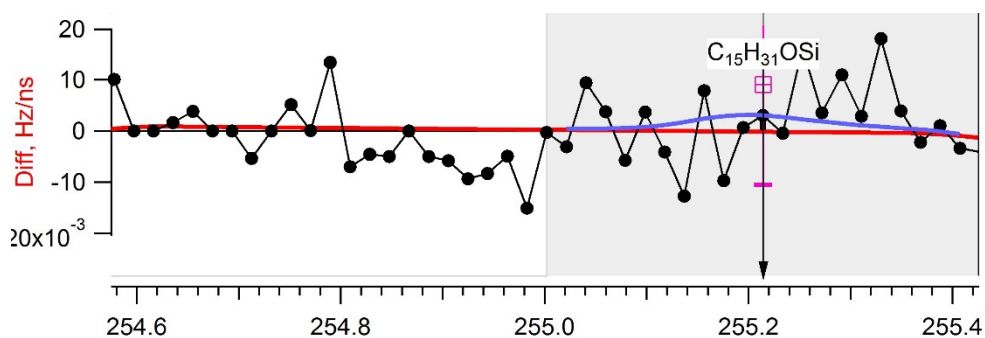


c)

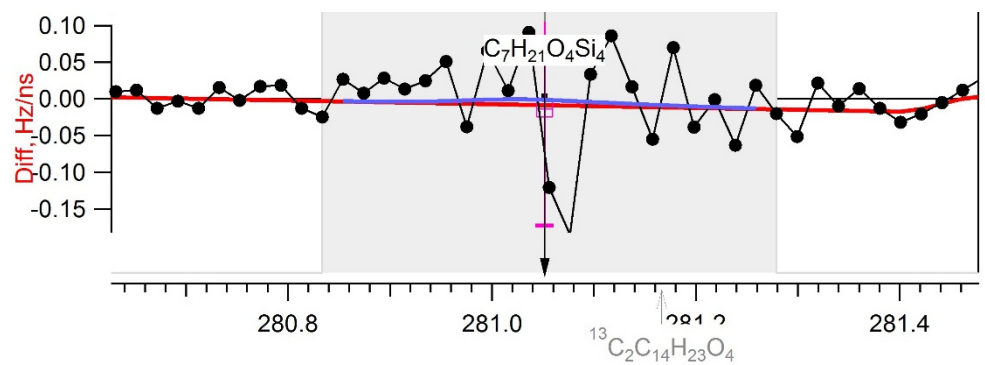


Appendix

d)



e)



f)

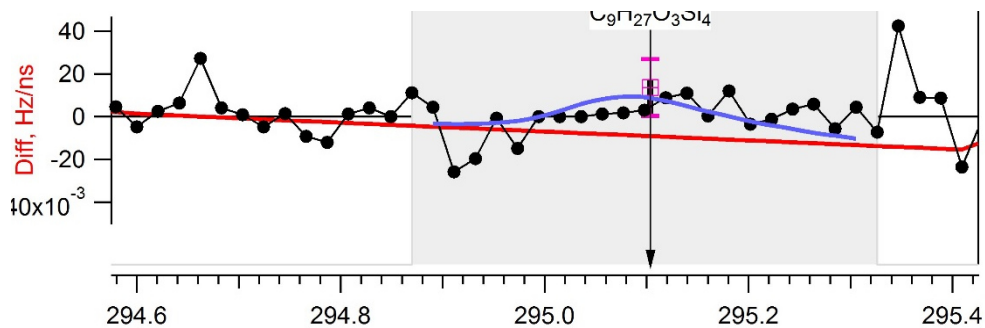
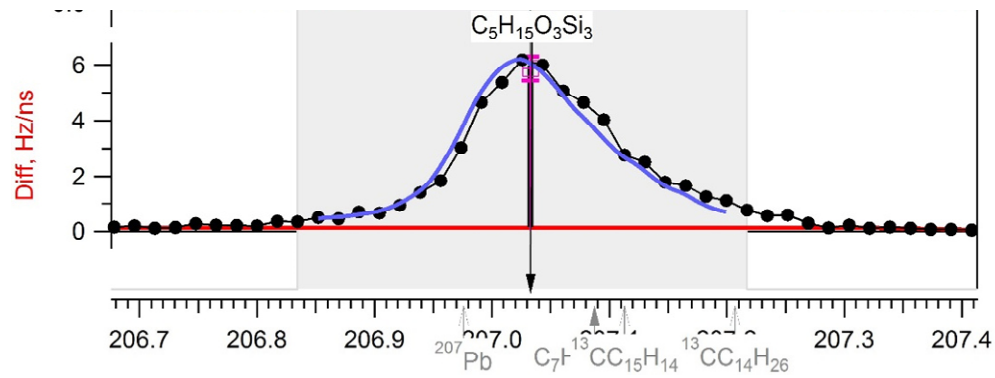


Figure 53: Peak analysis of a) m/z 207, b) 221, c) 239, d) 255, e) 281 and f) 295 between 14:02 and 14:14 when MSTFA was not added. The difference (diff) spectra are shown. The red line is the baseline, the grey and white background is the peak area and the baseline region, respectively. The blue line marks the fit of the respective part of the spectrum

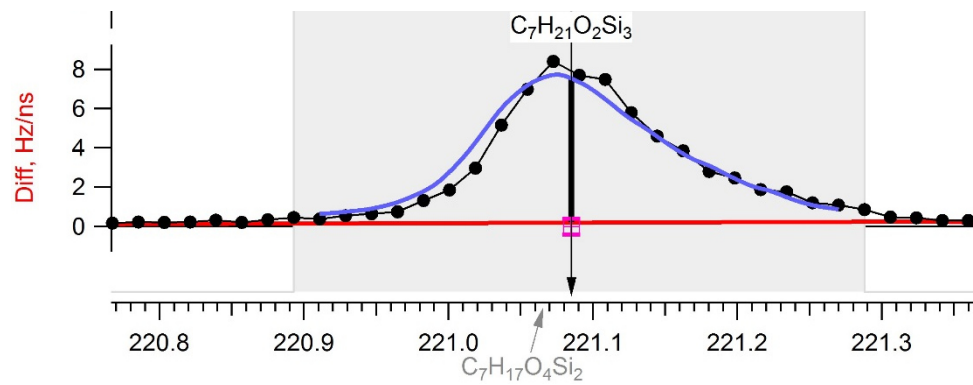
Appendix

Peak analysis of m/z 207, 221, 239, 255, 281 and 295 between 14:14 and 14:25 when MSTFA added.

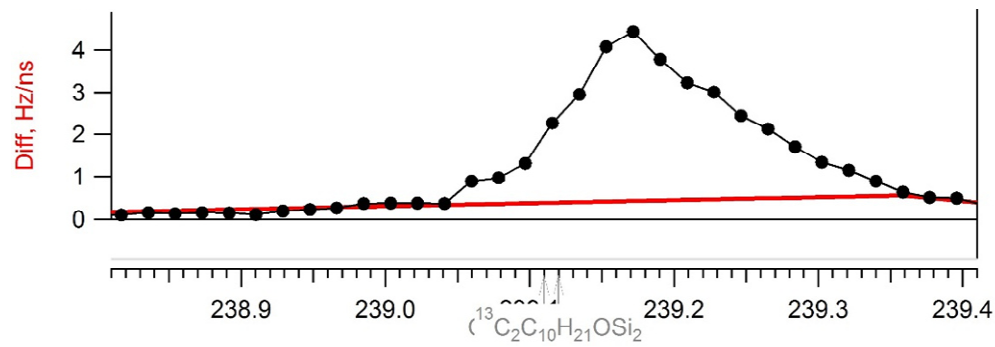
a)



b)

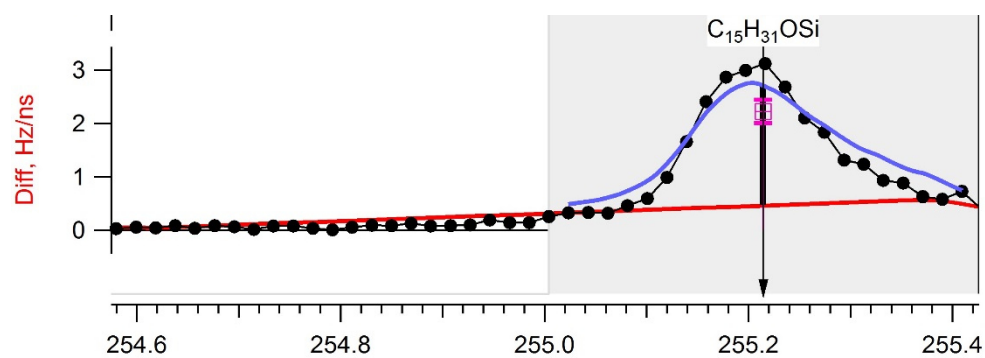


c)

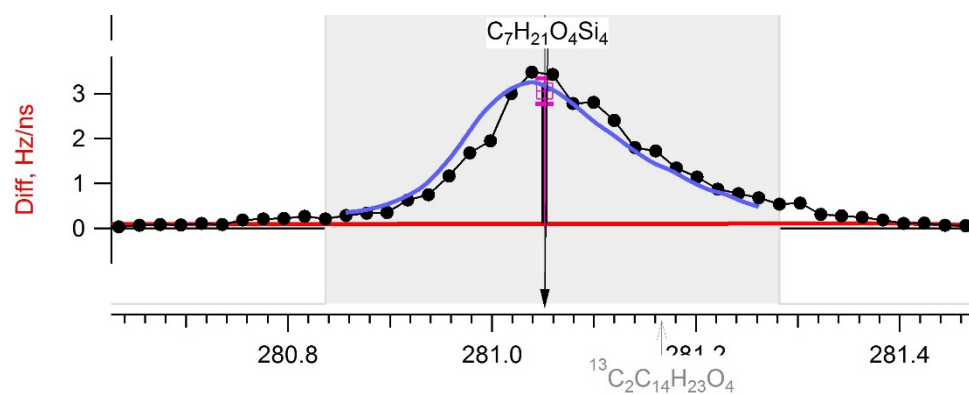


Appendix

d)



e)



f)

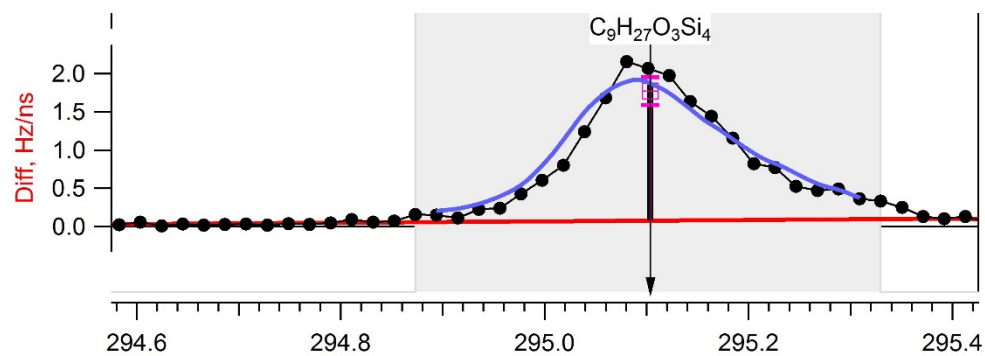


Figure 54: Peak analysis of m/z a) 207, b) 221, c) 239, d) 255, e) 281 and f) 295 between 14:14 and 14:25 when MSTFA added. The difference (diff) spectra are shown. The red line is the baseline, the grey and white background is the peak area and the baseline region, respectively. The blue line marks the fit of the respective part of the spectrum

7.6 Lists

7.6.1 Abbreviation

ADC	Analog-to-digital converter
AeroFAPA	aerosol flowing atmospheric-pressure afterglow
AMS	Aerosol mass spectrometer
APCI	atmospheric-pressure chemically ionization
AS	Ammonium sulfate
Backgr.	background
BFSP	Brute-force single particle
BSTFA	Bis-N-trimethylsilyl-trifluoroacetamide
CCN	Cloud condensation nuclei
CI	Chemical ionization
CPC	Condensation particle counter
CToF-AMS	Compact-ToF-AMS
<i>diff</i> -spectra	Difference spectra
DMA	Differential mobility analyzer
EI	Electron impact
ELVOC	Extremely low-volatile organic compound
Eq	equation
FAPA	flowing atmospheric-pressure afterglow
GC	Gas chromatography
HEPA	Highly-efficiency particulate air
HMDSO	hexamethyldisiloxane
HOM	Highly oxidized multifunctional molecule
HR-ToF-AMS	High-Resolution ToF-AMS
IE	Ionization efficiency / ion yield
IN	Ice nuclei
IT	ion trap
iToF	Ion ToF
LOQ	Limit of quantification
LV-OA	Low volatile organic aerosol
MCP	Microchannel plates
MS	Mass spectrometer
MSTFA	N-methyl-N-trimethylsilyl-trifluoroacetamide
NR	Non-refractory
ORD	Online redox derivatization
Organic	Organic material / organic compounds
PAH	Polyaromatic hydrocarbon
PM	Particulate matter
PM _{1.5}	Particulate matter with a maximum particle diameter of 1.5 μm
POA	Primary organic aerosol
PTFE	polytetrafluoroethylene
PToF	Particle time-of-flight
Q-AMS	Quadrupole-AMS
RH	Relative humidity
ROS	Reactive oxygen species
TBS	tributylsilyl
TMS	trimethylsilyl

Appendix

TMS-Im	trimethylsilyl imidazole
ToF	Time-of-Flight
TPP	Triphenylphosphine
TPPO	Triphenylphosphine oxide
SMPS	Scanning mobility particle sizer
SOA	Secondary organic aerosol
SV-OA	Semi volatile organic aerosol
VOC	Volatile organic compound

7.6.2 Figure

Figure 1: Organic chemistry in the gas- and particle phases (modified from Hallquist et al. (2009)).	4
Figure 2: Schematic description of the determination of functional groups in the aerosol particles.	7
Figure 3: Scheme of the processes during the online analysis of functional groups....	9
Figure 4: Gas sources: a) diffusion device b) permeation device (Reprinted by the permission from Springer Nature, Thorenz et al., © (2012)).	12
Figure 5: Schematic setup of an HR-ToF-AMS, based on DeCarlo et al. (2006).	15
Figure 6: Trajectories in aerodynamic lenses (based on Zhang et al., 2002).	17
Figure 7: Difference (Diff) mass spectra, obtained by subtraction of the mass spectra with chopper in <i>closed</i> position from the mass spectra with the chopper is in <i>open</i> position. a) in V-mode b) in W-mode.	22
Figure 8: Schematic setup of tandem DMA-AMS for the calibration.	23
Figure 9: Schematic setup of online APCI-MS, modified reprint from Warscheid and Hoffmann (2001).	27
Figure 10: Schematic FAPA setup (Reprinted (adapted) from Brüggemann et al. (2015)).	27
Figure 11: Scheme of a quadrupole ion trap, modified from Yoshinari (2000).	29
Figure 12: Cross-section of a microchannel plate and visualization of the electron multiplication (Reprint from de Hoffmann and Stroobant, 2007).	31
Figure 13: Reaction mechanism of the reaction of TPP with peroxidic compounds via a) a bimolecular nucleophile displacement, b) and c) cyclic intermediates at hydroperoxides and cyclic peroxides, respectively.	34
Figure 14: Schematic setup of ORD-AMS.	36
Figure 15: Setup of the SOA seed experiments.	37
Figure 16: Mass spectra of a) triphenylphosphine oxide TPPO and b) triphenylphosphine TPP.	38
Figure 17: Time series a) of detected TPPO (black) and detected TPP (red), b) of peroxide concentration (black) after background correction and mass concentration of the aerosol and SOA (red), and c) of peroxide per SOA (black).	40
Figure 18: Size distributions of m/z 277 (black, TPPO), m/z 262 (blue, residual TPP), m/z 43 (green, SOA), sulfate (red) for following periods: before the start of the ozonolysis a) without and b) with adding TPP, at the end (185-265 min) of the ozonolysis c) without and d) with adding TPP.	42

Appendix

Figure 19: Ozonolysis of β -pinene in the presence of AS aerosol. Time series of a) the concentration of peroxide (black), particles (red), and SOA (blue) and b) peroxide/SOA.....	43
Figure 20: Schematic setup of peroxide analysis.....	46
Figure 21: Schematic setup for the SOA generation.....	47
Figure 22: Ozonolysis of α -pinene. Time series of peroxide (black), SOA mass concentration (blue) and the peroxide / SOA yield (red).....	50
Figure 23: Ozonolysis of β -pinene. Time series of peroxide (black) and SOA mass concentration (blue) and the peroxide / SOA yield (red).....	51
Figure 24: Peroxide formation a) by autoxidation, b) by dimer formation in the gas phase and c) peroxyhemiacetal formation on the particle surface.....	52
Figure 25: Peroxide sinks a) by thermal or acid-catalyzed decomposition, b) by reactions on the surface, such as the reaction with OH radicals and c) by the oxidation of other functional groups, such as ketones to esters.....	52
Figure 26: The time series of the relative amounts of peroxide (black), reacted α -pinene (red), SOA mass (cyan) and SOA surface.....	53
Figure 27: a) Time series of the relative amount of detected TPPO to detected TPP, LOQ and blank value, b) diurnal variation of the estimated peroxide concentration and c) time series of the global radiation and temperature.....	56
Figure 28: a) Schematic setup for the online silylation. b) Aerosol generator for test compounds. c) Transfer of the silylation agent into the flow tube.....	59
Figure 29: Response factor $\chi^*(\text{TMS}^+, s)$ of TMS-derivatives s	62
Figure 30: Determination of the yield of the online silylation of tetradecanedioic acid. The courses of a) the measured concentration of the total aerosol (black) and measured signals of the marker ion $[\text{M}-\text{CH}_3]^+$ of MSTFA (red) and the TMS ion (blue), b) the course of the part of the product on the total aerosol (black) and the TMS ⁺ ion. c) Comparison of the concentration of the product, calculated by Eq. 49, to the concentration of the product in b).....	64
Figure 31: The calculated total mass concentration vs the measured mass concentration of the TMS derivatives of n -octadecanol (black square), n -octadecanoic acid (black dots), n -docosanoic acid (red dots), 1, 12 dodecanedioic acid (black triangle), 1, 14 tetradecanedioic acid (red triangle) and 1,18 octadecanedioic acid (green triangle).....	65
Figure 32: Size distribution of the total aerosol when supplying n -octadecanoic acid directly (black) and through the reactor (red) to the AMS.....	66
Figure 33: Vaporization of the silyl-ester of adipic acid when MSTFA is added (grey marked).....	67
Figure 34: Ambient air measurement on 18/08/2017. a) Measured organic aerosol. b) The concentration of the residual organic aerosol when MSTFA was added. c) TMS ⁺ -signal of MSTFA (red), hexamethyldisiloxane (blue), and the residual organic aerosol (black) when MSTFA was added. The periods with silylation are highlighted in grey, the periods without silylation in white.....	70
Figure 35: Mass spectra (unit mass resolution) of measured organic bulk aerosol in the range of m/z 200 -300, a) with b) without the reactor.....	72
Figure 36: Oxidation of a) cyclic and b) acyclic polymethylsiloxanes to silanols and their silylation to siloxanes (TMS-silanol ethers).....	73

Appendix

Figure 37: Time series of a) the signals at m/z 207 and m/z 221, and of the temperature (blue) b) the water concentration (blue) and the relative humidity (cyan).....	74
Figure 38: Size distribution of a) the TMS-silanol-ether related signal at m/z 221 and b) sulfate.....	75
Figure 39: Schematic setup for the calibration of the AMS.....	101
Figure 40: Determination of Jayne shape factor S for TPPO.	102
Figure 41: Results from the IE calibration of TPPO using the BFSP method (green) and MS/CPC method (red).....	103
Figure 42: Size distribution of the number concentration before the ozonolysis (black) and in the first 10 min ($t = 135-145$ min) of the ozonolysis (red) measured by the SMPS.....	105
Figure 43: Size distribution of the number concentration after 20 min (145-155 min, black), 30 min (155-165 min, red) and during the last 70 min (185-265 min, blue) of the ozonolysis.....	106
Figure 44: Size distribution of m/z 277 (black, TPPO), m/z 262 (blue, TPP), m/z 43 (green, SOA) and of sulfate (red) during the first 10 min (135-145 min) of the ozonolysis.	106
Figure 45: Size distribution of m/z 277 (black, TPPO), m/z 262 (blue, TPP), m/z 43 (green, SOA) and of sulfate (red) between 10 and 20 min (145-155 min) of the ozonolysis.	107
Figure 46: Size distribution of m/z 277 (black, TPPO), m/z 262 (blue, TPP), m/z 43 (green, SOA) and of sulfate (red) between 20 and 30 min (155-165 min) of the ozonolysis.	107
Figure 47: Ratio of TPP (= detected TPP + detected TPPO) to SOA amount at the ozonolysis of α -pinene.....	108
Figure 48: Ratio of TPP (= detected TPP + detected TPPO) to SOA amount at the ozonolysis of β -pinene.....	108
Figure 49: Smoothing (Moving average of 10 points, red) of time series of the SOA mass concentration (black), measured at the ozonolysis of α -pinene, and its transformation (blue) to the resolution of 2 min.....	109
Figure 50. Smoothing (Moving average of 5 points, red) of time series of the SOA mass concentration (black), measured at the ozonolysis of β -pinene.....	109
Figure 51. Original time series (black) of m/z 137 at the α -pinene ozonolysis, measured by FAPA-IT-MS. The exponential fit (green) was done from the smoothed time series (Moving average of 70 points, red).....	110
Figure 52: 72h backward trajectories from May 3 rd to May 10 th , 2018 every 24 hours.	111
Figure 53: Peak analysis of a) m/z 207, b) 221, c) 239, d) 255, e) 281 and f) 295 between 14:02 and 14:14 when MSTFA was not added. The difference (diff) spectra are shown.....	115
Figure 54: Peak analysis of m/z a) 207, b) 221, c) 239, d) 255, e) 281 and f) 295 between 14:14 and 14:25 when MSTFA added.	117

7.6.3 Table

Table 1: Yield of peroxide mass per SOA mass during the last 60 min of the experiments, the chamber temperature and relative humidity, the initial terpene concentration, the ozone concentration without reaction with the terpene and the reference.....	49
Table 2: Conversion factors $\chi^*(i, s)$ of other characteristic ions	63
Table 3: Estimated vapor pressure of trimethylsilyl- and tributylsilyl derivatives....	68
Table 4: Relation between the cyclic and acyclic polymethylsiloxane precursor, the silanols as their oxidation product, the TMS-silanol ether and the nominal mass of the $[M-CH_3]^+$ of TMS-silanol-ethers.....	73
Table 5: Achieved goals at ORD-AMS for peroxide analysis (chapter 3) and the online silylation (chapter 4).....	79
Table 6: Background contribution of TPPO on detected TPP, obtained at several SOA-seed aerosol experiments.....	103
Table 7: Obtained H/C, O/C according to Kuwata et al. (2012) and resulting density for the period during the ozonolysis.....	104
Table 8: Used chemicals.....	112
Table 9: The applied amount of octadecanol, MSTFA and solvent.....	112
Table 10. The applied amount of the starting material, MSTFA and solvent.....	113

7.6.4 Equation

Eq. 1.....	8
Eq. 2.....	8
Eq. 3.....	14
Eq. 4.....	14
Eq. 5.....	18
Eq. 6.....	18
Eq. 7.....	18
Eq. 8.....	18
Eq. 9.....	19
Eq. 10.....	19
Eq. 11.....	19
Eq. 12.....	19
Eq. 13.....	19
Eq. 14.....	20
Eq. 15.....	20
Eq. 16.....	21
Eq. 17.....	21
Eq. 18.....	21
Eq. 19.....	21
Eq. 20.....	21
Eq. 21.....	21
Eq. 22.....	23
Eq. 23.....	23
Eq. 24.....	23

Appendix

Eq. 25	23
Eq. 26	24
Eq. 27	24
Eq. 28	25
Eq. 29	25
Eq. 30	25
Eq. 31	26
Eq. 32	29
Eq. 33	29
Eq. 34	29
Eq. 35	39
Eq. 36	39
Eq. 37	39
Eq. 38	39
Eq. 39	39
Eq. 40	61
Eq. 41	61
Eq. 42	62
Eq. 43	62
Eq. 44	64
Eq. 45	64
Eq. 46	64
Eq. 47	64
Eq. 48	64
Eq. 49	65
Eq. 50	69
Eq. 51	69
Eq. 52	69
Eq. 53	69
Eq. 54	70
Eq. 55	101
Eq. 56	101
Eq. 57	101
Eq. 58	102
Eq. 59	102
Eq. 60	104
Eq. 61	104
Eq. 62	105

8 List of related publications and presentations

Publications:

11/2019

M. Weloe, T. Hoffmann: Application of time-of-flight aerosol mass spectrometry for the real-time measurement of particle phase organic peroxides: An online redox derivatization – aerosol mass spectrometer (ORD-AMS), *Atmos. Meas. Tech. Discuss.*, <https://doi.org/10.5194/amt-2019-406>.

Oral presentation:

04/2017

M. Weloe, S. Morat, T. Hoffmann: Nachweis von Alkoholen und Carbonsäuren in Aerosolpartikeln mittels Online-Silylierung und Aerosolmassenspektrometrie, *ANAKON 2017*, Tübingen, Germany.

Poster presentations:

08/2017

M. Weloe, S. Morat, T. Hoffmann: Development of a detection method to determine alcohols and carboxylic acids in aerosol particles using in-situ silylation and aerosol mass spectrometry, *European Aerosol Conference 2017*, Zurich, Switzerland.

10 Curriculum Vitae

Personal Information

Name: Marcel Mahendra Weloe
Date of birth: May, 6th, 1987
Place of birth: Mainz, Germany

Education

01/2015-05/2020 PhD studies
Chemistry Department
Johannes Gutenberg-University Mainz, Germany
Workgroup of Prof. Dr. Hoffmann

10/2008-12/2014 Diploma studies in chemistry
Johannes Gutenberg-University Mainz, Germany

09/2007-08/2008 Voluntary Year of Social Service
L'Arche des Bruxelles in Brussels, Belgium

06/2007 Abitur
Graf-Stauffenberg Gymnasium, Flörsheim, Germany

Working Experience

07/2019- present Commercial Broker (self-employed)
BUNDconnect GmbH
Lauf, Germany
BUND Naturschutz Marketing GmbH
Lauf, Germany

01/2015-07/2018 Research assistant
Johannes Gutenberg-University Mainz, Germany
Workgroup of Prof. Dr. Hoffmann

Mainz, March 4th, 2020